Precise Measurement of Solar Neutrinos with Super-Kamiokande III

Motoyasu Ikeda

December 16 2009

Abstract

New solar neutrino measurements with the Super-Kamiokande detector are reported. The main motivation of this thesis is to observe the spectrum distortion of solar neutrinos caused by the matter effect of neutrino oscillation in the Sun (MSW effect).

The data for this thesis were taken between August 2006 and August 2008, during the third phase of Super-Kamiokande (SK-III). Two neutrino samples are used in this thesis. The first one with total electron energy between 6.5 and 20MeV has a total livetime of 547.9 days. The second, with total electron energy between 4.5 and 6.5MeV has a total livetime of 298.2 days after rejecting high background periods caused by radioactive impurities accidentally injected into the detector.

With improved detector calibrations, a full detector simulation, and analysis methods, the systematic uncertainty on the total neutrino flux is estimated to be $\pm 2.3\%$, which is about two thirds of the systematic uncertainty in the first phase of Super-Kamiokande (SK-I). The observed ^{8}B solar flux in the 5.0 to 20MeV electron energy region is 2.28$\pm$ 0.04 (stat.) $\pm$ 0.05 (sys.) $\times 10^6 \mathrm{cm}^{-2}\mathrm{sec}^{-1}$, in agreement with previous measurements. The day-night asymmetry is measured to be $A_{DN} = -0.057 \pm 0.031(\mathrm{stat.}) \pm 0.013(\mathrm{sys.})$. In the 4.5-5.0 MeV region, the observed flux is $2.14^{+0.56}_{-0.54}$ (stat) $\times 10^6 \mathrm{cm}^{-2}\mathrm{sec}^{-1}$ and is consistent with the flux in the 5.0-20MeV region.

A global oscillation analysis is carried out using SK-I, II, and III, and is combined with the results of other solar neutrino experiments. The best-fit oscillation parameters are obtained with the world's best accuracy as $\sin^2\theta_{12} = 0.29^{+0.024}_{-0.011}$ and $\Delta m^2_{12} = 6.03^{+1.21}_{-1.67} \times 10^{-5} eV^2$. Combined with KamLAND result, the best-fit oscillation parameters are found to be $\sin^2\theta_{12} = 0.304^{+0.017}_{-0.016}$ and $\Delta m^2_{12} = 7.59^{+0.12}_{-0.39} \times 10^{-5} eV^2$. This parameter region corresponds to a ^{8}B flux of $5.08^{+0.10}_{-0.07} \times 10^6 \mathrm{cm}^{-2}\mathrm{sec}^{-1}$.

The χ^2 value of spectrum fit with the solar plus KamLAND best-fit prediction is 26.7/20d.o.f. which is slightly better than 27.7/20d.o.f. with a flat shape. Although, this result is not statistically significant, it is estimated that the improved calibration and analysis methods will give a sensitivity of 3σ level discovery of the spectrum distortion within a few years, together with re-analysis of the SK-I data.

Acknowledgements

First of all, I would like to express my great gratitude to Prof. Y. Takeuchi for giving me the excellent opportunity of studying the solar neutrino at Super-Kamiokande. This thesis would never exist without his support and encouragement.

I would like to appreciate Prof. Y. Suzuki for giving me the opportunity of studying in the Super-Kamiokande experiment.

I would like to extend my gratitude to LOWE members, Prof. M. Nakahata, Prof. Y. Koshio, Prof. A. Takeda, Prof. H. Sekiya, Prof. S. Yamada, Prof. H. Watanabe, Prof. M. Sakuda Prof. H. Ishino Prof. Y. Fukuda Prof. M. Vagins, Prof. M. Smy, Prof. K. Martens, Prof. C. Shaomin, T. Iida, K. Ueno, T. Yokozawa, K. Bays, Andrew, Jordan, Dr. J. P. Cravens, Dr. L. Marti, Dr. J. Schuemann, H. Zhang, and B. Yang.

I would like to thank Kamkoka members who encouraged me for all the time, Prof. K. Abe, Prof. Y. Hayato, Prof. J. Kameda, Prof. K. Kobayashi, Prof. M. Miura, Prof. S. Mine, Prof. S. Moriyama, Prof. S. Nakayama, Prof. Y. Obayashi, Prof. H. Ogawa, Prof. M. Shiozawa, Prof. S. Tasaka, Prof. M. Yamashita, Dr. A. Minamino, Dr. Y. Takenaga, Dr. G. Mitsuka, Dr. H. Nishino, Dr. R. Wendell, Dr. M. Litos, Dr. J. L. Raaf, Dr. O. Simard, Dr. K. Hiraide, Dr. A. Minamino, K. Ueshima, C. Ishihara, N. Okazaki, D. Ikeda, T. Tanaka, Y. Furuse, Y. Idehara, D. Motoki T.F. McLachlan, S. Hazama, Y. Nakajima, Y. Yokosawa, Y. Kozuma, T. Hokama, H. Nishiie, A. Shinozaki, K. Iyogi, Maggie, Patrick, Y. Heng, P. Mijakowski, M. Dziomba, K. Connolly, and Prof. C. K. Jung.

Finally, I would like to express my greatest appreciation and gratitude to my family, relatives, all my friends, and K. Nagaoka.

Contents

Chapter 1

Introduction

The Sun is the source of life, the source of neutrinos. The number of solar neutrinos passing through our body is 6.6×10^{10} per cm^2 per sec. Since the beginning of 1960s, many experiments have succsessfully observed the neutrino signal from the Sun.

Until 1990s, all the results reported from the solar neutrino experiments showed that the observed solar neutrino flux was significantly smaller than the flux calculated by the Standard Solar Model (SSM). This conflict between experiments and the SSM was called "solar neutrino problem". In 2001, the high statistical measurement done by Super-Kamiokande in Japan, which is a water Cherenkov detector with the fiducial volume of 22.5kton, together with SNO experiment in Canada, which can measure the all types of active neutrinos from the Sun, answered that the solar neutrino problem can be understood by considering the effect of the neutrino oscillation.

The neutrino oscillation was at first studied by Z.Maki, M.Nakagawa, S.Sakata, V.Gribov and B.Pontecorvo [1]. Their main subject at that time was the neutrino oscillation in vacuum. As Wolfenstein, Mikheyev and Smirnov discussed the neutrino oscillation in matter [2, 3], it was found that the adiabatic transition of neutrinos can occur under some special conditions in matter, such as the Sun and the Earth. This is call 'MSW effect'. By taking into account the MSW effect, the results of all the solar neutrino observations are consistent with the prediction of SSM, and the experimental uncertainties of the solar neutrino flux (^{8}B neturino) has been reaching the size of theoretical uncertainty. However, the direct confirmation of the MSW effect has not been done.

From this standpoint, this thesis is focused on the direct direct verification of the MSW effect in the Sun. This is done by a precise measurement of energy spectrum of ^{8}B neturinos. Since the oscillation probability of electron neutrinos has energy dependence due to the MSW effect, the spectrum is expected to be distorted from the original shape of ^{8}B neturinos.

In this thesis, the results of solar neutrino analysis using Super-Kamiokande detector are reported after the 547.9 days of observation from August 2006 to August 2008 (SK-III). In Chapter 2, introductions of SSM, the neutrino oscillation, and the solar neutrino experiments are presented. The strategies to observe the energy spectrum is also explained in Chapter 2. In Chapter 3, an overview of Super-Kamiokande experiment is given. From Chapter 4 to 9, the method of solar neutrino data analysis in SK-III is explained. The results of data analysis and oscillation analysis with Super-Kamiokande are presented in Chapter 10 and 11. Finally, the discussion and the conclusion is given in Chapter 12.

Chapter 2

Physics Background

In this chapter, an overview of solar models, the neutrino oscillation and solar neutrino experiments are shown. In Section 2.1, the introduction of Standard Solar Model will be given, and current problems of the theory will be shown. After a brief explanation of ^{8}B neutrino spectrum in Section 2.2, a short discussion of neutrino oscillation will be given in Section 2.3. Results of all solar neutrino experiments are summarized in Section 2.4. The main motivation and strategies of this thesis is explained in the last section.

2.1 Solar neutrino and the Standard Solar Model

How does the Sun shine? (J.N.Bahcall) This is the first question in his book "Neutrino Astrophysics" [4]. To answer this quite astronomical question, we had to wait until the theory of relativity and the quantum mechanics come out. It was in 1939 that Hans Bethe first discussed that the nuclear fusion is the source of the energy produced in a star including the Sun[6].

2.1.1 Nuclear reactions in the Sun

The nuclear fusion reaction can be written as:

$$4p \longrightarrow \alpha + 2e^+ + 2\nu_e \tag{2.1}$$

This reaction releases an energy of 26.7 MeV. Equation 2.1 is a form of a net reaction which proceeds via two different reaction systems; proton-proton chain (pp chain) and Carbon-Nitrogen-Oxygen cycle (CNO cycle) which are shown in Figure 2.1 and 2.2. Here, neutrinos are generated by the following reactions;

In pp chain:

$$p + p \longrightarrow {}^2\mathrm{H} + e^+ + \nu_e \qquad \text{(pp)} \tag{2.2}$$

$$p + e^- + p \longrightarrow {}^2\mathrm{H} + \nu_e \qquad \text{(pep)} \tag{2.3}$$

$${}^7\mathrm{Be} + e^- \longrightarrow {}^7\mathrm{Li} + \nu_e \qquad ({}^7\mathrm{Be}) \tag{2.4}$$

$${}^8\mathrm{B} \longrightarrow {}^8\mathrm{Be}^* + e^+ + \nu_e \qquad ({}^8\mathrm{B}) \tag{2.5}$$

$${}^3\mathrm{He} + p \longrightarrow \alpha + e^+ + \nu_e \qquad \text{(hep)} \tag{2.6}$$

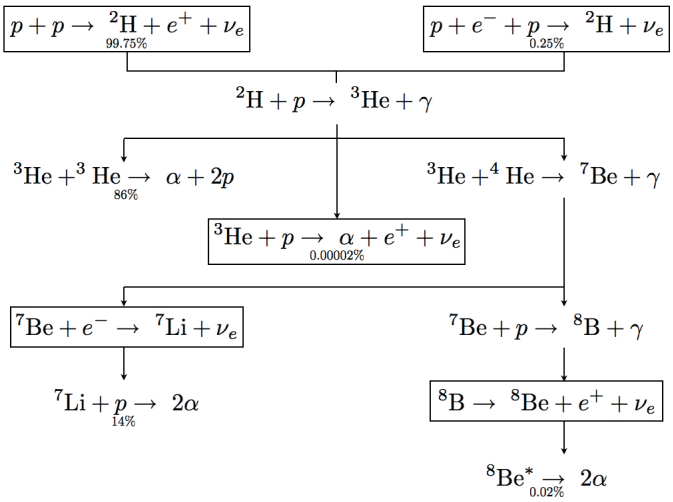

Figure 2.1: The pp-chain reactions

In CNO cycle

$$^{13}\mathrm{N} \longrightarrow {}^{13}\mathrm{C} + e^+ + \nu_e \tag{2.7}$$

$$^{15}\mathrm{O} \longrightarrow {}^{15}\mathrm{N} + e^+ + \nu_e \tag{2.8}$$

$$^{17}\mathrm{F} \longrightarrow {}^{17}\mathrm{O} + e^+ + \nu_e \tag{2.9}$$

The CNO sycle is predicted to contribute about 2% to the total solar luminosity, and other 98% contribution is due to pp chain [5].

2.1.2 Overview of the Standard Solar Model

The Standard Solar Model (SSM) predicts the solar neutrino flux which has been developed by J.N.Bahcall, who took over Bethe's calculation. Some of the input parameters of SSM are nuclear reaction cross section, the solar luminosity, the solar age, elemental abundances, radiative opacities. There are recent solar models which are not based on SSMs. One of them is provided by Turck-Chieze et al. [7]. Their calculation is based on the standard theory of stellar evolution which is tuned especially for the Sun using seismic measurement (called the seismic model). The seismic model predicts the neutrino fluxes which agree with the SSM prediction within their uncertainty $\sim 10\%$. In this thesis, the BP04 SSM [8] is used to calculate the solar neutrino flux. Figure 2.3 shows the expected energy spectrum of solar neutrinos. Our results will be also compared to BP05(OP) and BP05(AGS,OP) [9] to see our sensitivity to the different SSMs. To understand difference of the SSMs, some key aspects for the SSM are explained in remaining part of this section. Then, in the next section, a current problem of SSM will be explained.

S-factor (Cross section factor)

The energy dependence on the nuclear fusion cross section is defined by a conventional form [4]:

$$\sigma(E) = \frac{S(E)}{E} \exp(-2\pi\eta) \tag{2.10}$$

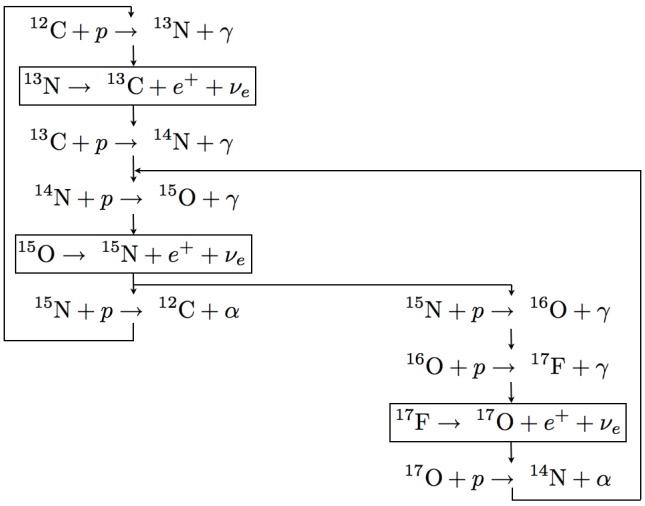

Figure 2.2: The CNO-cycle reactions

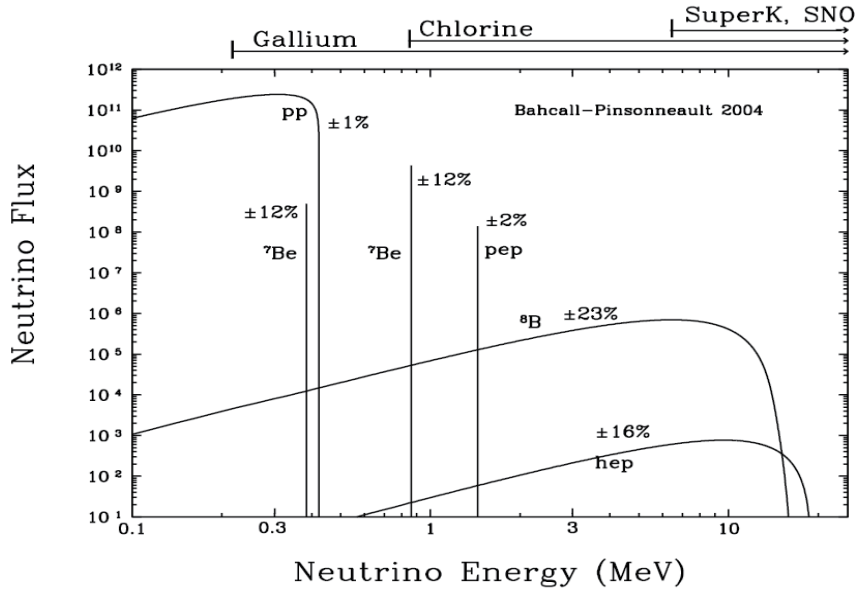

Figure 2.3: The solar neutrino energy spectrum predicted by BP04SSM.

where

$$\eta = Z_1 Z_2 \frac{e^2}{\hbar v} \tag{2.11}$$

E is the total energy of the interaction, Z_1, Z_2 are the atomic numbers of interacting particles, and v is the relative velocity of the incoming particle. $1/E$ is called the geometrical factor which is proportional to the the De Broglie wavelength squared ($\pi\lambda^2 \propto 1/E$). The $\exp(-2\pi\eta)$ is the probability factor of tunnelling through a Coulomb potential barrier is called Gamow penetration factor. The function $S(E)$ carries a pure intrinsic property of the nuclear interaction which varies smoothly in the absence of resonances. The value of $S(E)$ at zero energy is known as the cross section factor, S_0 , which is measured experimentally. The ^{8}B neutrino flux $\phi(^8\mathrm{B})$ has a dependence on the S-facotrs such as

$$\phi(^8\mathrm{B}) \propto S_{11}^{-2.6} S_{33}^{-0.4} S_{34}^{0.81} S_{17}^{1.0} \tag{2.12}$$

where the notation of the S-factor is listed in Table 2.1

Reaction	S-factor
^{1}H $(p, e^+\nu_e)$ ^{2}H	S_{11}
^{3}He $(^3He, 2p)$ ^{4}He	S_{33}
^{3}He $(^4He, \gamma)$ ^{7}Be	S_{34}
^{7}Be (p, γ) ^{8}B	S_{17}

Table 2.1: Notation of S-factor

Radiative opacity

The radiative opacity plays a key role in the SSM since the photon radiation is the main contribution of the energy transport in the central part of the Sun. The calculation of the opacity depends on the chemical composition and on the modeling of the atomic reactions.

Heavy metal abundance

The initial mass ratio of elements heavier than helium (Z) relative to hydrogen (X), Z/X is a very important input parameter in the calculation of SSM. The fractional abundances of each element determines the stellar opacity, which is closely related to the neutrino fluxes.

Helioseismology

Helioseismology studies how the wave oscillation, particularly acoustic pressure wave (p-mode), propagates in the Sun. The calculation of SSMs can be checked by the comparison with the seismic measurements of the depth of the convection zone, sound speed, and density in the Sun.

2.1.3 Current problems of the solar models

In 2005, the input parameters such as S-factor, Opacity, and surface abundances of heavy element(Z)are updated [10]. The largest variation was found in the surface abundances which is about 35% lower than the previous compilation [11]. The variation comes from different

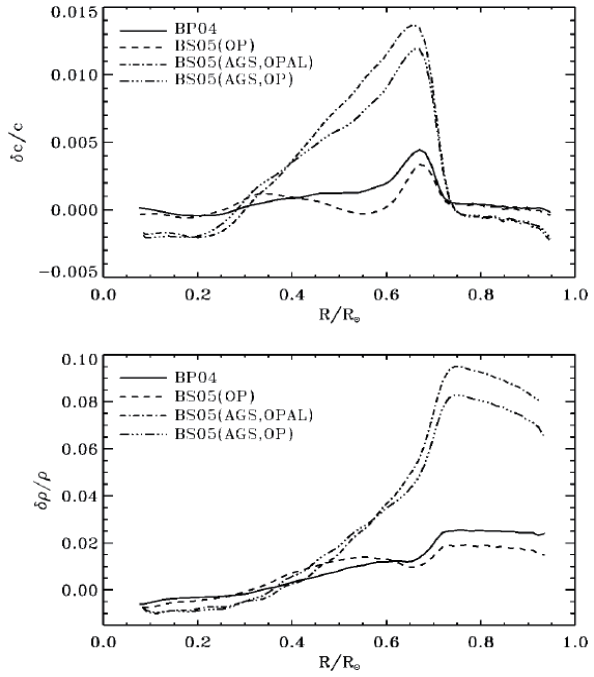

Figure 2.4: Relative sound speed differences, $\delta c/c = (c_{heli} - c_{SSM})/c_{SSM}$, and relative densities, $\delta\rho/\rho$, between solar models and helioseismological results from Michelson Doppler Imager data [9]. The solid line shows the calculation by BP04SSM which is used in this thesis. BS05(OP) uses the previous version of the abundances with the refined opacity calculation done by the Opacity Project [13]. BS05(AGS,OPAL) uses the new abundances with the previously used opacity calculation done by OPAL group [14]. BS05(AGS,OP) uses the new abundances with the opacity of OP group.

improvements and one of them is installing 3D solar atmosphere modeling. The new abundances are in better agreement with the gaseous medium between stars in our neighborhood of the galaxy, and the agreement between photospheric and meteoritic abundances becomes very good. However, the sound speed and the density calculated by the new SSM conflicts with the seismic measurement. On the other hand, if the previous abundances [12] are used, the agreement between SSM calculation and the seismic measurement is very good as shown in the Figure 2.4

Considering this situation, the two set of SSMs were published; one includes all the latest information (hereafter BS05(AGS,OP)), and the other one includes all updates except for the abundances (hereafter BS05(OP)). Specifically, BS05(AGS,OP) uses $Z/X = 0.0165$ (so called "low Z model") while BS05(OP) uses $Z/X = 0.0229$ (so called "high Z model"). OP means that the latest version of the opacity calculation which is done by Opacity Project is used [13]. This conflict between the SSM calculation and the helioseismology measurement has not been solved yet, and is under discussion [15].

What can we say from solar neutrino experiments?
It is suggested that a precise measurement of ^{8}B neutrino flux may tell what the real abundance

Neutrino type	BP04	BS05(GS98)	BS05(AGS05)
pp	5.94	5.99	6.06
pep	1.40	1.42	1.45
^{7}Be	4.86	4.84	4.38
^{8}B	5.79	5.69	4.59
hep	7.88	7.93	8.25
N	5,71	3.07	2.01
O	5.03	3.33	1.47
F	5.91	5.84	3.31

Table 2.2: Total flux for each neutrino type predicted by the SSMs. This table presents the predicted fluxes, in units of 10^{10}(pp), 10^{9}(^{7}Be), 10^{8}(pep, ^{13}N, ^{15}O), 10^{6}(^{8}B, ^{17}F) , and 10^{3}(hep) cm^{-2} s^{-1}

SSM	$+\sigma$(%)	$-\sigma$(%)
BP04	23	23
BS05(OP)	17.3	14.7
BS05(AGS,OP)	12.7	11.3

Table 2.3: The uncertainty of the SSMs prediction on the ^{8}B flux.

is. Since the dependence of the abundances on the ^{8}B neutrino flux $\phi(^{8}\mathrm{B})$ is given by

$$\phi(^{8}\mathrm{B}) \propto \left(\frac{Z}{X}\right)^{1.3} \tag{2.13}$$

which is relatively large dependence, the ^{8}B neutrino flux value predicted by BS05(AGS,OP) is smaller than BS05(OP) by $\sim$ 30%. Therefore, if experiments can measure the flux within 5%, then the result will improve the understanding of the solar interior [10]. This is one of the motivations of this thesis.

2.1.4 Solar Neutrinos predicted by SSM

In this section, some basic results from the SSM prediction are shown. Table 2.2 shows the total flux for each neutrino source predicted by the different versions of the SSM. and the uncertainties of the ^{8}B neutrino flux predictions are shown in Table 2.3. The electron density profile and production point of each neutrino source are shown in the Figure 2.5 and 2.6, respectively.

2.2 Energy spectrum of ^{8}B

In this thesis, I used the neutrino energy spectrum from the β^{+} decay of ^{8}B calculated by Ortiz et.al.[17]. The neutrino spectrum can be obtained from the measurement of energy

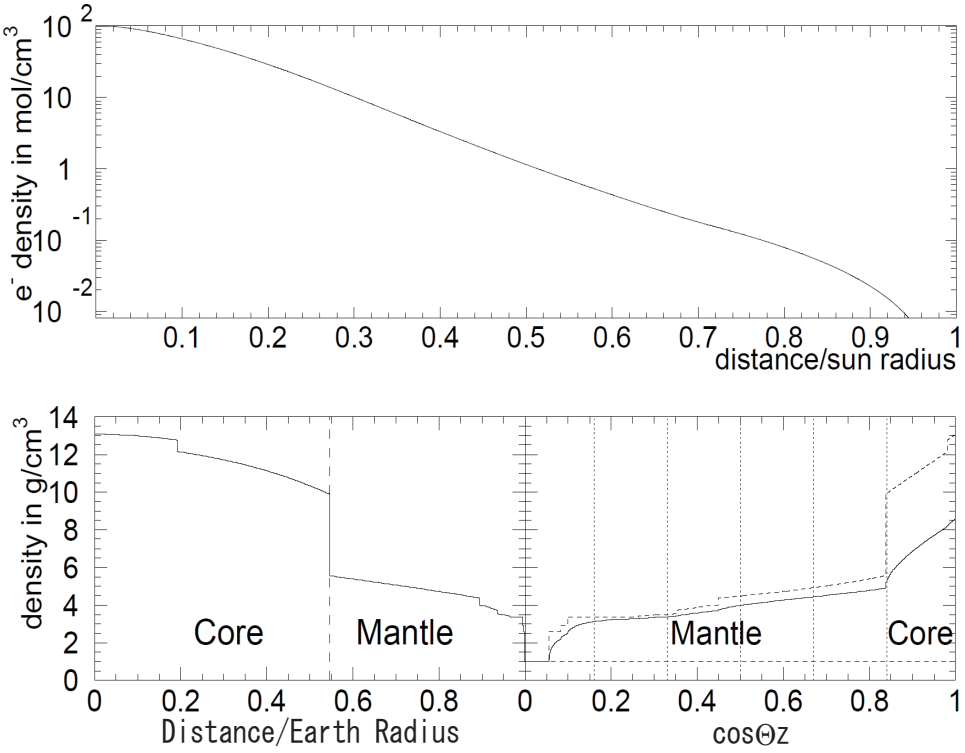

Figure 2.5: Upper: Electron density calculated by SSM. Lower: Electron density in the Earth (PREM) [16] which is used in the calculation of neutrino oscillation in the Earth.

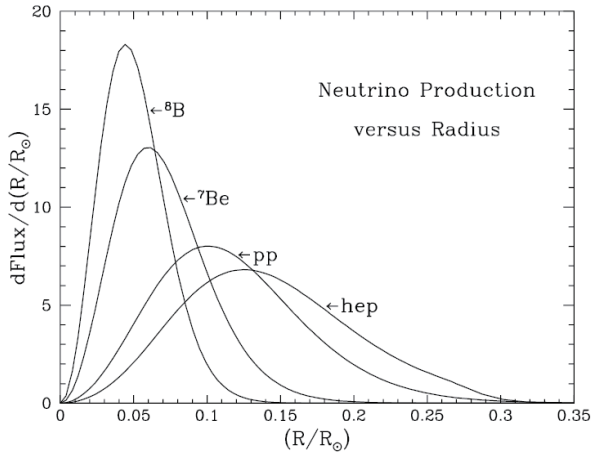

Figure 2.6: Production point for each solar neutrino. Horizontal axis shows the distance from the center of the Sun in unit of the solar radius. Vertial axis shows the solar neutrino flux as a function of the distance.

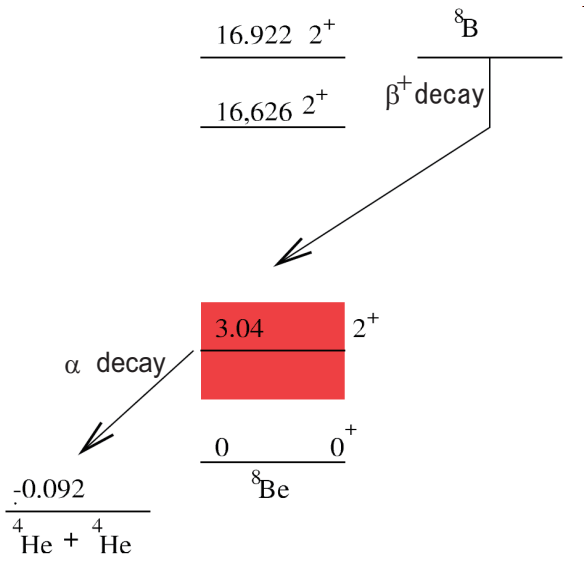

Figure 2.7: Decay scheme of ^8B.

spectrum of the α particle from ^{8}Be which is the daughter nucleus of ^{8}B (see Figure 2.7). In their estimation of uncertainty, however, a theoretical uncertainty to calculate the neutrino energy from the alpha spectrum which are considered in [18] is not fully taken into account. Thus the uncertainty of ^{8}B spectrum from reference [18] is used. In 2006, Winter obtained the ^{8}B spectrum after a very precise measurement of the alpha spectrum. Because of the improvement on both the measurement and the calculation method, the uncertainty of the spectrum becomes smaller. The Winter spectrum and the difference between Ortiz and Winter are shown in Figure 2.8. Thus, I also studied the effect of the uncertainty of Winter to the uncertainty of the total flux of our measurement for future analysis improvements. The detail of estimation of systematic uncertainty will be discussed in Chapter 9.

2.3 Neutrino Oscillation of Solar Neutrinos

The neutrino oscillation is the only experimental observation which cannot be explained by the standard model of elementary particle physics. A brief explanation of the essence of the neutrino oscillation is given in this section.

2.3.1 Neutrino Oscillation in vacuum

For simplicity, let us consider the neutrino oscillation between only two flavors, for example ν_e and ν_x. The mixing of the two-neutrino oscillation in vacuum is

$$\begin{pmatrix} \nu_1 \\ \nu_2 \end{pmatrix} = \begin{pmatrix} \cos\theta & \sin\theta \\ -\sin\theta & \cos\theta \end{pmatrix} \begin{pmatrix} \nu_e \\ \nu_x \end{pmatrix} \tag{2.14}$$

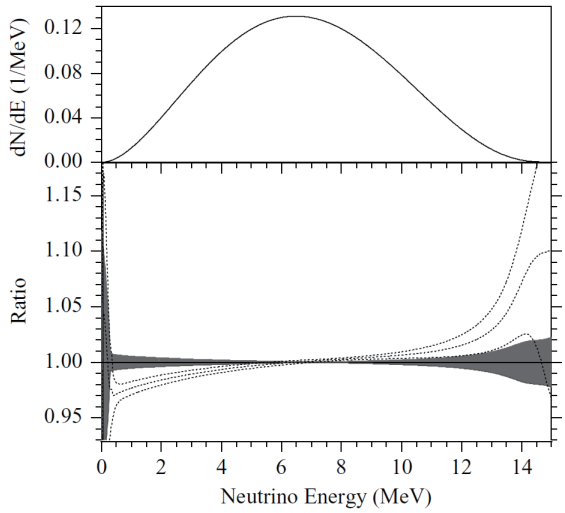

Figure 2.8: ^8B neutrino energy spectrum [19]. Upper plot shows the neutrino energy spectrum, and lower plot shows the comparison with the Ortiz spectrum [17]. Dashed lines show the ratio between the Ortiz spectrum and $\pm 1\sigma$ experimental uncertainty, to the Winter spectrum. Black band represents the $\pm 1\sigma$ experimental uncertainty of the Winter spectrum.

where θ is called the mixing angle. This flavor mixing gives an oscillating survival probability for a neutrino with energy $E(MeV)$ traveling a distance $L(m)$ as

$$p_{e\to x} = p_{x\to e} = \sin^2 2\theta \sin^2\left(\pi \frac{L}{L_{osc}}\right) \tag{2.15}$$

where L_{osc} is defined by

$$L_{osc} \equiv \frac{\pi}{1.27}\frac{E}{\Delta m^2} \tag{2.16}$$

and $\Delta m^2 = m_2^2 - m_1^2(\mathrm{eV}^2)$ is the squared mass difference of mass eigenstate 1 and 2.

2.3.2 Neutrino Oscillation in matter

In matter, neutrinos feel the potential of weak interaction. While ν_e has a chance of both charged current interaction and neutral current interaction, the other type of neutrinos have only neutral current interaction. The Hamiltonian $\mathcal{H}$ in the two neutrino case can be expressed in the following form, omitting the common multiple factor.

$$\mathcal{H} = \mathcal{H}_v + \mathcal{H}_M \tag{2.17}$$

$$= \frac{\Delta m^2}{4E}\begin{pmatrix} -\cos 2\theta & \sin 2\theta \\ \sin 2\theta & \cos 2\theta \end{pmatrix} + \begin{pmatrix} V & 0 \\ 0 & 0 \end{pmatrix} \tag{2.18}$$

where $\mathcal{H}_v$ is the Hamiltonian in vacuum, and the $\mathcal{H}_M$ is that of in matter. V is the potential of the charged current interaction,

$$V = \sqrt{2} G_F N_e \tag{2.19}$$

where G_F is Fermi coupling constant and N_e is the electron density in the matter. By putting the Hamiltonian to the Schroedinger equation, the eigenvector is given as

$$\begin{pmatrix} \nu_1^M \\ \nu_2^M \end{pmatrix} = \begin{pmatrix} \cos\theta_M & \sin\theta_M \\ -\sin\theta_M & \cos\theta_M \end{pmatrix} \begin{pmatrix} \nu_e \\ \nu_x \end{pmatrix} \tag{2.20}$$

where ν_1^M and ν_2^M are mass eigenstates of neutrinos in matter, and θ_M is the mixing angle in matter which is

$$\tan 2\theta_M = \frac{\frac{\Delta m^2}{E}\sin 2\theta}{2V + \frac{\Delta m^2}{E}\cos 2\theta}\ , \tag{2.21}$$

The survival probability can be obtained by replacing θ in equation 2.15 with θ_M, and L_{osc} with the oscillation length in matter L_M which is

$$L_M = \frac{\pi}{1.27\sqrt{(2V + \frac{\Delta m^2}{E}\cos 2\theta)^2 + (\frac{\Delta m^2}{E}\sin 2\theta)^2}} \tag{2.22}$$

2.3.3 The effect of neutrino oscillation

As described in [20], in the case of solar neutrino propagation, matter effects in the Sun and the Earth are taken into account. The calculation of the survival probability of a solar neutrino at our detector has in principle three steps: 1) from the production point of the solar neutrino to the surface of the Sun, 2) from the surface of the Sun to the surface of the Earth, and 3) from the surface of the Earth to the detector. In practice, since we already know from the previous experimental results that the distance between the Sun and the Earth is much lager than the vacuum oscillation length of the favored parameter $\Delta m^2/E > \sim 10^{-9} eV^2/MeV$, the propagation of ν_1 and ν_2 at 2) can be assumed to be incoherent. This makes the calculation more simple, so that we only need the probability of ν_e to be produced in the core of the Sun to appear as ν_1 (or ν_2), which is written as p_1 (or p_2), and the probability of ν_1 (or ν_2) at the surface of the Earth to be observed as ν_e in the detector, which is written as p_{1e} (or p_{2e}). The total survival probability of the ν_e, p_e is then obtained by

$$p_e = p_1 \times p_{1e} + p_2 \times p_{2e} = 2p_1 p_{1e} + 1 - p_1 - p_{1e} \tag{2.23}$$

where p_1 and p_{1e} are numerically calculated, and

$$\begin{aligned} p_2 &= 1 - p_1 \\ p_{2e} &= 1 - p_{1e} \end{aligned}$$

The details can be found in [21]

2.4 Solar Neutrino Experiment

In this section, introductions of the solar neutrino experiments (except for the Super-Kamiokande) are given. A summary of all solar neutrino experimental results is shown at the end of this section.

2.4.1 Radiochemical experiment

Cl target experiment

The first experiment which tried to observe solar neutrinos is the chlorine experiment in Homestake, USA. The neutrino target was 2.2×10^{30} atoms (133 tons) of ^{37}Cl in the form of 3.8×10^5 liters (615 tons) of liquid perchloroethylene, C_2Cl_4. The tank was located at the Homestake mine at 1478m depth(4100m of water equivalent (m.w.e)). The experiment period is from 1967 to 1994 [22]. The neutrino rate is measured by

$$\nu_e + ^{37}\text{Cl} \rightarrow e^- + ^{37}\text{Ar (threshold 814keV)} \tag{2.24}$$

The ^{37}Ar atoms produced by solar neutrino are extracted from the tank by purging it with He gas with 95% efficiency. With half life($\tau_{1/2}$) of 34.8 days, the decay of ^{37}Ar through orbital electron capture produces Auger electrons. The number of produced ^{37}Ar is obtained from count of Auger electrons in the proportional counter. Given the threshold value(=814keV), ^{8}B neutrinos contribute about 77% of predicted event rate.

Ga experiment

GALLEX(1991-1997)/GNO(1998-2003) [23, 24] in Gran Sasso, Italy and SAGE(1900-2001) [25] in Baksan, Russia use ^{71}Ga as the neutrino target. The detectors of GALLEX/GNO and SAGE locate at 3800m.w.e. and 4700 m.w.e. underground, respectively. The target volumes of GALLEX/GNO and SAGE are 30tons(GNO used 60 tons since 1991) and 60 tons. The neutrino rate is measured by

$$\nu_e + ^{71}\text{Ga} \rightarrow e^- + ^{71}\text{Ge (threshold 233keV)} \tag{2.25}$$

Like the Cl experiment the ^{71}Ge atoms are chemically extracted and introduced to a proportional counter to count the Auger electrons (half live of ^{71}Ge is 11.43 days). The low threshold enables to observe all the sources of solar neutrinos including the pp neutrinos.

2.4.2 Kamiokande

Kamiokande (1987-1995)[26] is a water Cherenkov detector with 3kton of pure water in Kamioka mine, Japan. The solar neutrinos are detected using the reaction:

$$\nu + e^- \rightarrow \nu + e^- \tag{2.26}$$

where the angular correlation between the incoming neutrino and the recoil electron is very strong. The Cherenkov photons emitted by the recoil electron are detected by 20-inch photo - multiplier tubes. The first real-time observation of solar neutrino was carried out by Kamiokande showing that the direction of recoil electron is pointing in the direction of the Sun. This observation principle is basically the same as in Super-Kamiokande.

2.4.3 Borexino

Borexino is currently running low background liquid scintillator detector since 2007 [27]. The detector is located at 3800m.w.e. in Gran Sasso, Italy. The fiducial volume is 87.9 ton. The solar neutrinos are detected by means of their elastic scattering of electrons. The light yield

of the scintillator which is measured as 500 p.e./MeV enables the real-time detection of ^{7}Be neutrinos, mainly. The neutrino rate can be obtained after statistical subtraction of radioactive background.

2.4.4 SNO

The Sudbury Neutrino Observatory (SNO, 1999-2006) [28, 29, 30] uses 1000 tons of D_2O contained in a spherical vessel. The detector is located at 6010m.w.e. in Sudbury, Canada. SNO mearsures ^8B neutrinos via the reactions

$$\text{Charged Current(CC)}: \quad \nu_e + d \rightarrow p + p + e - 1.442MeV \tag{2.27}$$

$$\text{Neutral Current(NC)}: \quad \nu_x + d \rightarrow p + n + \nu_x - 2.224MeV \tag{2.28}$$

$$\text{Elastic Scattering(ES)}: \quad \nu_x + e^- \rightarrow \nu_x + e^- \tag{2.29}$$

where $x = e, \mu, \tau$. SNO has 3 phases of the experiment, and each phase has different method of the neutron tagging. In Phase I, only pure D_2O is contained, and the neutrons are captured by D_2O with the emission of 6.25MeV γ which is used to tag the NC event [28]. In Phase II, 2tons of NaCl were added to enhance both the neutron capture efficiency and the total γ energy (8.6MeV) [29]. In Phase III, an array of 36 strings of proportional counters filled with ^{3}He are installed to detect the neutrons [30]. Since CC is sensitive only to ν_e and NC is sensitive to all types of neutrinos, SNO can actually measure how many fraction of ν_e oscillate to ν_x by taking ratio of CC rate to NC rate, which is the most significant result from SNO.

2.4.5 Summary of solar neutrino experimental results

Figure 2.9 summarize the results of solar neutrino experiment. The neutrino oscillation is not taken into account for the SSM predictions in that figure. If the neutrino oscillation is considered, then the SSM and the experimental results agree very well as shown in Figure 2.10 In the Figures, the unit of SNU for Ga, Cl experiment stands for "Solar Neutrino Unit" which is defined as 10^{-36} captures per target atom per second. To obtain the expectation flux with neutrino oscillation in Figure 2.10, the favored Large Mixing Angle (LMA) area ($\Delta m^2 = 6 \times 10^{-5} eV^2, \tan^2\theta_{12} = 0.4$) is assumed.

2.5 Motivation and strategies of this thesis

The biggest remaining problem is to find the MSW effect in solar neutrinos. Figure 2.11 shows the survival probability of ν_e as a function of neutrino energy. Super-Kamioande can observe the energy spectrum in terms of the total electron energy which is deposited by a recoil electron. Figure 2.12 shows the spectrum observed in the first phase of Super-Kamiokande experiment (SK-I) and predicted spectrum shapes with different oscillation parameters. As shown in Figure 2.12, it is still difficult to decide whether the distorted spectrum is correct or not because the sizes of the statistical uncertainty in lower energy region and the systematic uncertainty in higher energy region are large. Likewise, no other experiment has observed the distorted spectrum successfully. Therefore, the final goal of this thesis is to observe the distorted spectrum. The following improvements are necessary to observe the spectrum distortion as soon as possible.

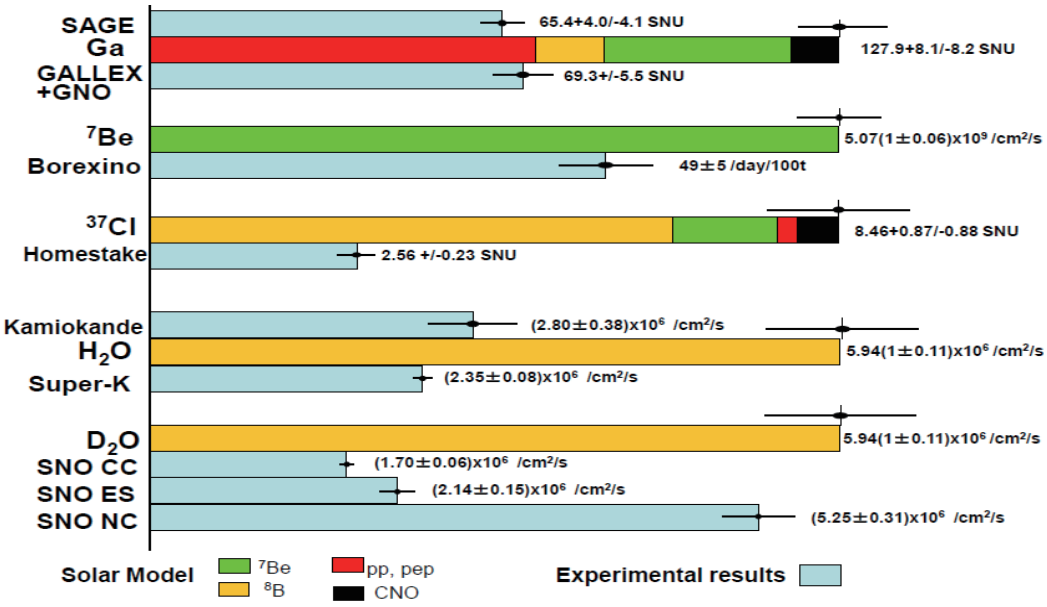

Figure 2.9: Comparison between various experimental results and SSM. The neutrino oscillation is not taken into account.

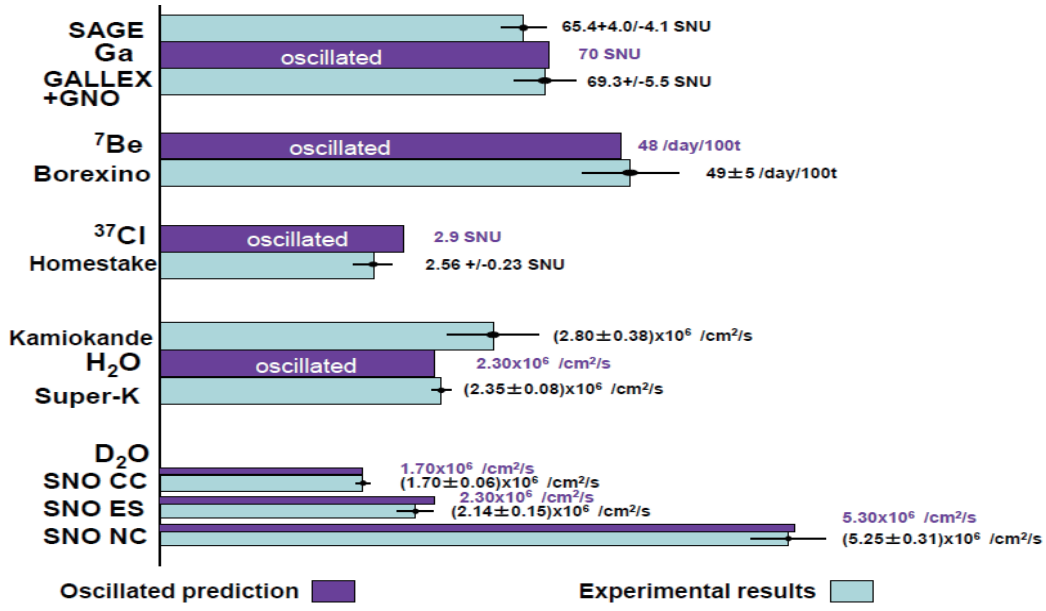

Figure 2.10: Comparison between various experimental results and SSM. The neutrino oscillation is taken into account.

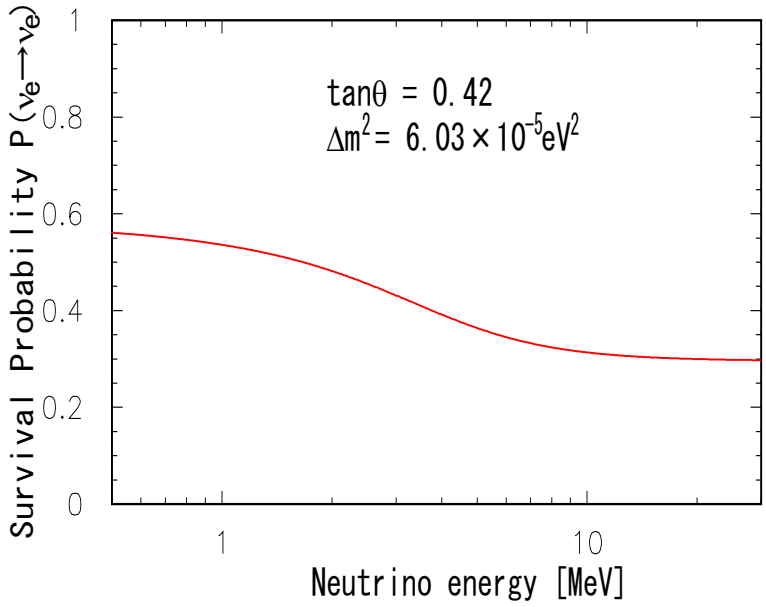

Figure 2.11: Survival probability of electron neutrino with the solar best fit 2 flavor oscillation parameters.

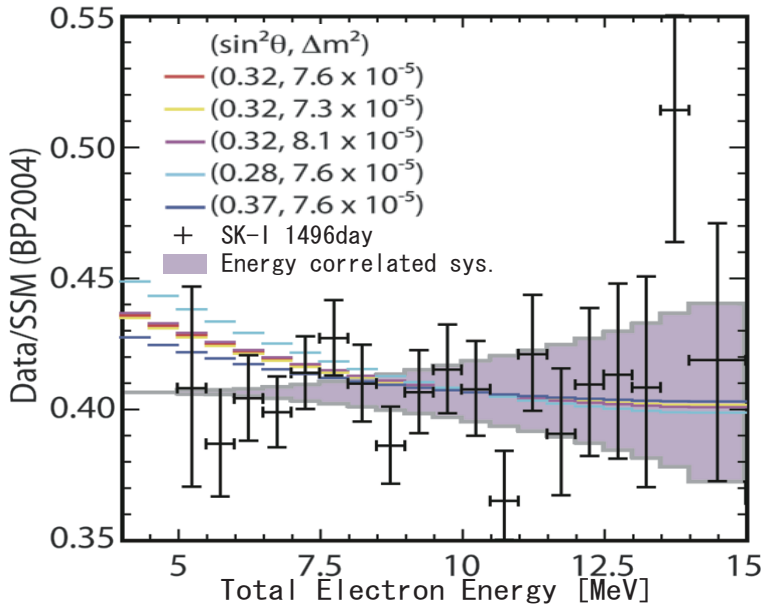

Figure 2.12: Observed energy spectrum/SSM. The color histograms show expected value for different oscillation parameters, and the gray band shows the energy correlated systematic uncertainty.

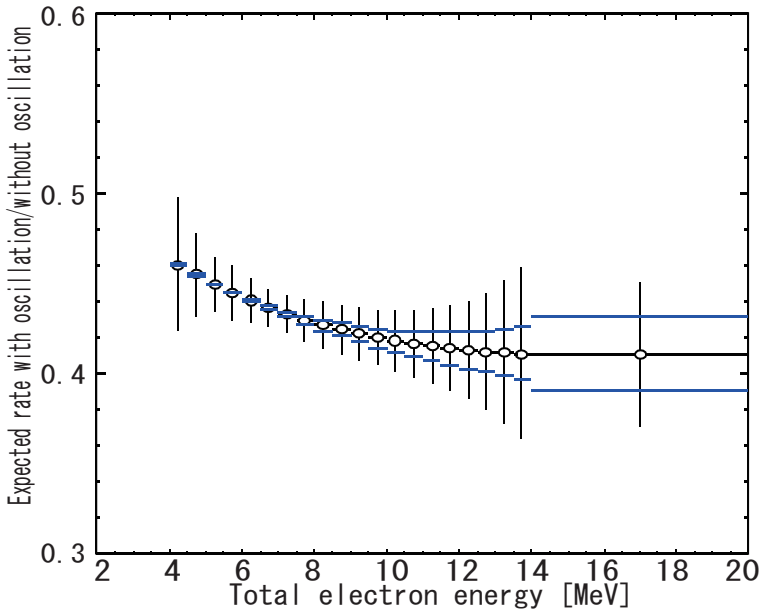

Figure 2.13: Expected energy spectrum after 5 years observation. The black histogram shows the expect value with expected statistical uncertainty with 70% background reduction below 5.5 MeV region. The blue band shows half size of energy correlated uncertainty as SK-I.

First, the number of background must be reduced to make the statistical uncertainty smaller especially in the lower energy region (<5.5MeV). This is because the size of statistical uncertainty is approximately the size of the square root of (statistical uncertainty of background)^2 plus (statistical uncertainty of signal)^2 and the statistical uncertainty of background is dominant for the low-energy region. The numerical goal is to reduce 70% of background from SK-I level in the lower-energy region. It was known from radioactive measurement of detector water that 40% of remaining low energy background around 5MeV was due to radioactive impurities in the water during SK-I, thus 40% reduction was expected because the water purification system and circulation system had been upgraded since SK-I. The other 60% of background was considered to be miss-reconstructed events which originally occurred in the edge of the detector but were reconstructed inside the fiducial volume. Such miss-reconstructed events could be reduced by half if new reconstruction tools and reduction tools are developed.

Second, the energy correlated systematic uncertainty must be reduced by 50% compared to SK-I. To reduce the systematic uncertainty, the most important thing is to understand the detector response. Thus, careful calibrations and tuning of the detector simulation are key to make the reduction possible. Another strategy is to update the theoretical calculation of ^{8}B spectrum as already discussed in Section 2.2.

Figure 2.13 shows predicted energy spectrum after 5 years observation with reduced background and systematic uncertainty. By comparing with Figure 2.12, we can see the upturn of the distorted spectrum with the reduced size of uncertainties. In this thesis, because the total livetime is about one third of SK-I, it is difficult to confirm the upturn statistically, however, these improvements which will be discussed in the following chapters must set the foundation for the future observation of the MSW effect in the Sun.

Chapter 3

Super-Kamiokande Detector

3.1 Detector outline

Super-Kamiokande is a cylindrical water Cherenkov detector with 50kton of ultra-pure water. The diameter of the detector is 39.3m, and the height is 41.4m. The detector location is 1000m underground (2700 m.w.e.) in the Kamioka mine, Gifu Pref., Japan, The latitude and longitude are 36°25' N and 137°18' E, respectively. The downward-going cosmic-ray muon rate is about 2Hz which is 10^{-5} times smaller than that at the ground level. The outside 2m of the detector is called the Outer Detector (OD) corresponding 18kton of volume, and the inside 32kton is called the Inner Detector (ID). ID and OD are separated by plastic black sheet and stainless steel structure on which ID and OD photo-multiplier tubes (PMTs) are assembled. The purpose of OD is to veto events from outside rock and reject cosmic-ray muon events. The fiducial volume is 22.5kton, 2m inside from the ID wall.

Figure 3.1 is a brief description of the detector in each phase of the experiment. As shown in the figure, SK has three phases of the experiment which are called SK-I, II, and III[1] After the full reconstruction in 2006, 11129 20-inch PMTs in ID, and 1885 8-inch PMTs in OD are installed. The photodetector coverage is 40% in ID. The detail information about the detector can be found in [31].

The update items from SK-I(or II) are

- ID PMTs are covered by FRP and acrylic case.
- Water purification system is upgraded (see the section 3.4)
- Detector calibration is improved.
- OD is segmented by Tyvek which improved the Cosmic-ray muon identification (see Figure 3.9).

3.2 20-inch PMT

R3600-06 HAMAMATSU PMT are used for ID PMT. Figure 3.2 shows a schematic view of a 20-inch PMT and the bleeder circuit. In Figure 3.3, the basic specifications of those PMTs are listed. Figure 3.4 shows basic distributions measured by HAMAMATSU [32].

[1]SK-IV has started since Sep.6 2008 with new electronics and DAQ system.

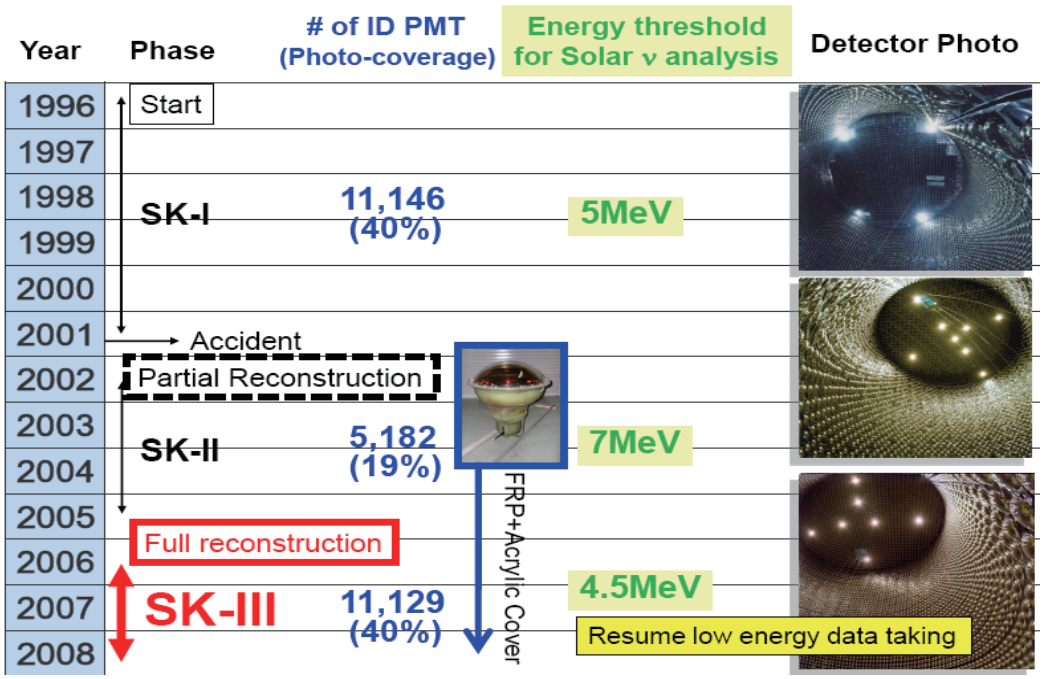

Figure 3.1: Time-line of each phase of Super-Kamioande experiment.

[2]

Figure 3.5 shows the transparency of the acrylic cover for photons with normal incidence in water. The transparency is more than 96% for longer wavelength than 350nm, which is reasonably good considering the quantum efficiency of 20-inch PMT (see Figure 3.4).

3.3 Data acquisition (DAQ) system

Figure 3.6 shows a schematic view of the DAQ system. The signal from each ID PMT is sent to each channel of front-end electronics called Analog Timing Module (ATM) [33, 34] through a 70m coaxial cable. The ATM is developed based on the TKO standard [35]. 12 PMTs are connected to one ATM, which records and digitizes the integrated charge and the arrival timing information with a 12-bit ADC. Each ATM channel has 2 buffer channels (a and b) to process successive events, such as a muon and the decay electron after the muon. Thus, one ATM has 24 channels (0a to 11b). The ATM characteristics is summarized in Table 3.1

The analog input of the ATM is made following the block giagram which is shown in Figure 3.7. If a hit exceed a threshold (0.25p.e.), the signal charge is integrated at Charge to Analog Converter (QAC) with a 400 nsec gate, and Time to Analog Converter (TAC) starts to integrate charge with a constant current to measure the time interval between the start time generated by

[2]Radiant sensitivity is the photoelectric current from the photocathode, divided by the incident radiant power at a given wavelength, expressed in A/W (amperes per watt). Quantum efficiency (QE) is the number of photoelectrons emitted from the photocathode divided by the number of incident photons. Quantum efficiency is usually expressed as a percent. Quantum efficiency and radiant sensitivity have the following relationship at a given wavelength.

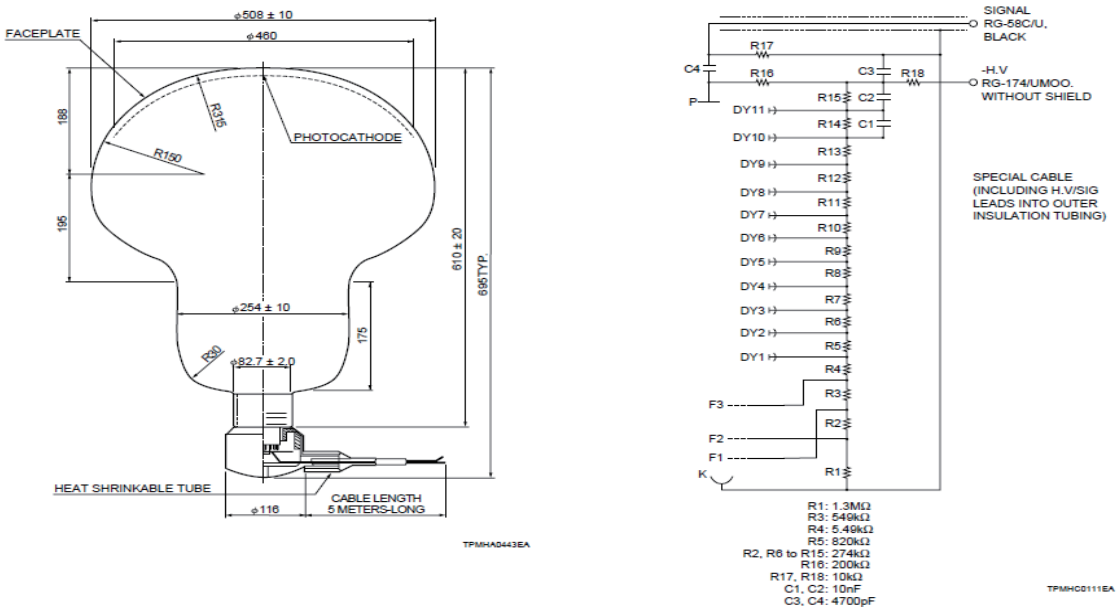

Figure 3.2: Schematic veiw of the 20-inch PMT and the bleeder circuit [32].

Number of channels	12 ch/board
One hit processing time	$\sim 5.5\mu$sec
Charge dynamic range	$\sim$ 400 to 600pC (12bit)
Timing dynamic range	$\sim$ 1300nsec (12bit)
Charge resolution (LSB)	0.2 pC/LSB
Charge resolution (RMS)	0.2 pC (RMS)
Timing resolution (LSB)	0.3 $\sim$ 0.4nsec/LSB
Timing resolution (RMS)	0.4 nsec (RMS)
Temperature dependence (QAC)	3 Count/deg. $\leftrightarrow$ 0.6 pC/deg.
Temperature dependence (TAC)	2 Count/deg. $\leftrightarrow$ 0.8 nsec/deg.
Envent number	8 bit
Data size of one hit	6 Byte
FIFO	2 kByte ($\sim$ 340 hits)

Table 3.1: Specifications of the ATM module

GENERAL

Parameter		Description/Value	Unit
Spectral Response		300 to 650	nm
Wavelength of Maximum Response		420	nm
Photocathode	Material	Bialkali	—
	Effective Area	2400	cm^2 Typ.
Window Material		Borosilicate glass	—
Dynode	Structure	Venetian blind	—
	Number of Stages	11	—
Direct Interelectrode Capacitances (Approx.)	Anode to Last Dynode	36	pF
	Anode to All Other Dynode	40	pF
Base		20-pin base JEDEC B20-102	—
Weight	R3600-02	8	kg
	R3600-06	10	kg
Suitable Socket		E678-20A (supplied)	—

CHARACTERISTICS (at 25°C)

Parameter		Min.	Typ.	Max.	Unit
Cathode Sensitivity	Luminous (2856K)	—	60	—	µA/lm
	Radiant at 420nm	—	65	—	mA/W
	Blue (CS 5-58 filter)	—	8.0	—	µA/lm-b
	Quantum Efficiency at 390nm	—	20	—	%
Anode Sensitivity [1]	Luminous (2856K)	—	600	—	A/lm
	Radiant at 420nm	—	6.5×10^5	—	A/W
Gain [1]		—	1.0×10^7	—	—
Supply Voltage for Gain of 10^7		—	2000	2500	V
Anode Dark Current (after 30min. storage in darkness) [1]		—	200	1000	nA
Dark Count (after dark condition for 15 hours) [1]		—	25	80	kcps
Time Response [1]	Anode Pulse Rise Time	—	10	—	ns
	Electron Transit Time	—	95	—	ns
	Transit Time Spread (FWHM) [2]	—	5.5	—	ns
Single Photoelectron	PHD (Peak to Valley Ratio)	—	1.7	—	—
Magnetic characteristics (at 200mG/20µT)	Sensitivity Degradation	—	15	—	%

1) Measured with the condition shown in below. 2) Measured with 0.25 photoelectrons detection threshold (at single photoelectron/ event).

VOLTAGE DISTRIBUTION RATIO AND SUPPLY VOLTAGE

Electrodes	K	F2	F1	F3	Dy1	Dy2	Dy3	Dy4	Dy5	Dy6	Dy7	Dy8	Dy9	Dy10	Dy11	P
Ratio	5	1	2	0.02	3	1	1	1	1	1	1	1	1	1	1	
Capacitors in µF													0.01	0.01	0.01	

Supply Voltage: 2000Vdc, K: Cathode, Dy: Dynode, P: Anode, F: Focus

Figure 3.3: Specifications of the 20-inch PMT [32]

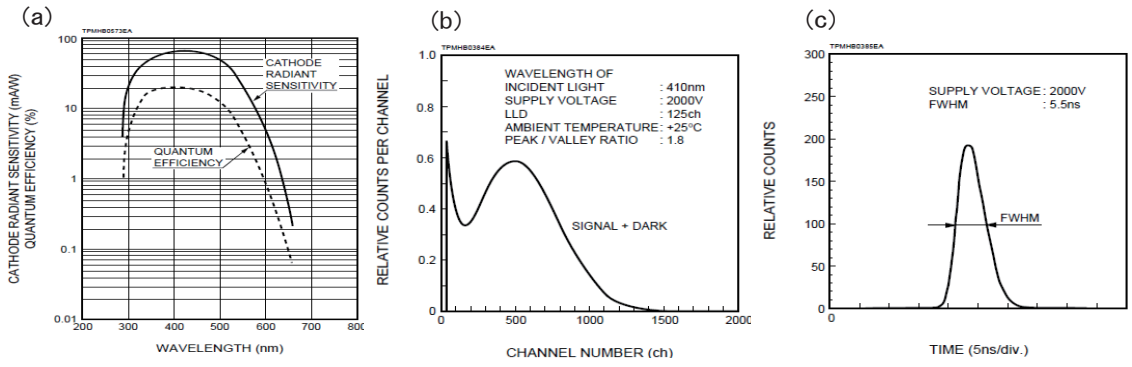

Figure 3.4: Basic distributions of 20-inch PMT (a) Cathode radiant sensitivity and Quantum efficiency. (b) 1p.e. charge distribution (c) Transit time distribution [32]

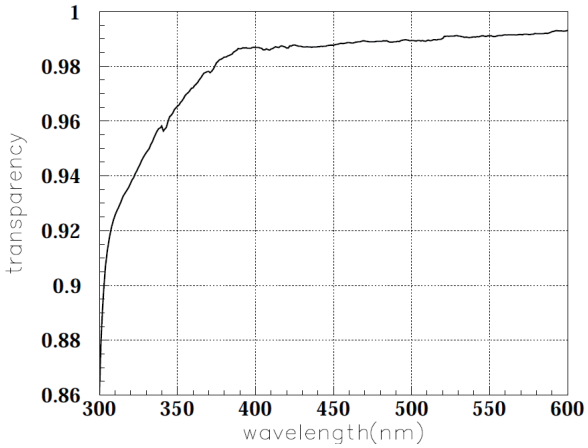

Figure 3.5: Transparency of acrylic cover as a function of the photon wavelength.

the hit signal and the stop signal which will be generated by a global trigger. After the global trigger arrived, the integrated charge in QAC and TAC are digitized in ADC. (Note that the output of a hit timing is the time interval between the hit and the global trigger, and thus, the bigger value of the output timing corresponds to earlier hit.) On the other hand, if there is no global trigger within 1.3μsec, the charges in QAC and TAC are cleared.

Every 16 events, the digitized data in the ATM are sent to VME memory module called Super Memory Partner (SMP). One SMP handle 20 ATMs and there are 8 slave computers each reading out 6 SMP memories. One sequence of data flow ends with the online host computer to which the slave computer sends its data.

More detailed information about the DAQ system is described in [31].

Trigger

The global trigger is made in the following process. At each ATM, in parallel with the processes in QAC and TAC, a hit signal is converted to a square pulse, then the ATM generate one HITSUM signal of 200nsec width by taking analog-sum of all the square pulses from 12 PMTs. The height of the summed HITSUM is proportional to the number of hit PMTs in the ATM. All HITSUMs are collected and AC-coupled into a discriminator to subtract offset due to dark noise hits. At this point, one hit corresponds to -11mV of the pulse height. If the summed HITSUM signal exceed a discriminator threshold, a global trigger is generated and then it fed to a VME TRiGger module (TRG) which issues the global trigger and the event number to be distributed to ATMs.

There are three types of the threshold values depending on the analysis region: Super Low Energy trigger (SLE), Low Energy trigger (LE), and High Energy trigger (HE). Table 3.2 shows the summary of each trigger setting. There also exists OD trigger, which has similar to that of ID and independent of the ID system. The OD trigger threshold is set to 19 OD hits in 200 nsec.

Since most of the SLE triggered events are caused by gamma-rays from the surrounding rock, and radioactive decay in the PMT and FRP, the vertex positions of such low energy

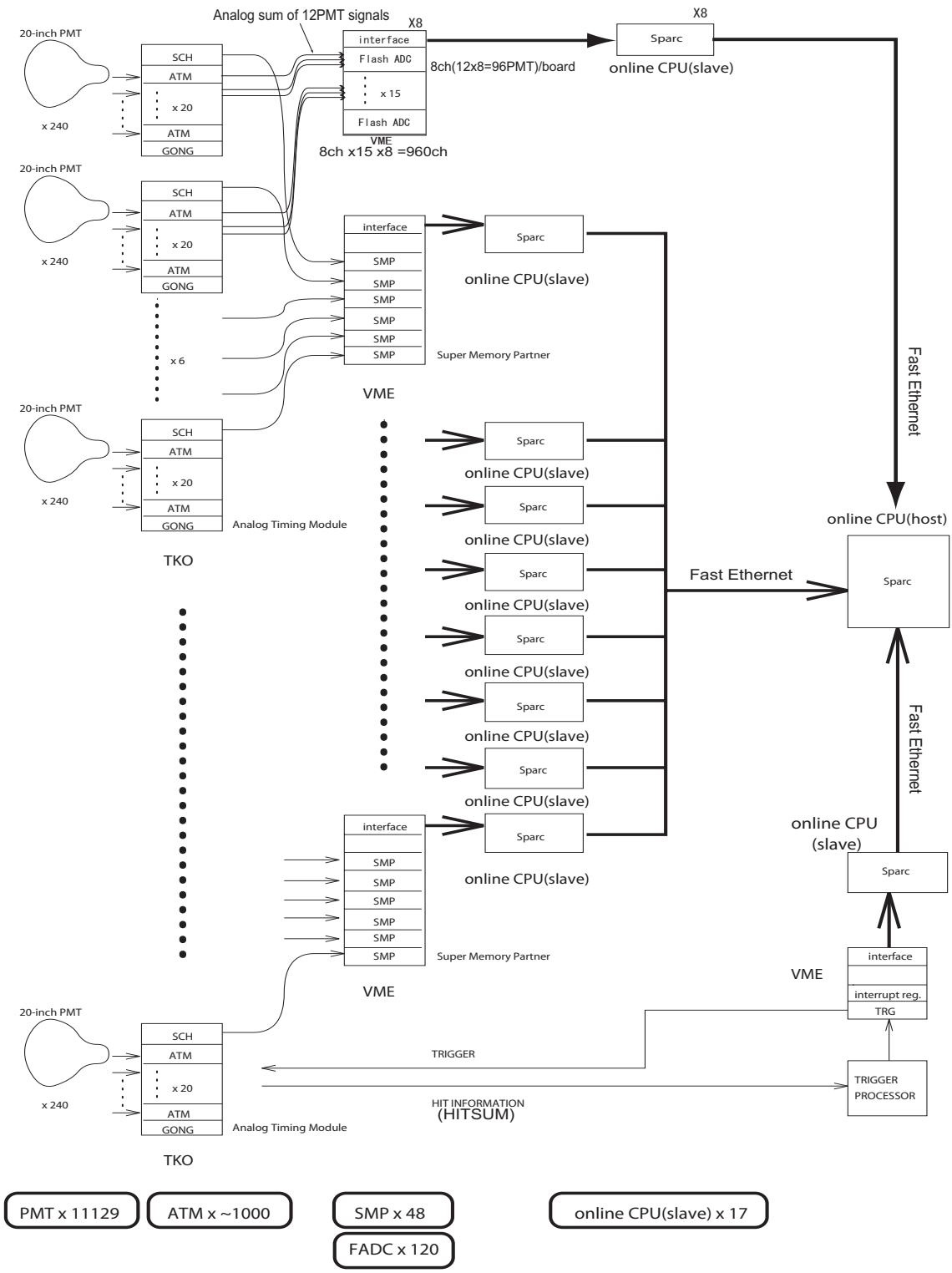

Figure 3.6: Schematic view of DAQ system

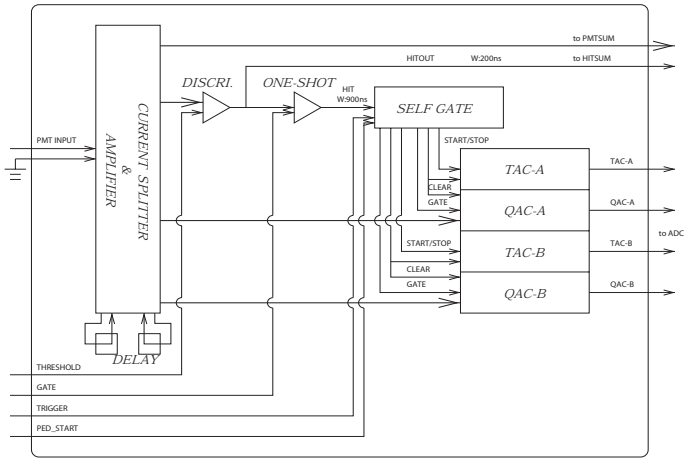

Figure 3.7: Block diagram of ATM.

Trig. Type	Thre. (mV)	Hits	Trg. Rate (Hz)
SLE1	-212	19	$\sim 1.3k$
SLE2	-186	17	$\sim 3.5k$
LE	-302	27	~ 30
HE	-320	29	~ 10

Table 3.2: Summary of trigger settings in SK-III. SLE1 and SLE2 are set in different periods. SLE1 is from Jan 2007 to Apr 2008, and SLE2 is from Apr 2008 to Aug 2008. LE and HE are used in whole SK-III period. See also Table 7.1. Hits shows corresponding number of hits at the threshold value namely Hits = (Thre. mV)/(-11 mV). About 6 hits correspond to 1MeV of the electron energy.

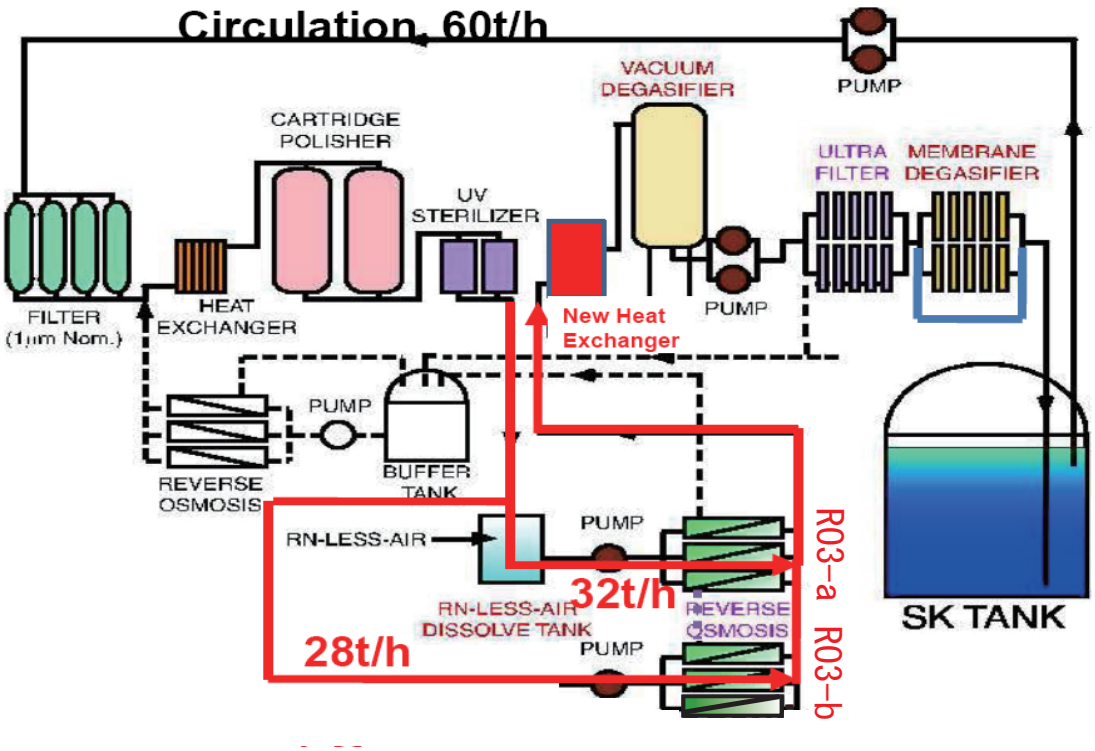

Figure 3.8: Upgraded water purification system.

background events are concentrated in the edge of ID. To reduce the number of events to be stored, a fast vertex fitter, which is a realtime vertex fitter and is applied to only SLE triggered events, was installed to cut events outside the 22.5kton fiducial volume. This software filtering and associated online computer hardware are called the Intelligent Trigger (IT) [20].

3.4 Water purification system

The purified water in the detector is constantly circulated through the water purification system with a flow rate of 60 ton/hour. Figure 3.8 shows the upgraded water purification system. Reverse Osmosis fiters (RO) remove particles, and RO3-a was installed during SK-I after supplying water, but it was used from the begining of SK-III, and a new RO3-b was installed during SK-III. In addition, a new heat exchanger was installed, so that the water temperature can be controlled with $0.1°C$ accuracy. A brief description of the purification system components is summarized in Table 3.3.

Figure 3.9 shows the circulation mode before and after the improvements of the system in SK-III. This final setting has been running since August, 2007. Before the improvements, we tested many circulation modes to achieve a stable and low background rate. It accidentally happened that sometimes radon-rich water contaminates even deep inside the fiducial volume. Such high background periods are eliminated from the final data sample for the very low energy region from 4.5MeV to 6.5MeV. (see Section 7.1).

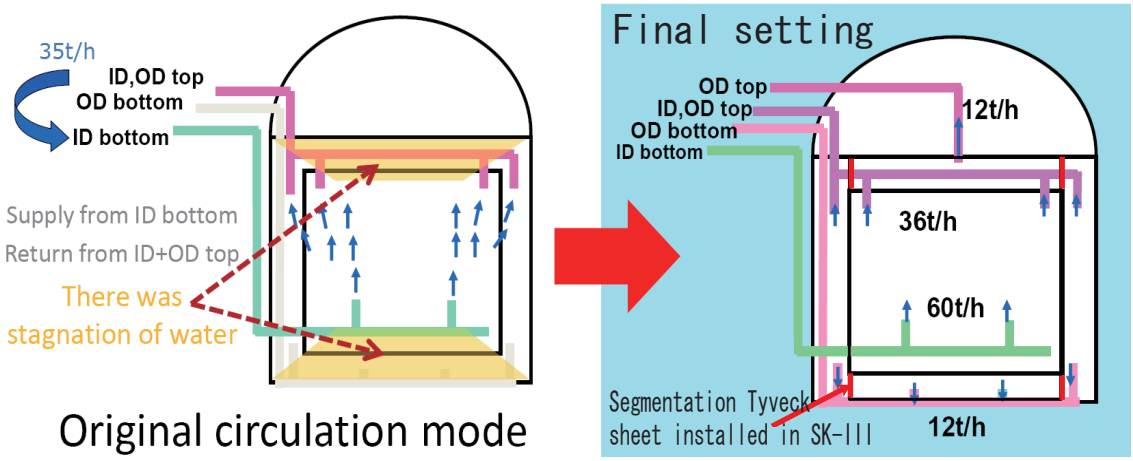

Figure 3.9: Water circulation mode before and after upgrade. OD is also separated by the Tyveck sheet.

Component	Function
1μm filter	Remove dust
Heat exchanger	Cool water heated by pump
Ion exchanger	Remove ions
UV sterilizer	Kill bacteria
Vacuum degasifier	Remove dissolved oxygen and radon gas
Cartridge Polisher	Remove U and Th
Ultra filter	Remove small particle (>$\sim$100nm)
Membrane degasifier	Remove radon gas
Reverse osmosis	Remove small particles (^{226}Ra etc.) (>$\sim$10nm)

Table 3.3: Functions of the components in the water purification system

After the improvements, the background level in the central region of the fiducial volume become significantly lower . This will be discussed in Chapter 10.

Chapter 4

Event reconstruction

The event reconstruction for solar neutrino events will be explained in this chapter. Super-Kamiokande observes the solar neutrino by detecting Cherenckov photons emitted from the recoil electron of the $\nu - e$ elastic scattering:

$$\nu + e^- \longrightarrow \nu + e^- \tag{4.1}$$

Since the recoil electron from a solar neutrino can travel only $\leq\sim$10cm in water, it can be assumed that the Cherenkov photons are emitted from point-like source. First item is vertex reconstruction which finds the interaction point. After the vertex reconstruction, the direction and energy of recoil electron are reconstructed. Figure 4.1 explains the basic variables in the SK detector.

4.1 Vertex reconstruction

The event vertex reconstruction for solar neutrino analysis performs a maximum likelihood fit to the timing residuals of the Cherenkov signal as well as the dark noise background for each testing vertex. This vertex fitter is called BONSAI [36]. The definition of the likelihood is

$$\mathcal{L}(\vec{x}, t_0) = \sum_{i=1}^{Nhit} \log(P(t - tof(\vec{x}) - t_0)) \tag{4.2}$$

Here, $\vec{x}$ and t_0 are the testing vertex position and the peak of hit timing t subtracted by Time Of Flight(tof) from the testing vertex $\vec{x}$ to each PMT position. $Nhit$ is the number of hit PMTs, and P is a probability density function (pdf) which describes timing distribution of a signal event as a function of the hit timing. The pdf is obtained from the shape of the timing residual $(t - tof - t_0)$ distribution from LINAC calibration data which is shown in Figure 4.2, and PMT dark noise is taken into account by constructing the likelihood.

The testing vertex with the largest likelihood is chosen as the reconstructed vertex. However, the accidental coincidence of dark noise hits after time-of-flight subtraction could produce local maxima of the likelihood at several positions which are far away from the true vertex. The search for the true global maximum is complicated and time consuming due to the large volume of the detector. To improve both the speed performance and the number of mis-reconstructions, the likelihood is then maximized from a vertex search from a list of vertex candidates calculated

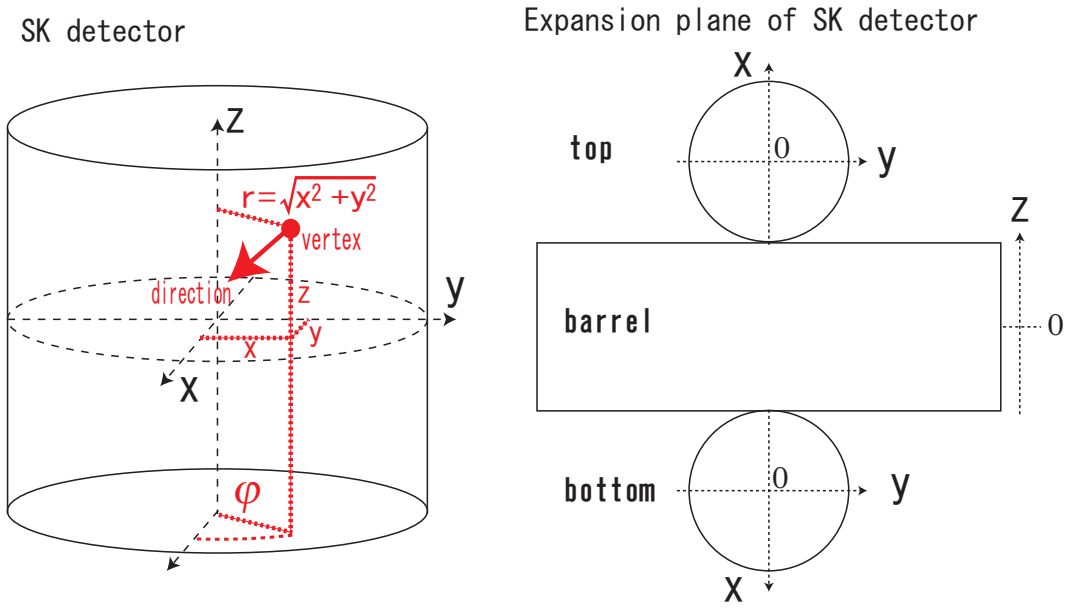

Figure 4.1: Basic variable definitions used in this thesis.

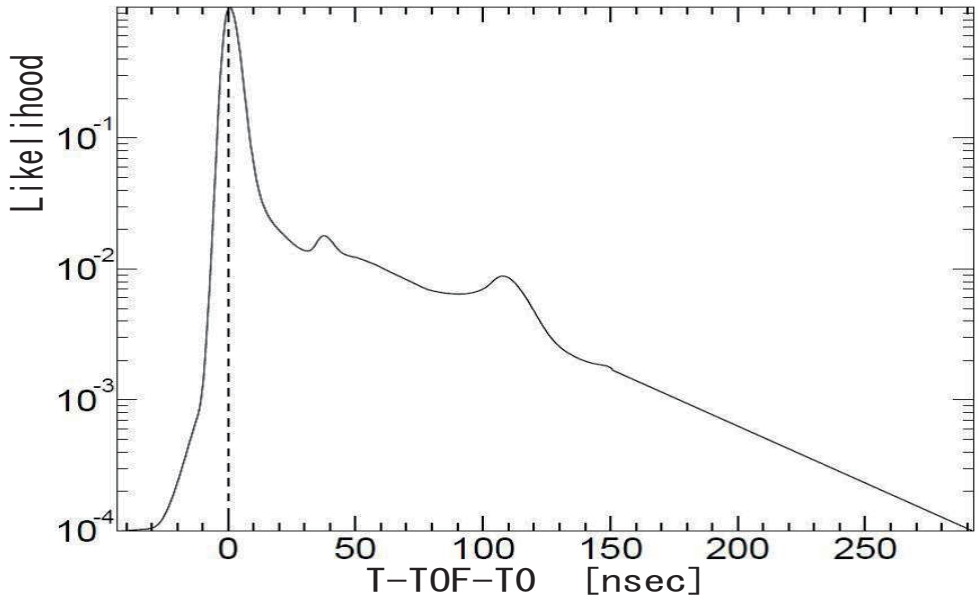

Figure 4.2: Likelihood function of BONSAI vertex fitter from LINAC calibration data. The peaks around the 40nsec and 110nsec are caused by the after pulses.

from PMT hit combinations of 4 hits each. The four-hit combinations each define a unique vertex candidate given their timing constraints. Thus, any events with four hits or more is reconstructed. The likelihood values for each vertex candidate are then calculated. To avoid a local maximum point, iterations of grid search (from 7.8m to 1cm)around each candidate are done until it finds a vertex which gives lager and more stable likelihood values at the surrounding grid points. We also use the result from the second vertex fitter which is described in [20] as a cross check and a noise reduction.

4.2 Direction reconstruction

To reconstruct the direction of a low energy event, a maximum likelihood method is used to scan directions which correspond with Cherenkov ring patterns. The definition of the likelihood is

$$L(\vec{d}) \equiv \sum_{i}^{N_{20}} \log(f_{dir}(\cos\theta_{dir,i}, E))_i \times \frac{\cos\theta_i}{a(\theta_i)} \tag{4.3}$$

where N_{20} is the number of hit PMTs within a 20 ns time window around $t - tof - t_0 = 0$. f_{dir} describes distributions of opening angles between a candidate particle direction $\vec{d}$ and the reconstructed vertex $\vec{v}$ to hit PMT position $\vec{h_i}$ $(\vec{v} - \vec{h_i})$. This function is made by Monte Carlo (MC) simulation. An example for 10 MeV electrons is shown in Figure 4.4. Since the electron multiple scattering angle depends on the electron momentum [1], the function f_{dir} is constructed as a function of not only the opening angle but also the electron energy.

The factor multiplied to f_{dir} in Equation 4.3 is to correct the effect the photon incident angle to PMT (θ_i) weighted by the PMT acceptance function $a(\theta_i)$ (see Figure 4.3 for the definition of $\theta_{dir,i}$ and θ_i). Equation 4.3 is maximized by carrying out a grid search. The size of a grid is 20° at first and 1.6° at the end. An absolute angular resolution is then defined as the maximum angular difference between 68% of the reconstructed and true directions. The angular resolution is checked by LINAC event (see Section 6.9). The difference of angular resolution between MC and data results in systematic uncertainty on the total solar neutrino flux which will be discussed in Chapter 9.

4.3 Energy reconstruction

The reconstruction of the energy of recoil electron is explained here. The energy reconstruction depends on the intensity of that light. That is, the number of Cherenkov photons is approximately proportional to the electron energy and in turn proportional to the number of generated p.e.. However, because of the poor charge resolution ($\sim$ 50% at 1p.e.) of the PMTs and the fact that electrons below 20 MeV produce roughly one photon per a hit PMT, the number of hit PMTs is used to reconstruct the energy of an event. Another reason why the

[1] The approximate multiple scattering angle θ_{msc} (radian) can be calculated as

$$\theta_{msc} = \frac{13.6MeV}{\beta cp}\sqrt{\frac{x}{X_0}} \tag{4.4}$$

where p and βc are momentum and velocity, and x/X_0 is the thickness of the scattering medium in the unit of the radiation length. In the case of 10 MeV electron in water (the radiation length is 36.1 cm), $\theta_{msc} \sim 27°$. Thus, the angular resolution for solar neutrino is limited by the multiple scattering.

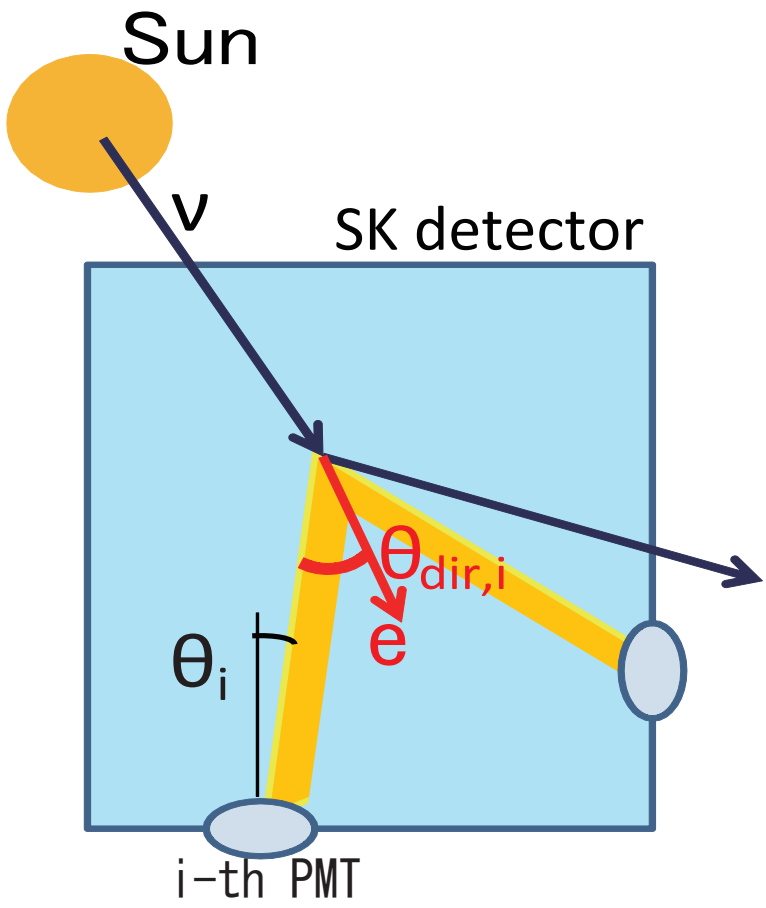

Figure 4.3: Definition of $\theta_{dir,i}$ and θ_i.

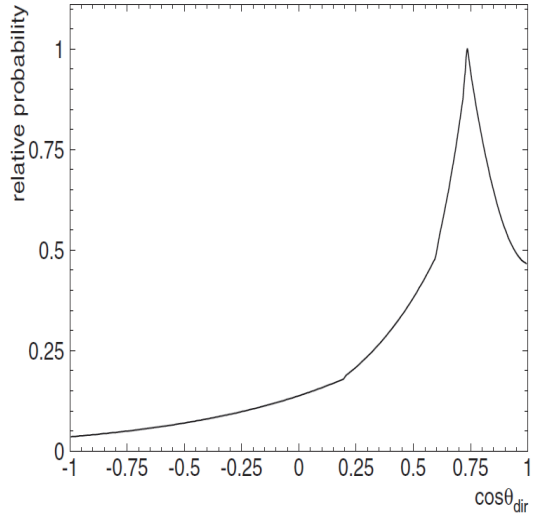

Figure 4.4: Angular likelihood of 10 MeV electron

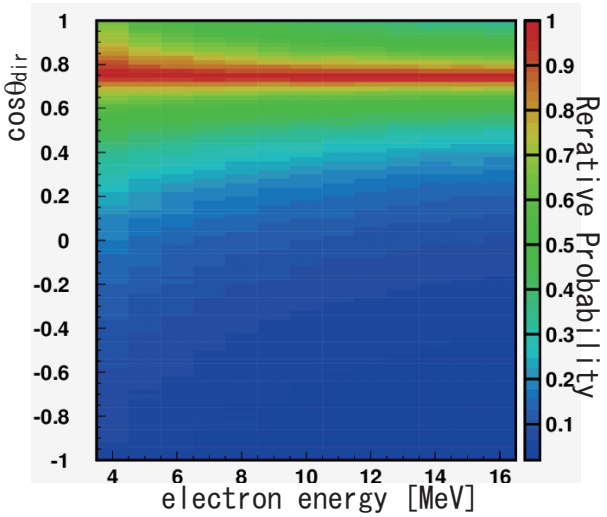

Figure 4.5: Likelihood of angular reconstruction depending on energy.

number of hits is used for energy calculation is that the number of hits does not strongly depend on the gain of PMTs compared to the total p.e.

N_{50} is defined as the maximum number of hits found by 50nsec sliding time window search of $T - Tof - T0$ distribution. Since N_{50} is affected by several factors, such as accidental hits from dark noise of PMTs, the effective number of hits (N_{eff}) is used to estimate the energy of an event. The definition of N_{eff} is following;

$$N_{eff} = \sum_{i}^{N_{50}} \left\{ (X_i + \epsilon_{tail} - \epsilon_{dark}) \times \frac{N_{all}}{N_{alive}} \times \frac{1}{S(\theta_i, \phi_i)} \times \exp(\frac{r_i}{\lambda(run)}) \times G_i(t) \right\} \tag{4.5}$$

where the explanation of each correction are following;

X_i: Multi-photo-electron hit correction

This correction is needed to estimate the effect of multiple photo-electrons in the i-th hit PMT due to the fact that if an event occurs close to a detector wall and is directed towards the same wall, the Cherenkov cone does not have much distance to expand then the observed number of hits becomes smaller. The correction X_i is defined as

$$X_i = \begin{cases} \frac{\log \frac{1}{1-x_i}}{x_i}, & x_i < 1 \\ 3.0, & x_i = 1 \end{cases} \tag{4.6}$$

where x_i is the ratio of hit PMTs in a 3×3 PMTs surrounding the i-th PMT to the total number of live PMTs in the same area. The $-\log(1-x_i)$ term is then the estimated number of photons per one PMT in that area and is determined from Poisson statistics. When $x_i = 1$, 3.0 is assigned to the value.

e_{dark}: Correction for dark noise hits

This factor is for hits due to dark noise in the PMTs.

$$\epsilon_{dark} = \frac{50nsec \times N_{alive} \times R_{dark}}{N_{50}} \tag{4.7}$$

where N_{alive} is the number of all live ID PMTs and R_{dark} is the measured dark rate for a given run.

e_{tail}: Correction for late hit

Some Cherenkov photons being scattered for reflected arrive late to the PMT, and make late hit outside the 50nsec time window. To correct the effect of the late hits, the term

$$\epsilon_{tail} = \frac{N_{100} - N_{50} - N_{alive} \times R_{dark} \times 50nsec}{N_{50}} \tag{4.8}$$

is added where N_{100} is the maximum number of hits found by 100nsec sliding time window search.

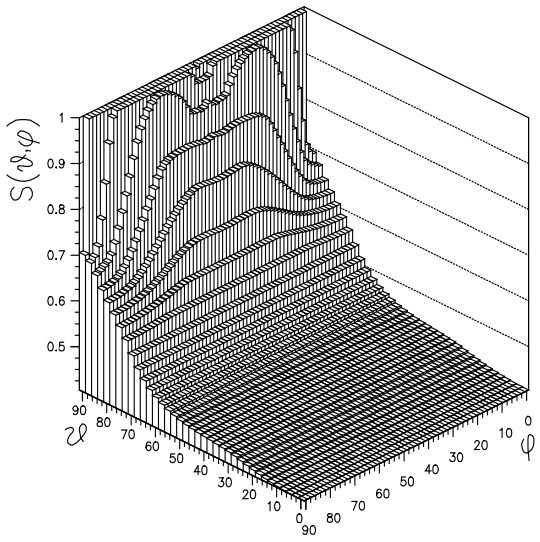

Figure 4.6: Correction factor of photocathode coverage.

$\frac{N_{all}}{N_{alive}}$: Dead PMT correction

This factor is for the time variation of the number of dead PMTs. N_{all} is total number of PMTs in SK-III and is 11129.

$\frac{1}{S(\theta_i,\phi_i)}$: Correction for photo-cathode coverage

This term is to account for the direction-dependent photcathode coverage. $S(\theta_i, \phi_i)$ is the effective photocathode area of the i-th hit PMT as viewed from the angles (θ_i, ϕ_i) which is shown in Figure 4.6. The definition of (θ_i, ϕ_i) is shown in Figure 4.7.

exp($\frac{r_i}{\lambda(run)}$):Water transparency correction

The water transparency is accounted for by this factor where r_i is the distance from the reconstructed vertex to the i-th hit PMT. $\lambda(run)$ is the measured water transparency for a given run.

$G_i(t)$: PMT gain correction

This factor is to adjust the relative gain of the PMTs at the single photo-electron level. The differences in gain depend on the fabrication date of the PMTs.

After determining N_{eff}, an event's energy in terms of MeV can be calculated as a function of N_{eff}. The relation between N_{eff} and MeV is obtained by uniform electron MC events , and the systematic uncertainty of the reconstructed energy is checked by LINAC and DT calibration (see Section 6.7.2)

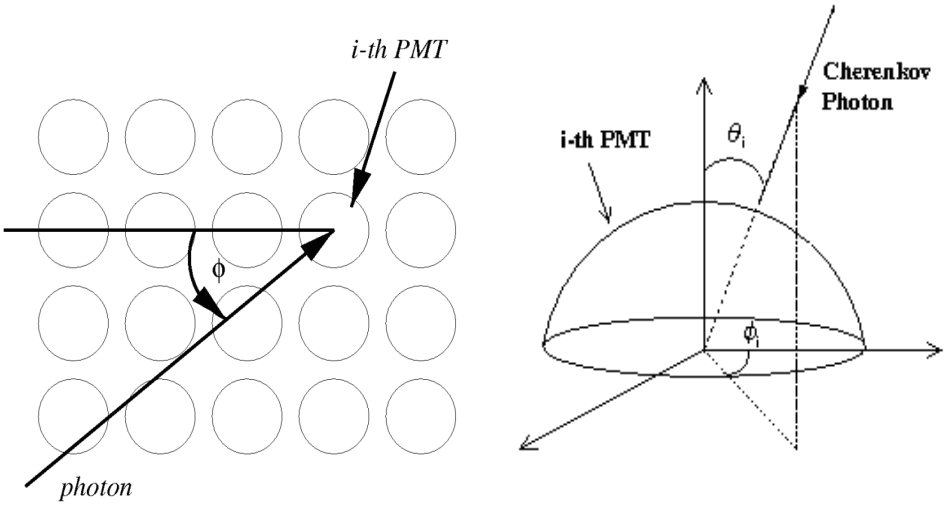

Figure 4.7: Definition of (θ_i, ϕ_i).

Chapter 5

Simulation

5.1 Outline of detector simulation

The detector response can be understood by Monte Carlo(MC) simulation of the detector. In solar neutrino event simulation, the tracking of the recoil electron and the emission of Cherenkov photons are done in the first step. In the second step, the Cherenkov photons are propagated. Finally, the response of the detector is simulated. Most of the physics processes such as multiple scattering or bremsstrahlung are simulated by GEANT3.21 [37], except for the production and the propagation of Cherenkov photons and the light attenuation in water, which are developed by SK group [38].

Cherenkov photon production

The number of Cherenkov photons dN emitted by an electron per wavelength interval $d\lambda$ per track length dx is given by

$$dN = 2\pi\alpha\left(1 - \frac{1}{n^2\beta^2}\right)\frac{1}{\lambda^2}dxd\lambda \tag{5.1}$$

where n is the refractive index of water ($n = 1.334$), α is the fine structure constant, and β is the velocity of the electron in unit of the light velocity in vacuum. The opening angle θ of Cherenkov photons is given by

$$\cos\theta = \frac{1}{n\beta} \tag{5.2}$$

Based on these formulae, Cherenkov photons are produced in the simulation.

Propagation of photons in water

The velocity of Cherenkov photons depends on its wavelength. The velocity is given as a group velocity (v_g) of the wave packet:

$$v_g = \frac{c}{n(\lambda) - \lambda\frac{dn(\lambda)}{d\lambda}} \tag{5.3}$$

where $n(\lambda)$ is the refractive index of water as a function of the wavelength such as

$$n(\lambda) = \sqrt{\frac{a_1}{\lambda^2 - \lambda_a^2} + a_2 + a_3\lambda^2 + a_4\lambda^3 + a_5\lambda^6}. \tag{5.4}$$

The unit of λ is μm, and parameters are

$$\begin{aligned} \lambda_a^2 &= 0.018085, & a_1 &= 5.7473534 \times 10^{-3} \\ a_2 &= 1.769238, & a_3 &= -2.797222 \times 10^{-2} \\ a_4 &= 8.715348 \times 10^{-3}, & a_5 &= -1.413942 \times 10^{-3} \end{aligned}$$

These are obtained by measurements.

There are three processes which are considered during the photon propagation: Rayleigh scattering, Mie scattering, and absorption. The attenuation length ($L_{attn.}$) of light in water is then given by

$$L_{attn.} = \frac{1}{\alpha_{abs}(\lambda) + \alpha_{Rayleigh}(\lambda) + \alpha_{Mie}(\lambda)} \tag{5.5}$$

where $\alpha_{abs}(\lambda), \alpha_{Rayleigh}(\lambda), \alpha_{Mie}(\lambda)$ are coefficients for the absorption, Rayleigh scattering, and Mie scattering as a function of the wavelength of photons (λ). The fraction of these processes depends on the wavelength and the purity of water. The wavelength dependence of each process is given by

$$\alpha_{abs}(\lambda) = \begin{cases} \frac{A_1}{\lambda^4}, & \lambda \leq 350\text{nm} \\ \frac{A_1}{\lambda^4} + A_2(\lambda/A_3)^{A_4}, & 350 < \lambda \leq 415\text{nm} \\ \frac{A_1}{\lambda^4} + f(\lambda), & 415\text{nm} < \lambda \end{cases} \tag{5.6}$$

$$\alpha_{Rayleigh}(\lambda) = \frac{R_1}{\lambda^4} \times (1 + \frac{R_2}{\lambda^2}) \tag{5.7}$$

$$\alpha_{Mie}(\lambda) = \frac{M_1}{\lambda^4} \tag{5.8}$$

where A_x, R_x, M_x are tuning parameters, and $f(\lambda)$ is measured by [39]. The measurement is done by a periodical laser injection calibration. When a photon arrives at the detector wall (the acrylic cover, the PMT surface or the black sheet), the reflection, absorption and transmission are considered. An example of the fraction of these processes at the PMT surface is shown in Figure 5.1.

Detector response

When a photon reaches at the PMT surface, the detector response is simulated. The probability to produce one p.e. from the photon arriving at each PMT surface has four components:

$$Probability = QE(\lambda) \times \frac{AorP(\lambda, \theta_i)}{AorP(\lambda, 0)} \times COREPMT \times qetable(i) \tag{5.9}$$

where $QE(\lambda)$ is the quantum efficiency of 20-inch PMT depending on the wavelength of the incident photon λ, which is measured by HAMAMATSU, $AorP(\lambda, \theta)$ is summed fraction of the absorption and p.e production (black + green in figure 5.1), and is measured by a calibration with injected laser light. Thus, $\frac{AorP(\lambda,\theta_i)}{AorP(\lambda,0)}$ is a correction depending on the incident angle θ_i for the photon with λ. $COREPMT$ corrects the average quantum efficiency (Q.E.) which is common to all PMTs and tuned by LINAC (see Section 6.6.2). Finally, $qetable(i)$ is the relative Q.E. for the i-th PMT measured by Ni calibration (see Section 6.1). After one p.e. is produced with the probability, the output charge from PMT is simulated according to the measured 1

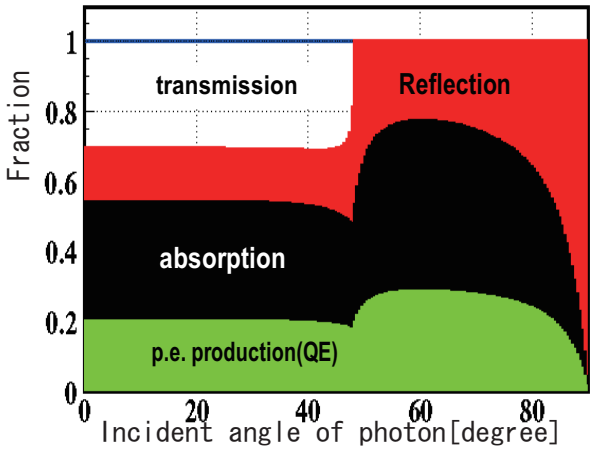

Figure 5.1: Fraction of reflection, absorption, or transmission at PMT surface (the wavelength of the incident photon is $\lambda = 420$nm)

p.e. charge distribution. If the output charge exceeds the ATM threshold within the ADC gate, the hit information is stored. The hit timing is simulated according to the timing distribution obtained by LINAC. Finally, one event is generated by adding random dark hits.

5.2 New modeling of water condition

It was found that the PMT hit-rate measured by Ni calibration at top region are systematically lower than that of bottom region by $3 \sim 5\%$ (called top-bottom asymmetry (TBA)). Figure 5.2 shows the time variation of top-bottom asymmetry measured by Ni calibraion and Xe calibration (see Section 6.1). However, MC simulation cannot reproduce the top-bottom asymmetry with the uniform attenuation length in space. To solve this problem, a simple model of the light absorption is introduced to take into account the position dependence of the attenuation length in Equation 5.5. In this modeling, only z-dependence of the absorption parameter is considered. The reason is that by the laser injection calibration, the dominant contribution to the time variation of the water transparency is measured to be the absorption. Figure 5.3 shows the absorption parameter measured by laser light injectors at different z positions in February 2008. As suggested by the measured z-dependence, the z-dependence can be modeled as

$$\alpha_{abs}(\lambda, z) = \begin{cases} \alpha_{abs}(\lambda)(1 + \beta \cdot z), & \text{for } z \geq -1200\text{cm} \\ \alpha_{abs}(\lambda)(1 - \beta \cdot 1200), & \text{for } z < -1200\text{cm} \end{cases} \tag{5.10}$$

where the absorption factor is assumed to be uniform below z=-1200cm due to the convection of water. This β is called Top-Bottom Asymmetry parameter (TBA parameter), and is tuned so that the top-bottom asymmetry becomes smallest. The tuning result is shown in section 6.4

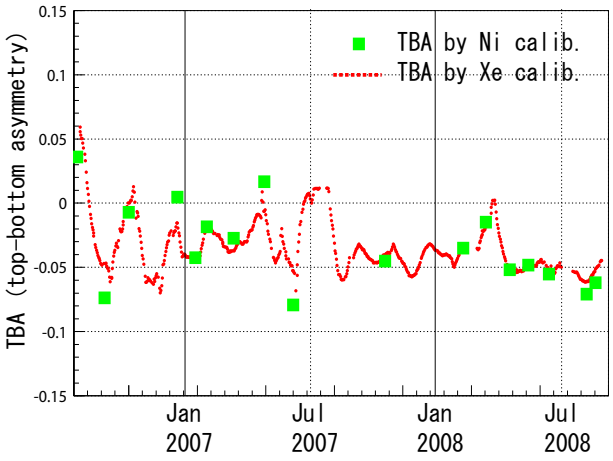

Figure 5.2: Time variation of TBA measured by Ni and Xe calibration The vertical axis show the top-bottom asymmetry (TBA) value which is defined as (Hirate(top)-Hitrate(bottom))/Hitrate(barrel) for Ni calibration, and (Charge(top)-Charge(bottom))/Charge(barrel) for Xe calibration.

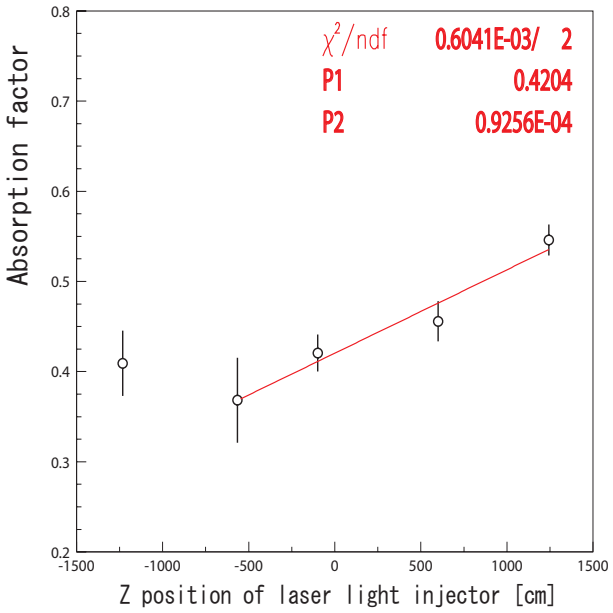

Figure 5.3: Z dependence of the absorption factor α_{abs} measured by laser light injector. The data was taken in February 2008. The Ni calibration for the tuning of TBA parameter was carried out in February 2008. The line shows the result of linear fitting of the four points. This slope is consistent with the tuned TBA parameter value (see Section 6.4)

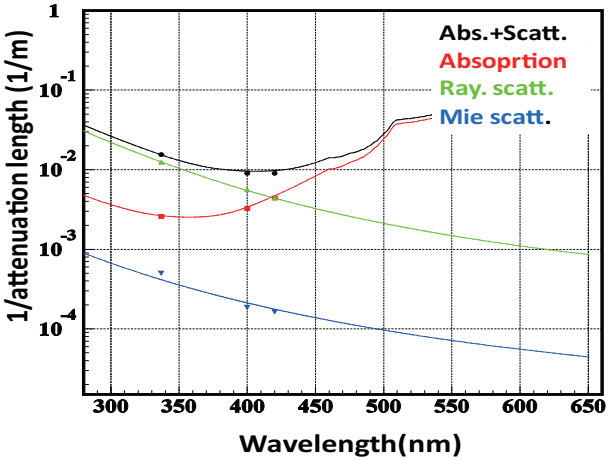

Figure 5.4: Tuned water parameters measured by laser injection calibration Makers show the measured parameters and lines show the fitted functions.

5.3 Tunable input parameters

The tunable parameters for MC simulation are listed here. The tuning results are shown in Chapter 6.

Water parameters

The absorption and scattering parameters are measured by laser light injected from top, barrel, and bottom. Figure 5.4 shows the measured water attenuation length and the contribution of the absorption, Rayleigh scattering, and Mie scattering as a function of photon wavelength for SK-III.

TBA parameter

TBA parameter is tuned so that the hit-rate of MC simulation reproduces that of calibration data taken by Ni calibration. The time variation of TBA parameter is also implemented by periodical measurements of the top-bottom asymmetry factor.

Timing resolution of PMT

Timing resolution of PMT is calibrated by LINAC. The hit timing is smeared by the measured timing resolution in MC simulation.

After pulse

PMT hit timing has some characteristic peaks after the main peak (called after pulse). A possible explanation of the cause of the after pulse is that if a photo-electron is back scattered at the first dynode, it takes some time until it loses its velocity against the electric field then comes back to the first dynode, producing a delayed hit. The fraction of the after pulse is measured by LINAC calibration. (see Section 6.6.2)

Average quantum efficiency (Q.E.) of PMT

While the relative Q.E. of each PMT is measured by the Ni calibration, the average Q.E. is tuned so that the N_{eff} of MC simulation reproduces LINAC data.

Chapter 6

Calibration

6.1 Outline of detector calibrations

An outline of the detector calibration will be given in this section. Some important calibrations for the solar neutrino measurement such as timing of PMT, water transparency, quantum efficiency(Q.E.) of PMT, and LINAC are explained in the subsequent sections. Especially, the improvement to the timing calibration is newly achieved in this thesis. The detail explanation of the detector calibration is in [31].

First, High Voltage (HV) value which is applied to each PMT is adjusted in order to achieve the same Q.E.× gain value for all PMTs becomes same within ±1% accuracy. This HV determination was done by light emission of Xe lamp guided through optical fiber (hereafter Xe calibration). A scintillator ball at the end of the optical fiber absorbs the UV light and emits light isotropically with a peak at 440nm wavelength.

After the HV determination, the conversion factor of ADC charge to p.e. is measured for each PMT. The conversion factor is given by (average PMT gain)×(relative PMT gain). The average PMT gain is obtained from an average 1 p.e. distribution of PMTs measured by Cf-Ni γ-ray source (peak energy ∼9MeV, average number of hits is 50PMTs, hereafter Ni calibration). The obtained value of average gain is 2.243 pC/p.e.. The relative PMT gain for each PMT is obtained by calibration data using high and low intensity laser light (398nm). The laser light was put into the detector through optical fiber and diffuser ball. The relative PMT gain (G_i: i denotes PMT ID) is the ratio of the mean charge (Q_i) in the high intensity data to the number of hits (Hit_i) at the low intensity data for each PMT; $G_i = Q_i/Hit_i$. This is because the Q_i is proportional to Q.E. × gain, and the Hit_i is proportional to only Q.E., thus, only the gain factor can be extracted by taking the ratio of Q_i to Hit_i.

The charge of each PMT hit is corrected by taking into account the ADC non-linearity. This non-linearity is measured by obtaining deviation of measured p.e value from the expected p.e. value. The data for this calibration is taken by laser light source.

In parallel to these calibration related to the charge of each hit, timing calibration, water transparency measurement, and Q.E. measurement were done. Then LINAC and DT (deuterium and tritium neutron generator) calibration were done especially for the low-energy event analysis. In the following sections, the explanation about these calibrations which are closely related to the solar neutrino analysis will be given.

6.2 Timing calibration

The timing of all PMTs must be calibrated so that the event vertices and directions are reconstructed accurately. To obtain correct timing, the followings must be considered; the light intensity of each PMT, the length of cable between each PMT and electronics, and different range of hit timings. Different light intensity makes different triggered timing which is so called "time walk". The time walk exists because larger charge hits exceed TDC discriminator threshold earlier than those with less charge even though the hit PMT gets photons in the same timing. The timing calibration for SK-III consists of two measurements; one is to make a correction table for the time walk and cable length, and the other one is to make a correction function for hit timings in different time ranges. It should be mentioned that the former one is a main part of timing calibration which is basically same as the one in the previous phase of experiments, but the latter one is newly introduced in SK-III to decrease the systematic shift of the reconstructed vertex position.

Conventional timing calibration

This calibration is to correct the time walk of each PMT and the overall process time for each PMT (cable length and electronics. etc.). The time walk and the overall process time can be measured by putting a fast pulsing light source in the center of the detector. Figure 6.1 shows a schematic view of the timing calibration system. First, a N_2 laser pulse is divided in the

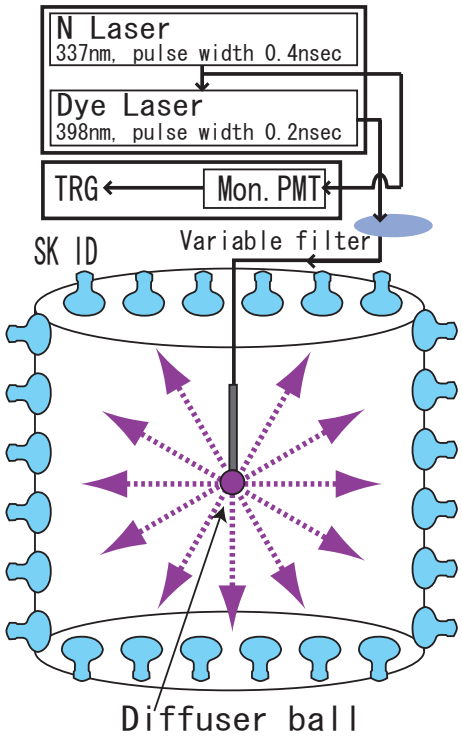

Figure 6.1: Schematic view of timing calibration system

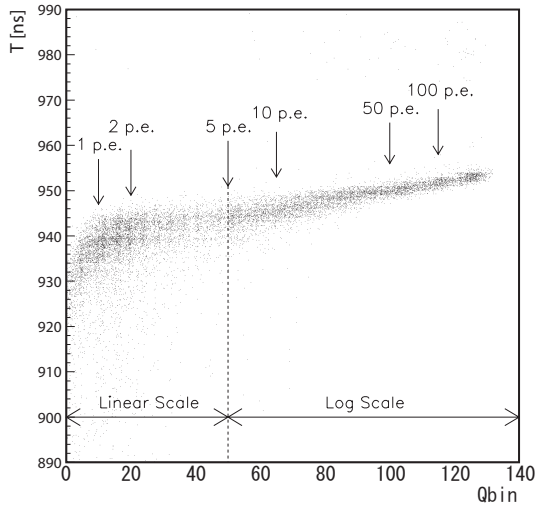

Figure 6.2: Example of TQ distribution. Horizontal axis shows charge of each hit, and Vertical axis shows hit timing without correction.

laser module. One goes to a trigger PMT which makes an external trigger for timing calibration

event. The other goes to dye laser module to produce a dye laser pulse. The dye laser pulse (wavelength; 398±5nm(FWHM), pulse width 0.2nsec) then goes through variable filter which is used to adjust the laser intensity. After traveling 70m optical fiber, the dye laser pulse is emitted in the detector from a diffuser ball.

The calibration data are taken by changing the intensity of the light from the diffuser ball. Using the variable filter, the light intensity can be adjusted from 0.0 p.e. level to high intensity level (250p.e.) which causes saturation of electronics. Figure 6.2 shows a typical relation between timing and charge. The vertical axis shows the hit timing without correction, and the larger value corresponds to earlier hit timing. This two dimensional histogram is called "TQ distribution". The purpose of this calibration is to fit the TQ distribution by a proper function. This function is called "TQmap".

The TQmap is made for each channel (11129 PMTs × 2 ATM buffer channels). The method to generate TQmap is following. In the first step, after making the timing distribution plot for each channel, selection of laser hit is done by setting 100 nsec time-window around the peak of the timing distribution with TOF(time of flight from the diffuser ball to each PMT) "added". The "+" sign for TOF means that before the timing correction the vertical axis corresponds to time interval between the hit and the global trigger (see the DAQ section 3.3). Since the smaller value of vertical axis shows the later hit, TOF must be added to get the time when a pulse light is emitted from the diffuser ball.

A selection is needed to remove pre-pulses which occur at around 50nsec before the main peak by a photon hitting the dynode of PMT, and after-pulses which occur at about 100 nsec after the main peak by an electron back scattered at the first dynode. After the selection of laser hits, for each of the 140 bins in charge (Q_{bin}), the peak timing and the standard deviation of timing distribution is obtained by asymmetric Gaussian fitting which takes into account the effect of the scattered or reflected hits. The bin width of each charge bin is defined as

$$\Delta Q_{bin} \equiv \begin{cases} 0.2 \text{ pC}, & \text{for } 1 \leq Q_{bin} \leq 50 \ (0 \text{ pC} \leq Q \leq 10 \text{ pC}) \\ 10^{\frac{Q_{bin}}{50}} - 10^{\frac{Q_{bin}-1}{50}}, & \text{for } 51 \leq Q_{bin} \leq 140 \ (10 \text{ pC} \leq Q \leq 630.95 \text{ pC}) \end{cases} \tag{6.1}$$

Finally, the peak timings with respect to the charge is fitted by a seventh order polynomial function.

An improvement of SK-III method is following. In SK-I and II, instead of the peak value, the timing of each charge bin was determined from an average timing. The timing obtained by the previous method, therefore, was affected by late scattered or reflected hits especially at small charge regions. [1] Since the amount of reflected hits are large in the edge of ID, such effect gives systematic timing shift depending on PMT positions. Figure 6.3 shows one example of the difference between the two methods. As shown in Figure 6.3, the hit timing of the new method is faster than that of the old method at small charge region, which means that the new method is less affected by the late hits.

[1] In the previous method, to reduce the effect of timing of late hits, First, an average is obtained from the selected hits within 100nsec for each Qbin. Then, for each Qbin, a narrow timing window is set +2.0RMS-1.5RMS around the average timing within the 100 nsec time-window. Finally, the timing of each Qbin is determined from the average timing in the narrow time window.

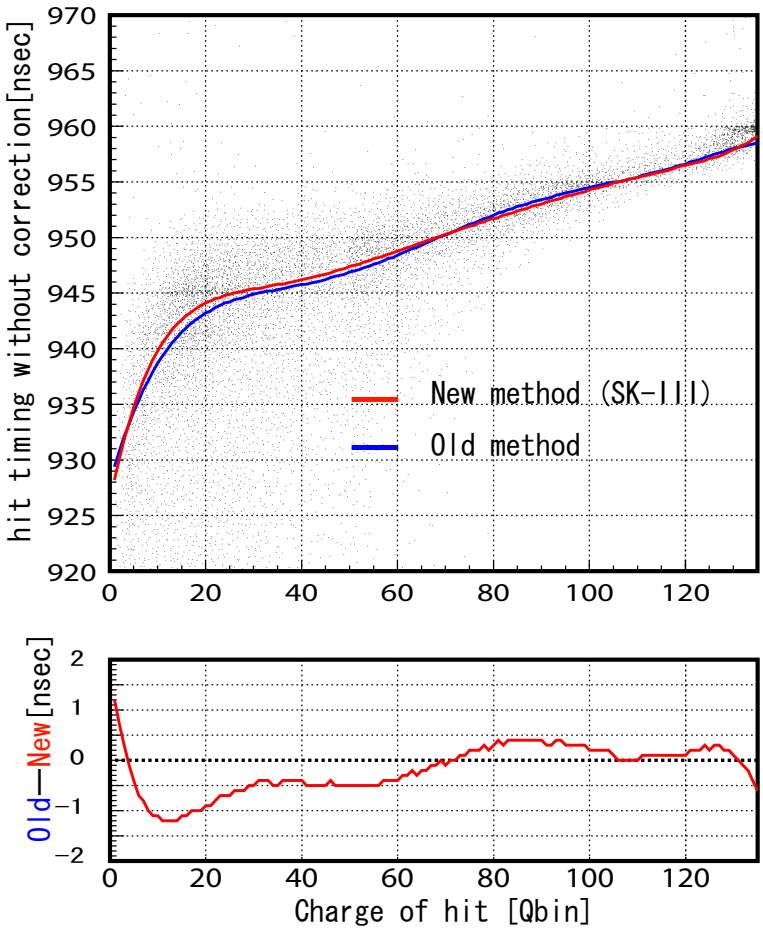

Figure 6.3: Example of comparison between the old and new methods of TQmap.

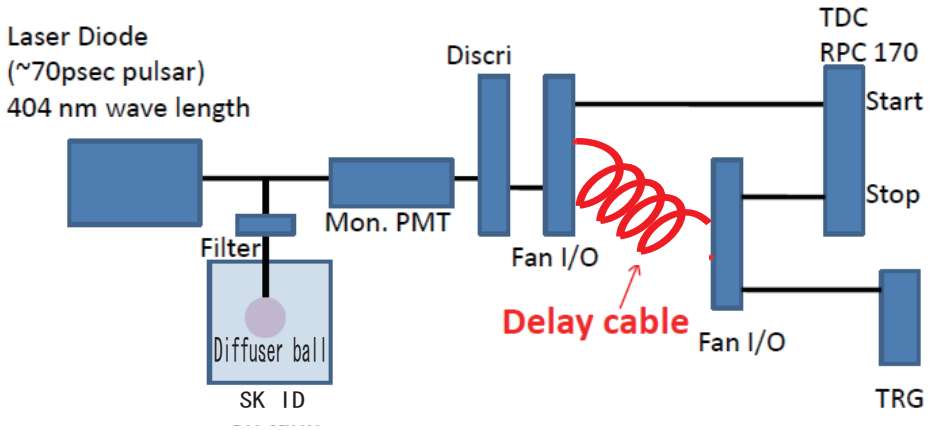

Figure 6.4: Setup for additional timing calibration

Additional timing calibration

The other calibration which has been carried out is to improve the performance of reconstruction. It was observed that the reconstructed position of Ni calibration events was shifted inward direction from the real source position to the tank center (see Figure 6.7-(a)).

This direction of the vertex shift indicates that the linearity of relative timing within a wide range (∼100nsec) is not perfect due to characteristics of electronics. For source positions away from center and near the ID wall, the spread of hit times is larger (∼100nsec) if the TOF is not subtracted. In this case, the earlier hits seem to be shifted later by ∼0.5nsec. This timing difference between far side hits and near side hits can create the bias to reconstructed position.

I have measured this timing shift by the following setup. Figure 6.4 shows a schematic diagram of trigger system of this calibration. In order to measure the timing shift between late hit and early hit, a calibration trigger signal (common stop signal) from the monitor PMT is artificially delayed by putting additional cables (from 15m to 80m), and the time delay is measured by a independent system which is pre-calibrated within 0.1% accuracy. For example, a 20m cable can make the arrival time of the global trigger at each ATM by 50nsec later, which corresponds to make hit timing of each PMT 50nsec faster. By changing the cable length 15m up to 80m, we can check the relation of the timing measured by ATM and the timing measured by the independent system within the range of about 300 nsec.

Figure 6.5 shows an example of the result for a PMT. The horizontal axis shows hit time measured by ATM, and vertical axis is delayed time measured by independent system. While the horizontal axis and vertical axis show good linearity within ±1nsec as shown in the top plot of Figure 6.5, the difference has a clear dependence on the value of hit time. This tendency is common to all channels which is shown in Figure 6.6. The average of fitted slope values is -0.67nsec/100nsec, thus correction function is

$$T = T - slope \times (T - 1000.0) + offset(ch) \tag{6.2}$$

where T is hit time, 1000.0nsec is selected as normalization point, and $offset(ch)$ is an offset value depending on ATM ch (0a ∼ 11b). After applying this correction, the vertex shift is

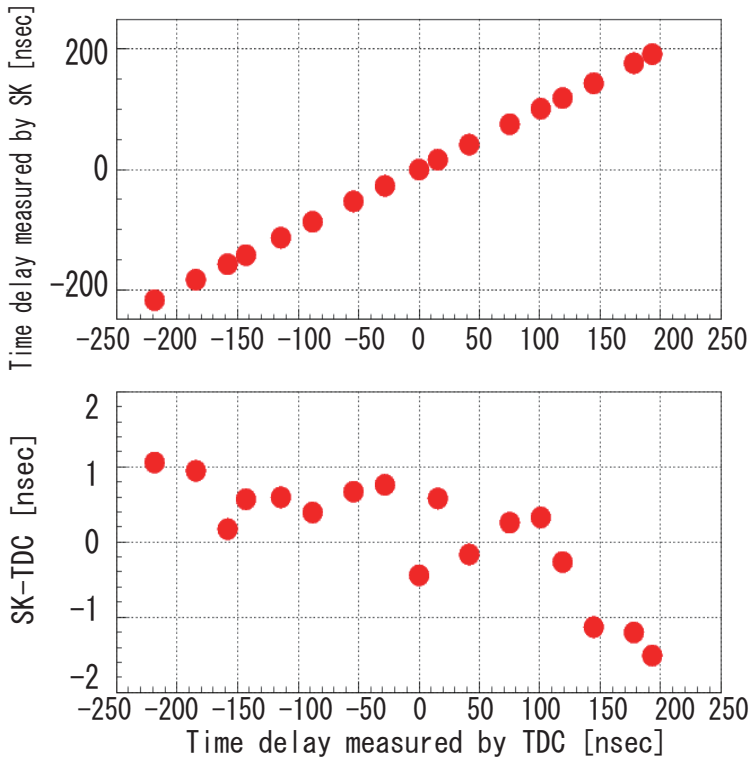

Figure 6.5: Example of timing shift as a function of hit timing range for one channel

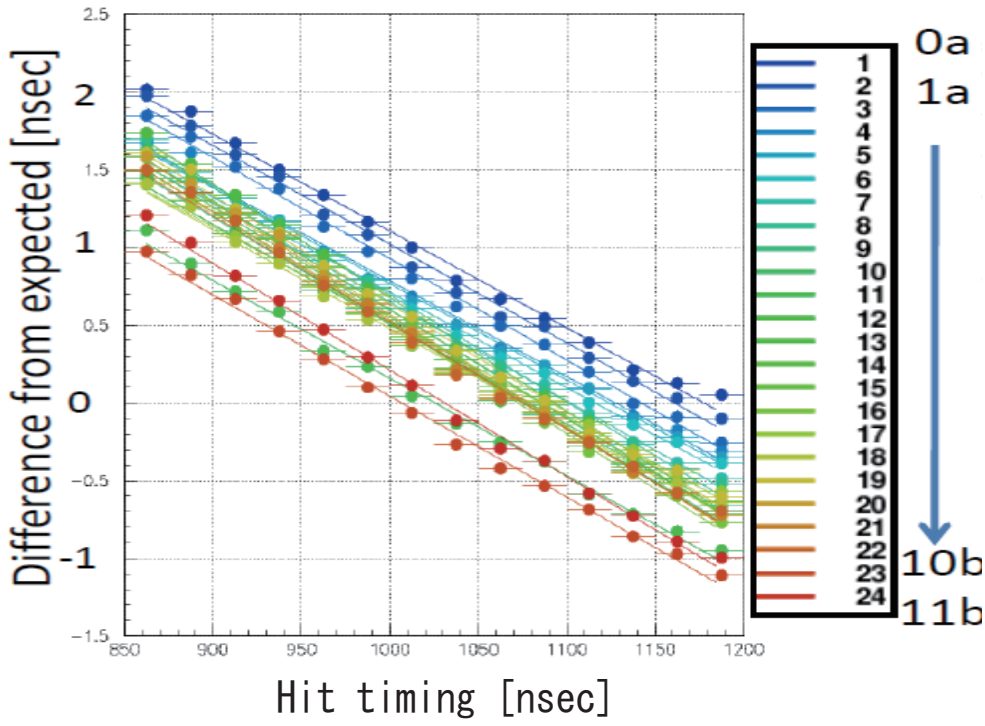

Figure 6.6: timing shift as a function of absolute hit timing. Different colors show timing shift of the different ATM channels (0a to 11b). The marker show mean timing shift of the same ATM channel PMTs with respect to the absolute hit timing. The lines show the results of linear fitting for all ATM channels.

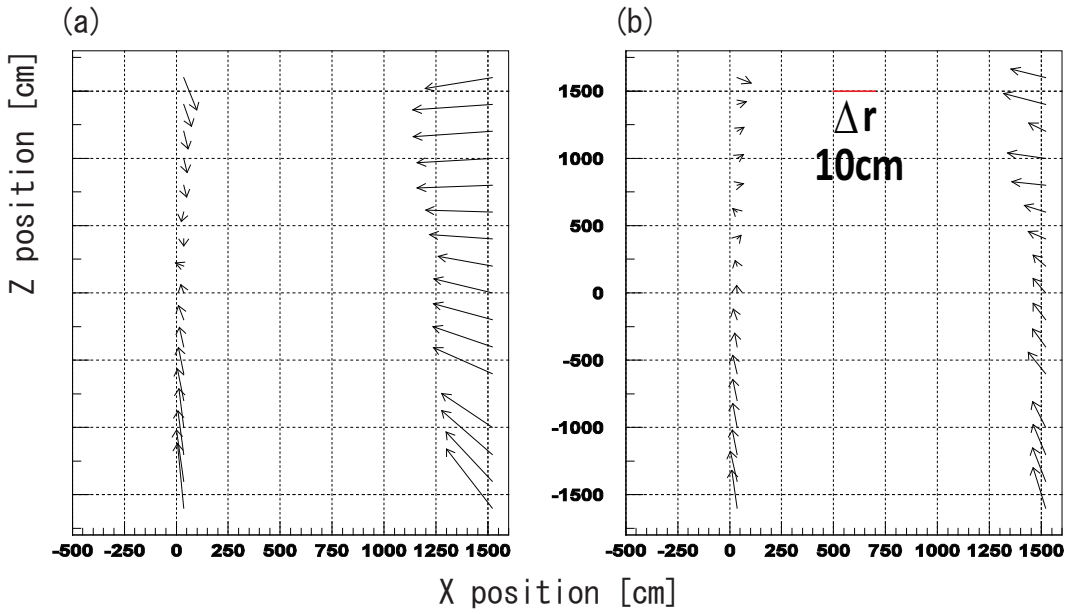

Figure 6.7: Vertex shift of Ni calibration events before(a) and after(b) correction. The origin of arrows shows the true Ni source position and the direction indicates the averaged reconstructed position. The length of arrow shows the length of vertex shift. The red line is the scale of 10cm vertex shift.

reduced as shown in Figure 6.7-(b). The remaining vertex shift gives a systematic uncertainty of fiducial volume which is estimated as 0.54%. The corresponding value in SK-I was 1.3%. So, more than factor 2 improvement is achieved in this analysis.

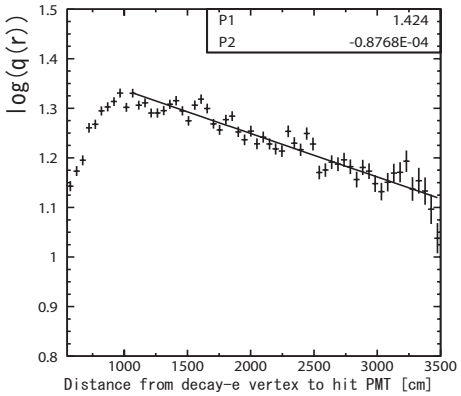

Figure 6.8: Charge vs. distance from the decay-e vertex. Vertical is log of hit charge (p.e.) and line shows the result of linear fitting.

6.3 Water Transparency Measurement

The water transparency is measured by using decay electrons and positrons (hereafter decay-e) from cosmic-ray muons stopped in the detector (hereafter stopping μ). The selection criteria of decay-e are following:

- The time difference between the stopping μ and the decay-e candidate (ΔT) must be $2.0\mu\text{sec} < \Delta T < 8.0\mu\text{sec}$.
- The reconstructed vertex of the decay-e candidate must be within the 22.5-kton fiducial volume (=2m from ID wall).
- The number of hit PMTs within 1.3μsec, $N_{hit} \geq 50$

About 1500 decay-e events are selected with this criteria every day, which is statistically enough for this weekly transparency measurement.

Figure 6.8 shows the correlation between log of the charge ($q(r)$) of hit PMTs (vertical) and the distance from the decay-e vertex to each hit PMT (horizontal). The charge of PMT is corrected considering the acceptance depending on the incident angle of photon. To eliminate scattered hits or reflected hits, hit PMTs are selected by the following criteria:

- Hit PMT must be one of N_{50}.
- The opening angle of a hit PMT θ_{dir} must be $32^\circ < \theta_{dir} < 52^\circ$

After fitting the histogram with linear function, the water transparency is obtained by the inverse of the fitted slope.

Figure 6.9 shows the time variation of the water transparency. Each point represent a water transparency for 6 days.

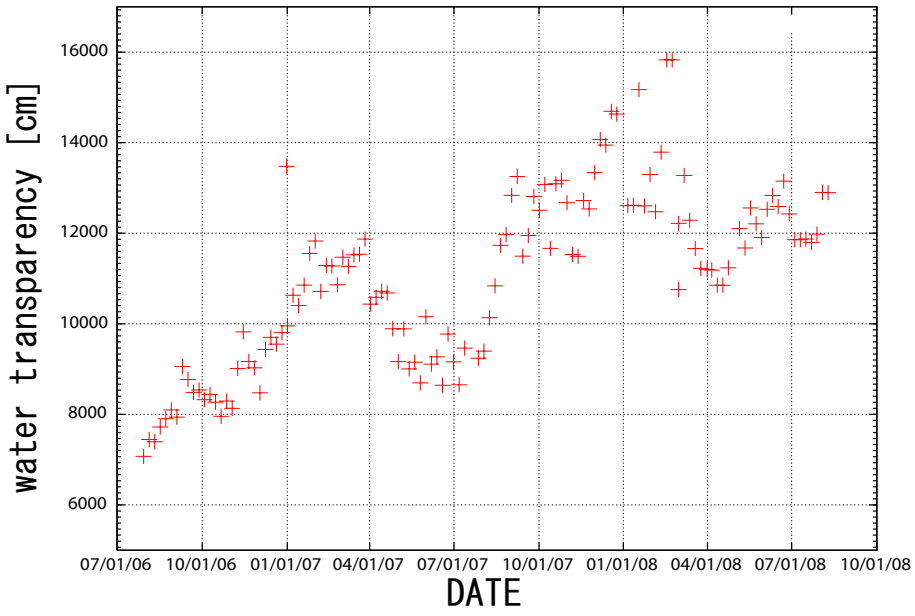

Figure 6.9: Time variation of water transparency. Each point is determined from 6day data period.

6.4 TBA tuning and Q.E. measurement by Ni calibration

As already described in the previous chapter, the TAB parameter is newly introduced to SK-III detector simulation to model the z-dependence of the absorption parameter. This parameter is tuned so that the PMT hit-rate of data and MC simulation shows the best agreement. With the tuned TBA parameter, the relative Q.E. of individual PMT is obtained by taking the ratio of the hit-rate of data to that of MC simulation. The usage of Ni-Cf γ-ray source is favored because of following reasons

- Easy to operate and good isotropy.
- Low occupancy ($\frac{Nhit}{\text{Total \# of PMTs}} \sim 1\%$) is needed to avoid multi-photon hit.
- Q.E. should be measured at the Cherenkov wavelength range.

Figure 6.10 shows a comparison of the hit-rate between data and MC simulation with TBA=0 and TBA=tuned value respectively. Hit-rate is defined as number of hits in each PMT in a unit of the averaged number of hits for all PMT during the calibration run[2]. As shown by the figure, data and MC shows better agreement with TBA=tuned value (8.85×10^{-5}). Then, the relative Q.E. to be put into MC is obtained as the ratio of data to MC.

[2]The acceptance correction as a function of incident angle of photon to each PMT and the distance correction between the source position and each PMT position are taken into account to obtain the number of hits for each PMT.

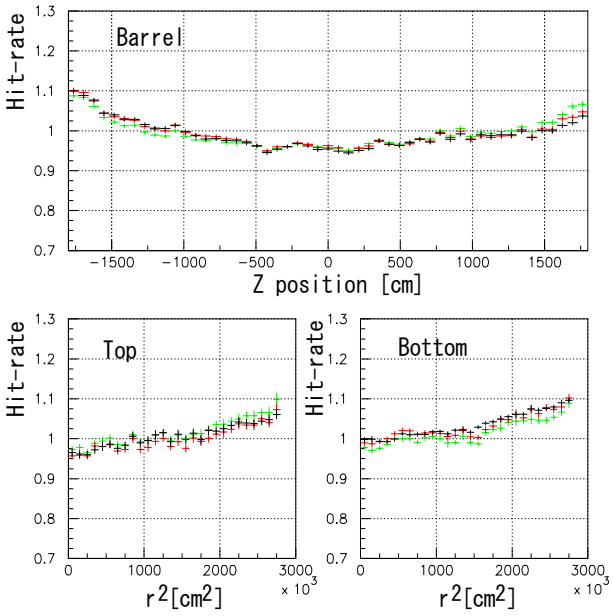

Figure 6.10: Hit rate of data(Black) and MC simulation (Green: TBA=0,Red: TBA=tuned)

6.5 DT calibration

6.5.1 DT neutron generator

Deuterium-Tritium Generator [40] produce neutrons by colliding deuterium and tritium ions with a fixed metal hydride target with a reaction;

$$^{3}\mathrm{H} + ^{2}\mathrm{H} \longrightarrow ^{4}\mathrm{He} + n \tag{6.3}$$

The deuterium and tritium are ionized by Penning ion source. The energy of neutrons is 14.2MeV which is high enough to make ^{16}N by the (n,p) reaction on ^{16}O [41] in water. The ^{16}N then decays with a half-life of 7.13 second with gamma-ray and/or electrons. The dominant decay mode (66%)produces a 6.1MeV γ with an electron of 4.3MeV endpoint energy, while the second dominant decay mode (28%) produce a 10.41MeV electron. The advantage of this calibration is following; First, as shown in the Figure 6.11, this calibration is easier to operate compared to LINAC. Second, the data can be taken in many places. Third, the event direction is isotropic. Taking advantage of DT neutron generator, the data are uesd to study the uncertainty of energy scale depending on position and direction (see Section 6.7.2).

6.5.2 Trigger efficiency

In addition to data taking with the normal LE and SLE trigger threshold, special calibration data was taken with the threshold value at -150mV. With the special data, the trigger efficiency is defined as follow ;

$$Eff_{LE,j} = \frac{N_{LE,j}}{N_{special,j}} \tag{6.4}$$

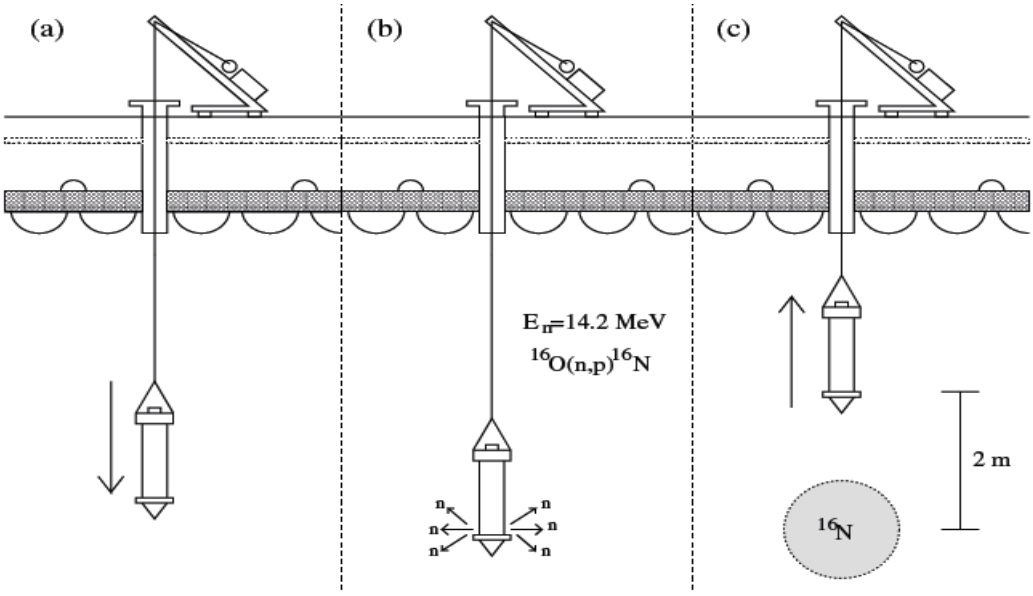

Figure 6.11: Schematic view of DT neutron generator calibration setup. (a) The generator is inserted in the tank, (b) Neutrons are created, (c) The generator is lifted 2 meters, so that we can make the shadow effect of the the generator as small as possible.

$$Eff_{SLE,j} = \frac{N_{SLE,j}}{N_{special,j}} \tag{6.5}$$

where $N_{LE(SLE),j}$ is the number of events in j-th energy bin triggered by LE (SLE) threshold, and $N_{special,j}$ is that of the special threshold. Figure 6.12 shows the trigger efficiency measured by DT calibration compared with trigger simulation of MC. The difference between data and MC is 2.0% in 4.5-5MeV, 1.0% in 5-5.5MeV, 0.5% in 5.5-6MeV, and 0.1% in 6-6.5MeV (SLE2 period). The trigger efficiency in higher energy region is 100%, thus the difference is negligible.

6.6 LINAC Calibration

6.6.1 the LINAC system

An introduction of the LINAC system will be given. The detail information can be found in [42]. Figure 6.13 and 6.14 show the schematic view of the LINAC system and structure of the end cap. The LINAC is a model ML-15MIII from Mitsubishi. During the operation, the beam pipe is evacuated to less than 0.1Pa, and the beam size and momentum is tuned by collimator and magnets. The energy range of the electron is selected from 4.4-18MeV, so that we can make a similar event as the recoil electron event. Other specifications are summarized in Table 6.1 Due to the small systematic uncertainty of the system [42], we can use the LINAC data not only for the absolute energy scale calibration but also for various systematic uncertainty studies.

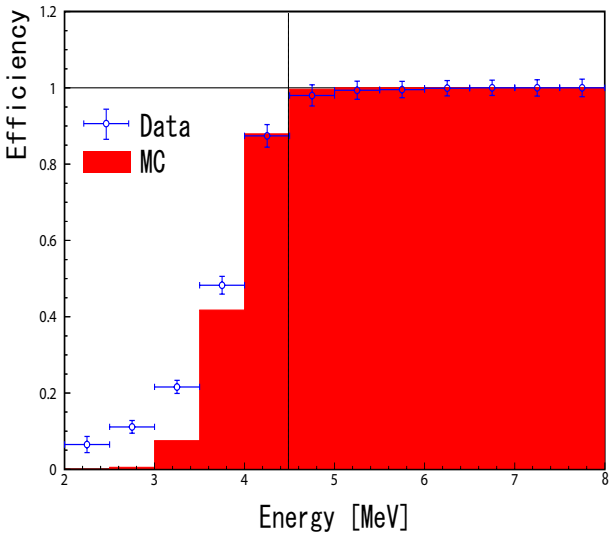

Figure 6.12: An example of SLE trigger efficiency obtained by DT data and MC

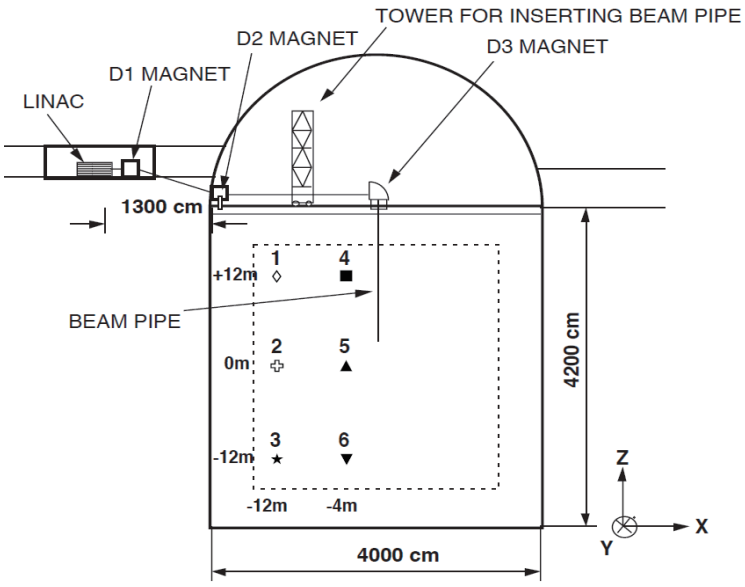

Figure 6.13: The LINAC system

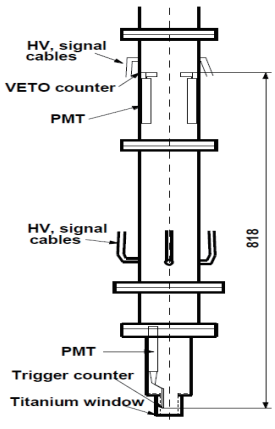

Figure 6.14: The structure of end cap

Energy range	4.4 - 18 MeV
Intensity	$\sim$ 0.1 electron/bunch
	adjusted by the intensity of electron gun
Number of bunches	up to $\sim$ 90 bunches/sec
Beam energy spread	$< \pm 0.3\%$
Beam size	$1 \sim 2$cm at end cap
Vacuum	$\sim 10^{-4}$ Pa in accelerator tube
	<0.1 Pa in beam pipe

Table 6.1: LINAC specification

Beam energy calibration

The beam energy is measured by a Ge detector. The crystal size of the Ge detector is 57.5mm in diameter and 66.4mm in length. The energy resolution is 1.92keV for 1.33 MeV γ from ^{60}Co. At the end of data taking for each position and each beam momentum, the Ge detector is placed just behind of D3 magnet whose current set to 0A. There is the same titanium window at the position. The energy evaluation by Ge is done by comparison with Ge detector MC simulation considering the energy losses in the Ti window, the Be window of the Ge detector, and inactive region of the Ge detector. The total energy in SK detector is obtained from the measured beam momentum. The energy loss of the trigger counter and the Ti window is taken into account in that calculation. The uncertainty of the beam energy is evaluated as $\pm$20keV at 9.52MeV (0.21%).

Data set

LINAC data was taken in March 2008. Beam energies taken in that time are 5.1, 8.8, 13.6, 18.9 MeV. The beam positions are shown in Figure 6.13.

6.6.2 Tuning parameter results

Average Q.E.

The average Q.E. (COREPMT) is obtained by the following steps. For this study, 8.8MeV mode is used.

1. Make MC of all positions with different COREPMTs
2. Get peak value of N_{eff}
3. Compare the peak values with that of DATA.
4. Find COREPMT which gives minimum position dependence.

As the result, obtained value of COREPMT is 0.888. Figure 6.15 shows the tuning result. Figure 6.16 shows the energy scale difference between data and MC simulation. The position averaged difference between LINAC data and MC is within 0.5% for all energies.

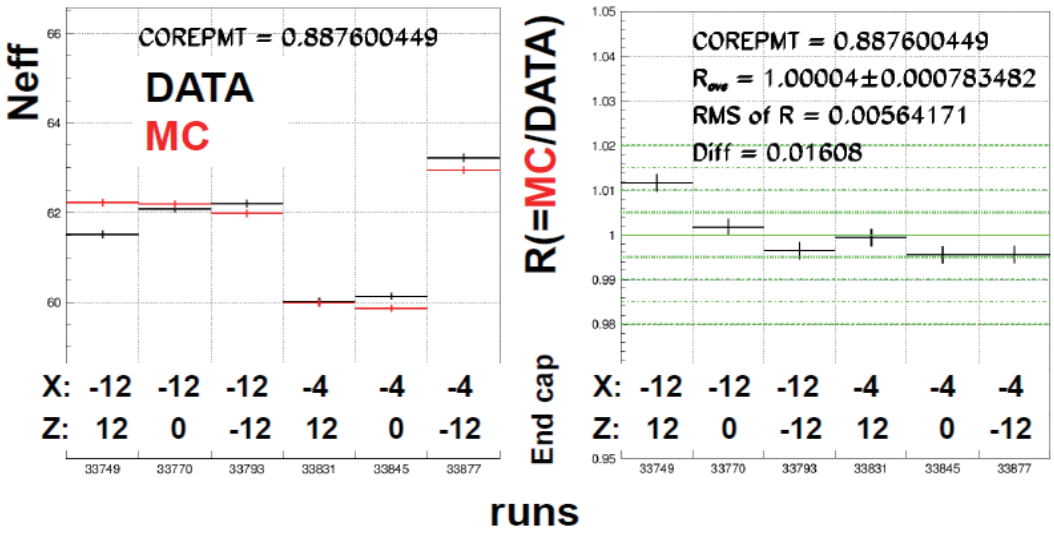

Figure 6.15: Tuning result of COREPMT Diff in the right plot shows the difference between the maximum and minimum of R(=MC/DATA).

After pulse

If a photo-electron is back scattered at the first diode, it takes some time until it loses its velocity against the electric field then comes back to the first dynode. In such case, the hit timing delays a certain amount and makes an after pulse. The fraction and the delay time are tuned by LINAC hit timing distribution. Tuning result shows that the characteristic components of the after pulses are at 111.5 nsec (1.4%) and 39.0 nsec (1.3%) after the main pulse (see Figure 4.2).

Timing resolution

Timing resolution determines the vertex resolution, and thus it affects the vertex resolution directly. Therefore, the tuning of timing resolution is important in terms of reducing systematic uncertainty of MC. In this analysis, I have performed a very precise tuning of the timing resolution.

After these tuning done, the timing distribution of LINAC data and MC agree very well as shown in Figure 6.17.

6.7 Energy scale

6.7.1 N_{eff} to Energy

After the all detector simulation tuning, the conversion function from N_{eff} to energy is obtained by uniformly generated electron MC events. This energy is electron total energy. The

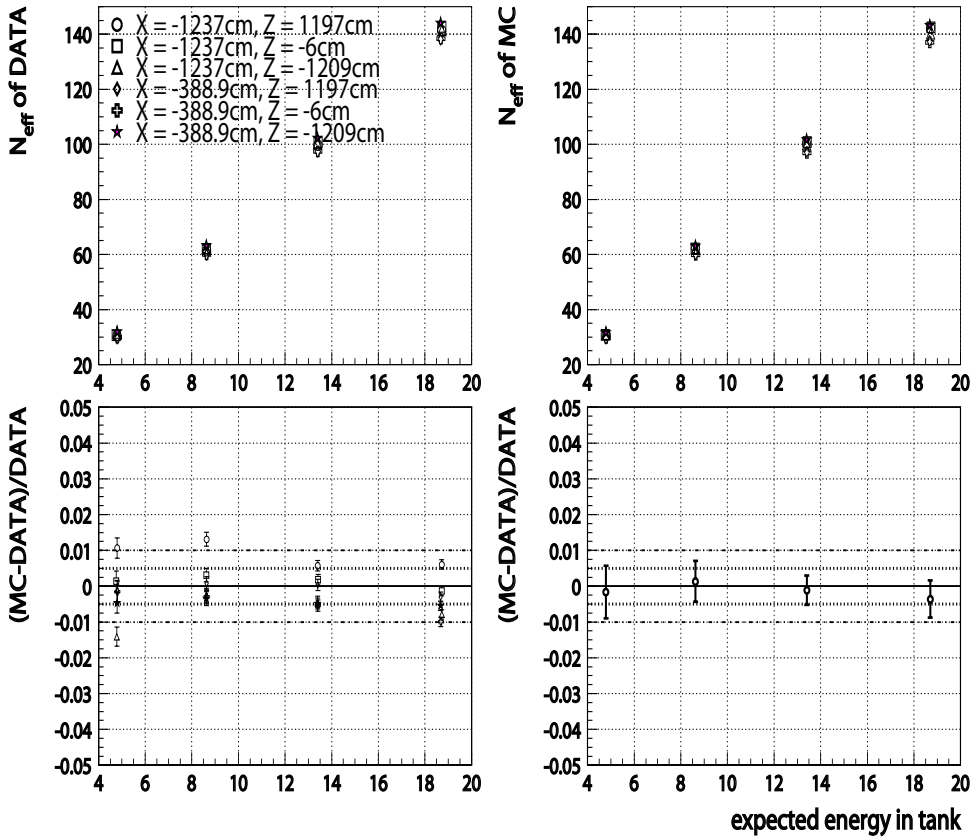

Figure 6.16: Energy scale difference of LINAC data and MC simulation . The left bottom plot shows the difference of each position (makers correspond to the position of Figure 6.13) The right bottom plot shows the position averaged difference.

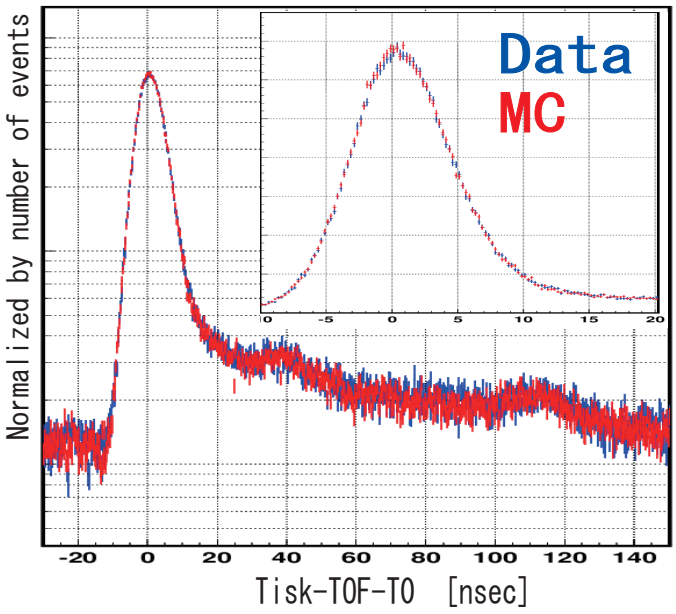

Figure 6.17: Timing distribution after tuning MC. LINAC 5.1MeV (x,z)=(-12m,12m)

relation between the energy and N_{eff} is given

$$E = p_1 + (p_2 + (p_3 + (p_4 + p_5 N_{eff})N_{eff})N_{eff})N_{eff} \tag{6.6}$$

where p_i $(i = 1..5)$ are fitting parameter. Figure 6.18 shows the fitting result. The obtained parameters are

$$\begin{aligned} p_1 &= 0.82221 \\ p_2 &= 0.12897 \\ p_3 &= -9.49202 \times 10^{-5} \\ p_4 &= 1.09289 \times 10^{-6} \\ p_5 &= -2.91088 \times 10^{-9} \end{aligned}$$

6.7.2 Energy scale uncertainty

Position dependence of Energy scale

To estimate the position dependence of energy scale, the z-dependence and phi-dependence should be taken into account. The z-dependence is measured by LINAC, and the ϕ-dependence is measured by DT because the large y position is not included in the calibration positions for LINAC.

Figure 6.19 shows the difference of energy scale between LINAC data and LINAC MC depending on the LINAC position. By averaging over all positions, the z-dependence is estimated as 0.06% (difference between r=4m and r=12m is also included here.)

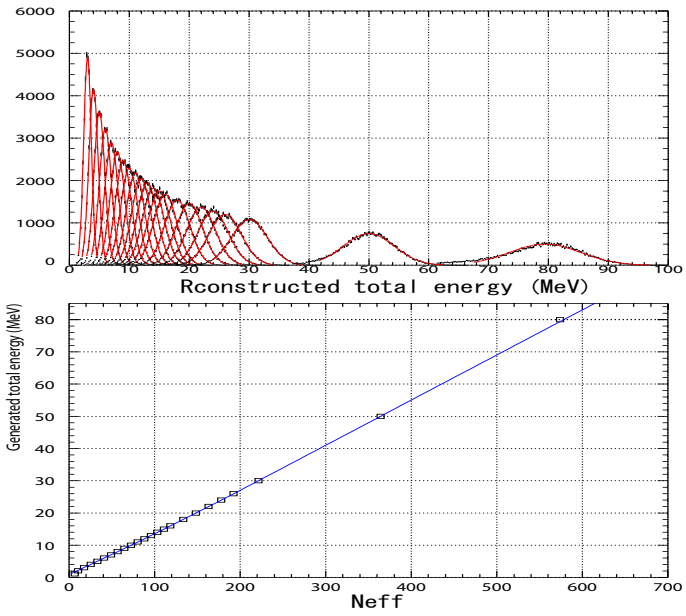

Figure 6.18: Energy distribution of electron MC simulation (upper), and N_{eff} to energy function (lower) In lower plot, the maker shows the relation of the mean of N_{eff} and generated electron total energy, and the line shows the fitted polynominal function.

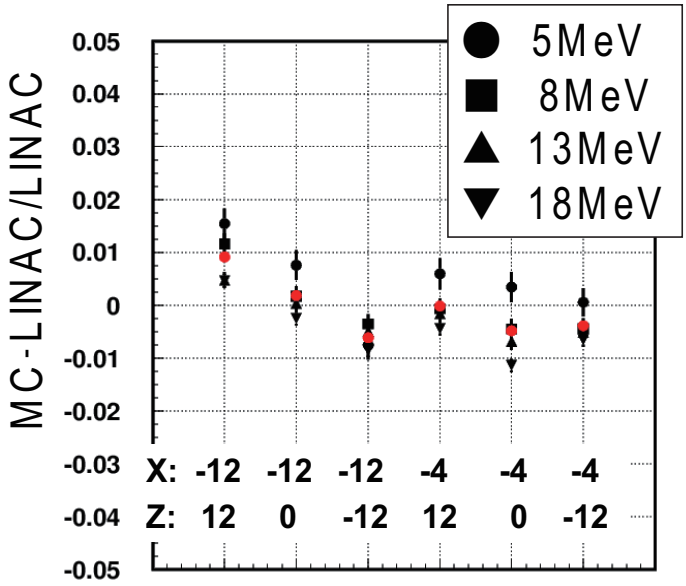

Figure 6.19: Difference of N_{eff} mean between LINAC Data and MC simulation. Black markers show each energy, and red markers show energy averaged values.

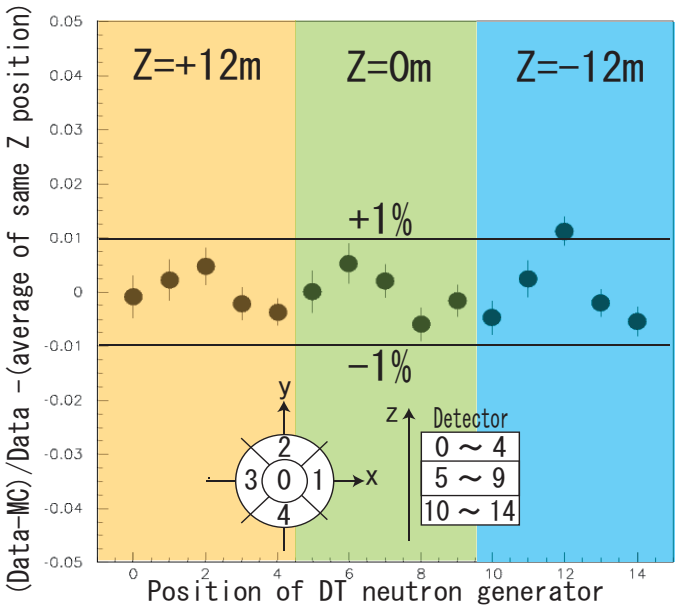

Figure 6.20: Difference of N_{eff} mean between DT Data and MC simulation. The definition of horizontal axis is shown in the figure.

Figure 6.20 shows the difference of energy scale between DT data and DT MC the horizontal axis is normalized by the average of same z positions. The mean value of deviation from the average is taken as a phi-dependence of energy scale which is 0.35%.

Angular dependence of energy scale

The directional uniformity of the energy scale can be obtained by DT calibration. Since the LINAC beam is only downward-going, the directional uncertainty of energy scale should be checked and added to the total energy scale uncertainty. This is also important when studying the energy spectrum distortion and the day/night effect caused by the MSW effect.

Figure 6.21 shows energy scale difference between DT data and DT MC depending on the event direction. The difference between LINAC direction (the left most bin of the Figure 6.21) and the average of other bins is 0.02%. Conservatively, the size of error is taken as the angular dependence of energy scale which is 0.25%.

Effect of Water transparency accuracy to energy scale

The uncertainty of the energy scale is also depending on the uncertainties of water transparency measurement when the LINAC calibration data was taken. The uncertainty of the water transparency measurement is evaluated by fitting error distribution. Figure 6.22 shows a distribution of statistical uncertainty of water transparency of every 6day period which is obtained from the fitting error of the transparency slope. The average value of uncertainty for 6day measurement is taken as the uncertainty of water transparency during LINAC run period. The average value 159cm is correspond to 0.2% of energy scale which is obtained from MC generated with artificially increased water transparency.

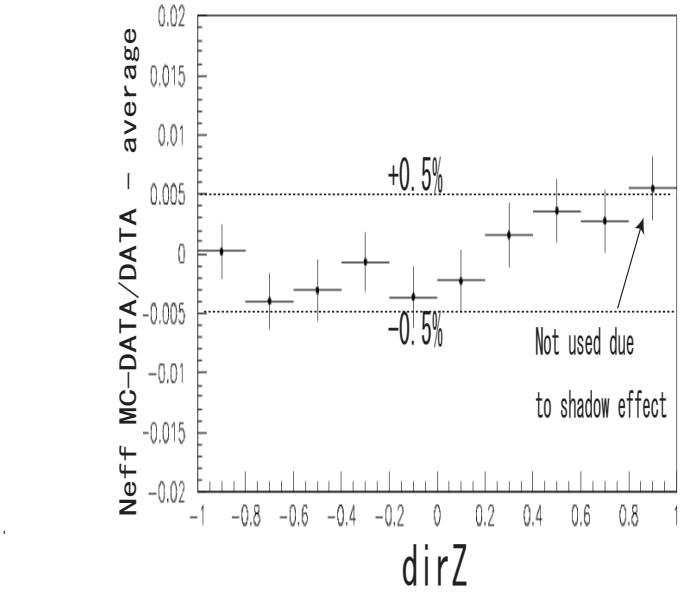

Figure 6.21: Difference of N_{eff} mean between DT Data and MC simulation depending on direction.

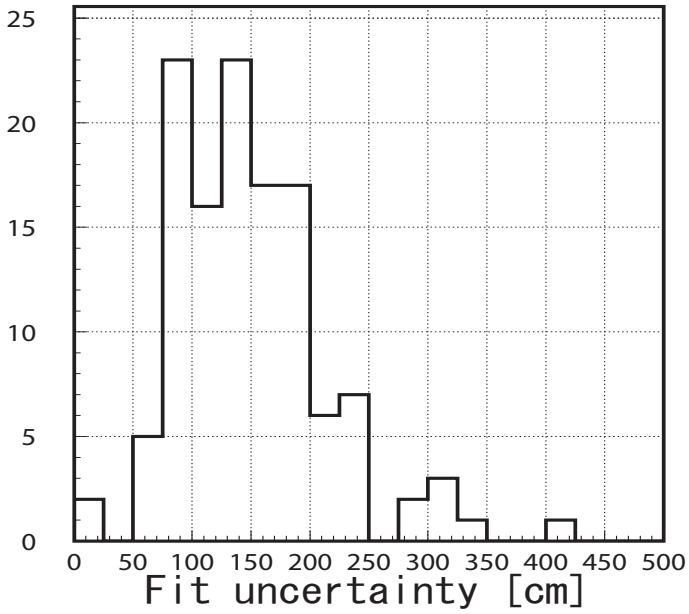

Figure 6.22: Fit uncertainty of water transparency measurement.

Position dep.	0.35 %
Direction dep.	0.25 %
WT. uncertainty	0.20 %
LINAC energy sys.	0.21 %
Total	0.53 %

Table 6.2: Systematic uncertainty of energy scale

Electron beam energy determination

Uncertainty of electron beam energy determination of LINAC system is estimated as 0.21 % [42].

Total energy scale systematic uncertainty

Adding all the contributions in quadrature, the total uncertainty of SK-III energy scale is estimated as 0.53% (see Table 6.2). The corresponding value for SK-I is 0.64%. About 20% of improvement can be seen in SK-III.

6.8 Energy resolution

Energy resolution function is obtained from MC which is same as the one the energy function is made from. Figure 6.23 shows the energy resolution as a function of the reconstructed energy. The fitted energy resolution function is:

$$\sigma(E) = \frac{1}{E}(-0.123 + 0.376\sqrt{E} + 0.0349E) \tag{6.7}$$

where E is the energy of an event (MeV). The difference of the energy resolution between data and MC is checked by LINAC, and it is shown in Figure 6.24. The observed shift seemed on direction, but I took the difference between data and MC is $\pm 2.5\%$.

6.9 Angular resolution

An absolute angular resolution is defined as an angle which include 68% of the reconstructed directions around the beam direction. The angular resolution as a function of electron energy is shown in Figure 6.25. The difference between data and MC is 0.7% at maximum.

This angular resolution shows about 10% improvement in 5MeV region if it is compared to that in SK-I [20].

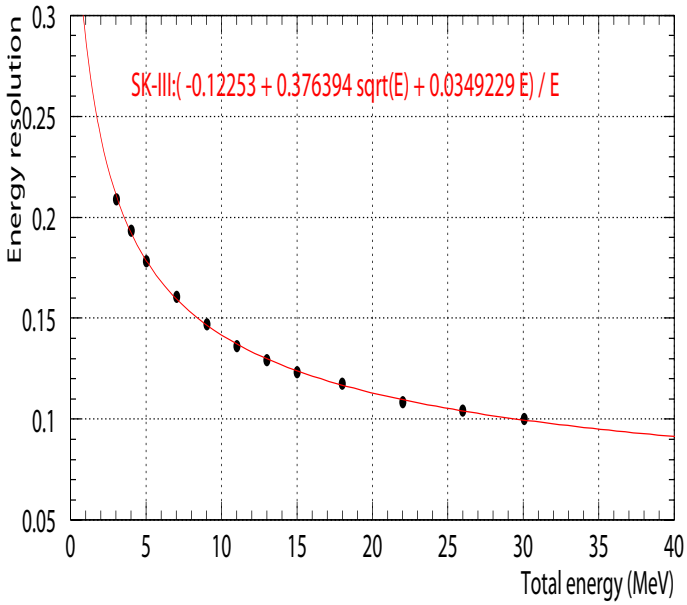

Figure 6.23: Energy resolution function obtained by electron MC simulation . Black points show the one standard deviation of Gaussian fit of MC simulation (see top plot of Figure6.18), while the line shows the fitting by the polynominal function.

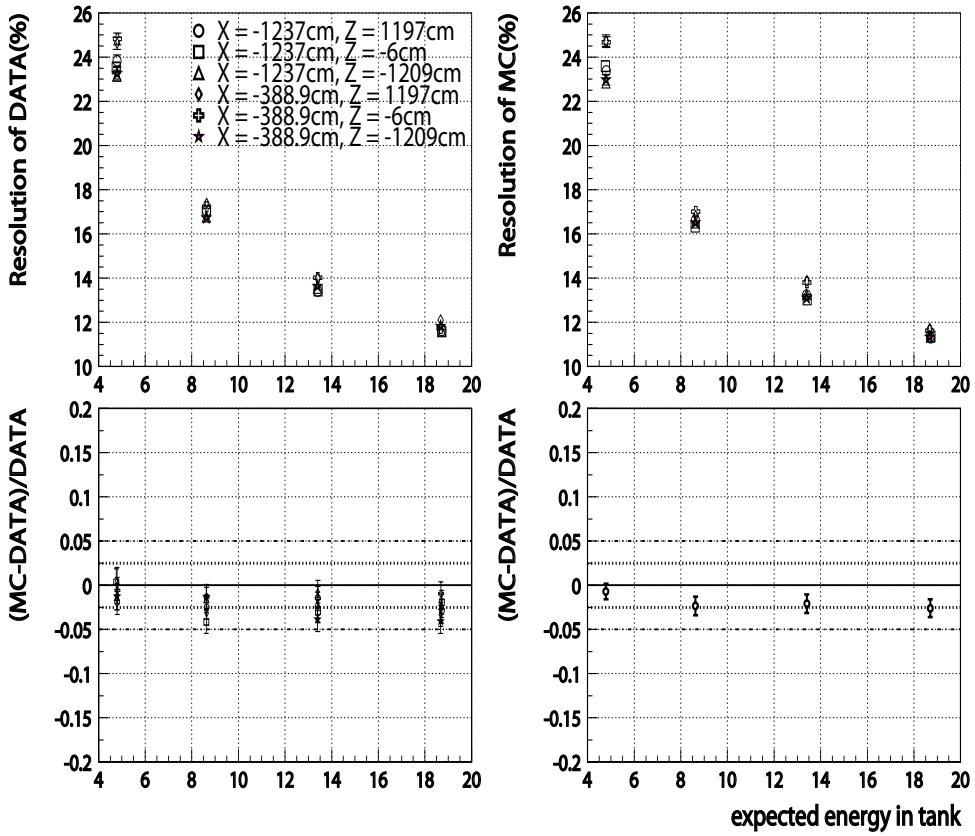

Figure 6.24: Energy resolution of LINAC data and MC simulation The left bottom plot shows the difference of each position (makers correspond to the position of Figure 6.13) The right bottom plot shows the position averaged difference.

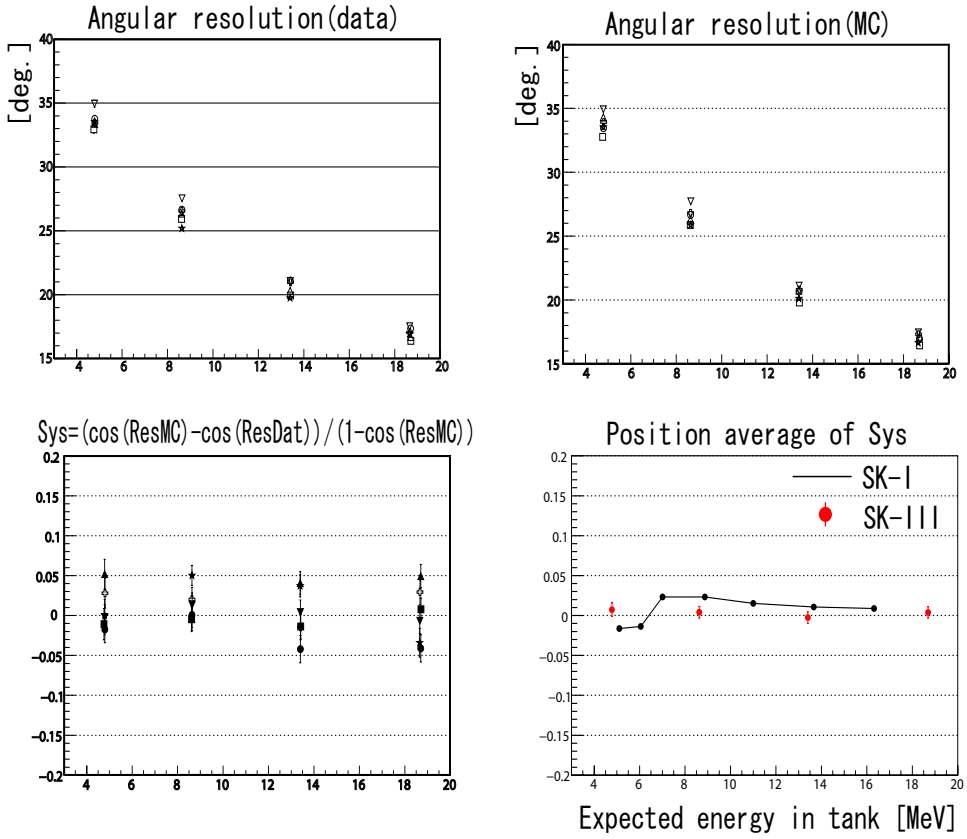

Figure 6.25: Angular resolution of LINAC data and MC simulation

Chapter 7

Data Analysis

The data for SK-III solar neutrino analysis were taken from August 5, 2006 to August 17, 2008. SK-III has three periods with different hardware threshold settings. The explanation of each period is summarized in Table 7.1

7.1 Monitoring of Radon level

A major background for the lower energy region (total energy is less than 6.5 MeV) is radioactive impurities such as radon which are mixed in the pure water. To achieve the low energy threshold at 4.5 MeV, it is needed to reject such high radon concentration periods that happened after water system maintenance or detector calibration, etc.. In order to do this, the radioactivity at different positions of the detector has been monitored by checking low energy event rate. Figure 7.1 shows how the low-energy event rate changes at the different detector positions. The high event rate periods coincide with the water system maintenance and detector calibration. These high rate are caused by remaining radon in water. After removing the high radioactivity periods, the sample for low-energy threshold analysis is obtained. The corresponding livetime is 298.2 days. Since the radon event only affect the low energy region the periods are not removed for sample with 6.5 MeV threshold whose livetime is 547.9 days.

7.2 Run definition

A basic unit of dataset is a run. Each run is at most 24 hours long, and divided into subruns which have usually 1 to 5 minutes long depending on the trigger rate.

Date (From Y/M/D to Y/M/D)	Hardware thr. (mV)	100% eff. above: (MeV)	livetime (days)
2006/08/05 - 2007/01/24	-302	6.5	121.7
2007/01/24 - 2008/04/17	-212	5.0	331.5
2008/04/17 - 2008/08/18	-186	4.5	94.8

Table 7.1: Summary of run periods with different hardware threshold values .

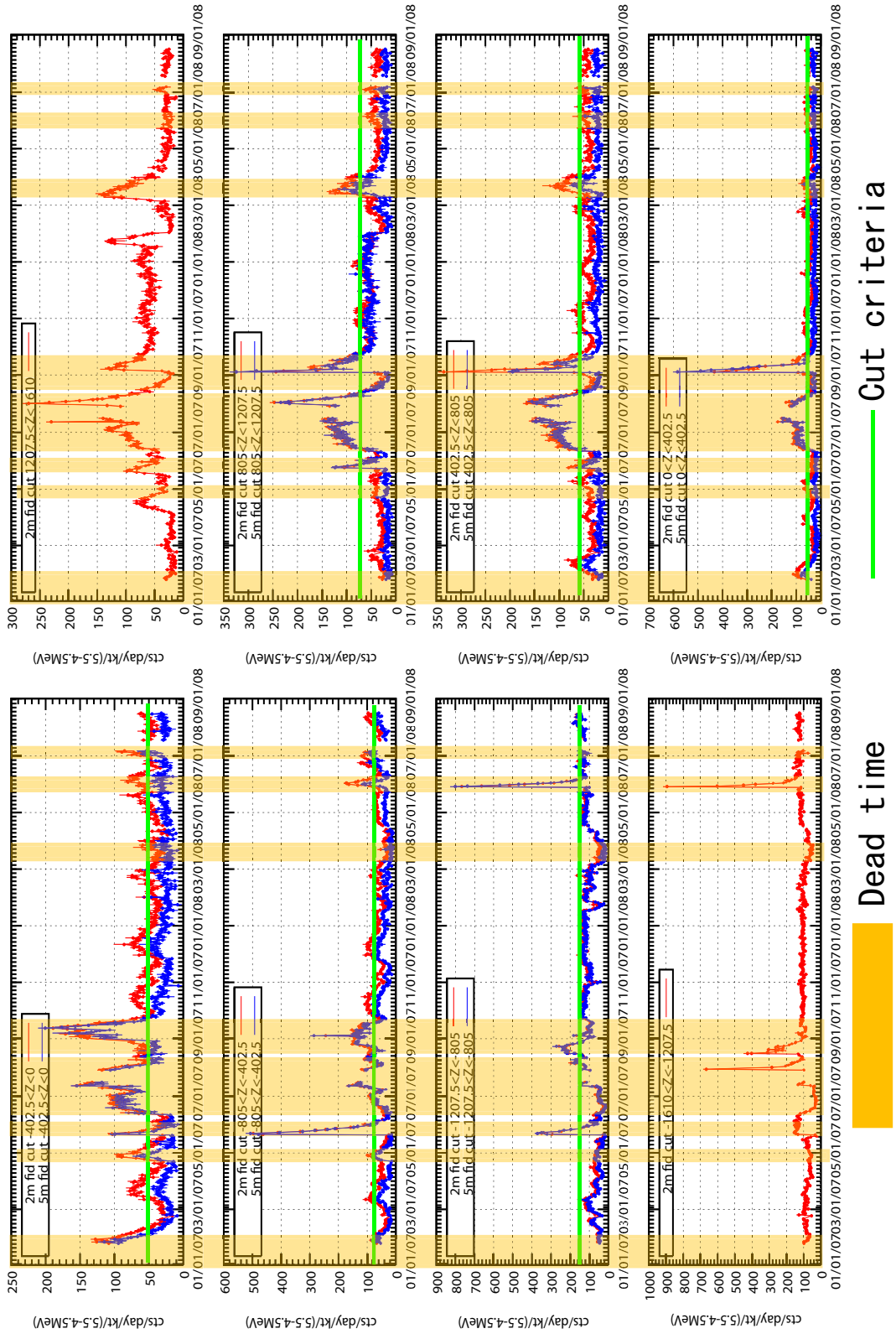

Figure 7.1: Low energy event rates in different Z positions. The horizontal axis is date (mm/dd/yy). The noise cut and quality cuts (not the final tune) are applied.

The data quality is checked with subrun or run unit. The criteria for bad run or subrun are following;

- The run length is less than 5 min.
- The subrun length is less than 30 sec.
- The one of event reduction rates of a subrun is higher than the allowed rate.
- Hardware and/or software problems happen
- Calibration run

7.3 Noise reduction

7.3.1 Total charge cut

Events with the total charge more than 2000 p.e. are rejected. This cut is to remove cosmic ray muons. 2000 p.e. corresponds to about 300 MeV for an electron, so no solar neutrino events are cut by this criterion.

7.3.2 Fiducial volume cut

Events which have vertex position within 2m from the ID wall are rejected. This cut is to reduce background events coming from the surrounding rock or the ID structure. 2m is set considering the resolution of vertex position ($\sim$100cm at 6.5MeV). The volume 2m of the ID wall is called fiducial volume.

A tighter fiducial volume cut is applied for the event with energy less than 5.5 MeV as explained later in this chapter.

7.3.3 Pedestal/Uncompleted event cut

The pedestal data was taken at the beginning and 30 min after the beginning of every run. After that, the 8 online computers, each handles 6 TKO crates, check temperatures of 6 crate in every 30min. If more than or equal to one of 6 TKOs have a different temperature by $\pm$ 0.15 degree from the previous pedestal time, the online computer takes pedestal data for the 6 TKOs. If pedestal data is not taken for more than 6 hours by a online computer, the online computer takes pedestal data for the 6 TKOs.

Other than the pedestal data taking, some parts of the detector happen to become off due to hardware problem. The data taken in such period ($2 \sim 3\%$)is not included in this analysis.

7.3.4 Time difference cut

Events are rejected if they occurred within 50μsec after the previous event. This is to remove electrons from the decay of cosmic ray muons. Figure 7.2 shows the distribution of time interval in a typical data. The fractional dead time due to this cut is $\sim 2 \times 10^{-4}$, which is taken into account in the solar neutrino simulation.

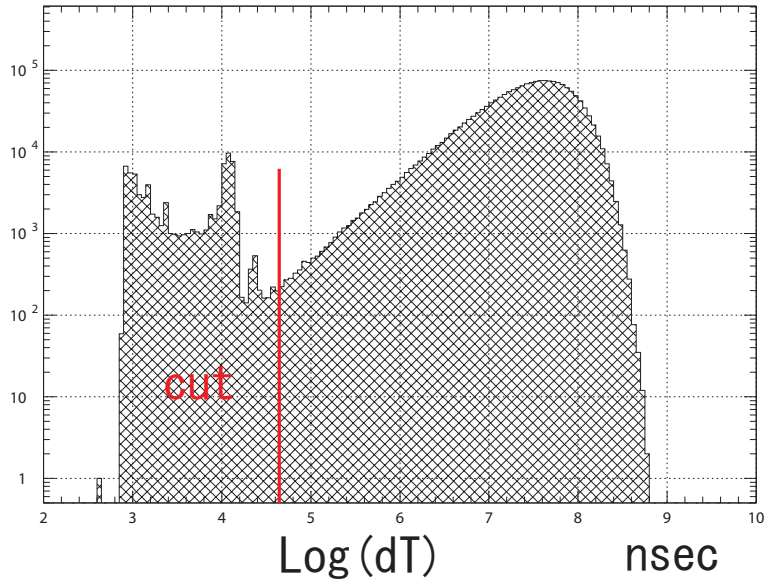

Figure 7.2: Time difference to previous low energy triggered event. The first peak around 1μsec is due to ringing events after a high energy cosmic muon, and the second peak around 15μsec is due to after pulse events, and the third peak around 30μsec is so called "after trigger" event, which is issued after HE triggered event.

7.3.5 OD event cut

Events with an OD trigger are rejected. An OD trigger is issued if the OD hits are more than 19 his within a 200 nsec time window (see Figure 7.3). This is to remove cosmic ray muon event with total p.e. less than 2000 p.e.

7.3.6 Noise cut

Event with high fraction of noise hits are rejected. This is to remove events due to electronic noise. The fraction of noise hits is defined as follows;

$$NSratio = N_{noise}/N_{total} \tag{7.1}$$

where N_{noise} is the number of hit PMTs with charge less than 0.5 p.e., and N_{total} is the total number of hit PMTs. If $NSratio$ is greater than 0.4, the event is rejected. Figure 7.4 shows $NSratio$ distribution of a typical good run.

7.3.7 Goodness of vertex reconstruction cut

Events with poor vertex reconstruction are rejected. Figure 7.5 shows the goodness of the second vertex fitting [20]. If a event has goodness < 0.3, the event is rejected. Some broken PMT made flash light. These flasher events are usually clustered in goodness < 0.3 region.

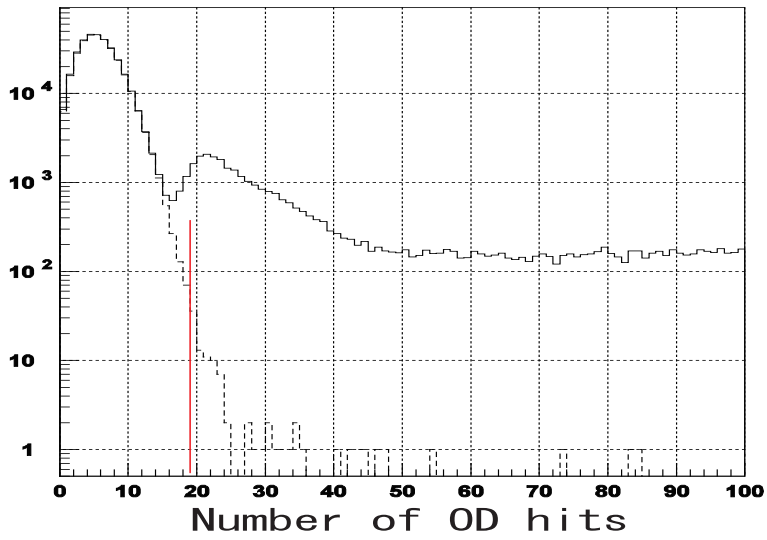

Figure 7.3: Number of OD hits distribution of a typical good run. Solid histogram includes events with OD trigger on. Dashed histogram corresponds to the events with OD trigger off. Events in the right side of the red line are rejected.

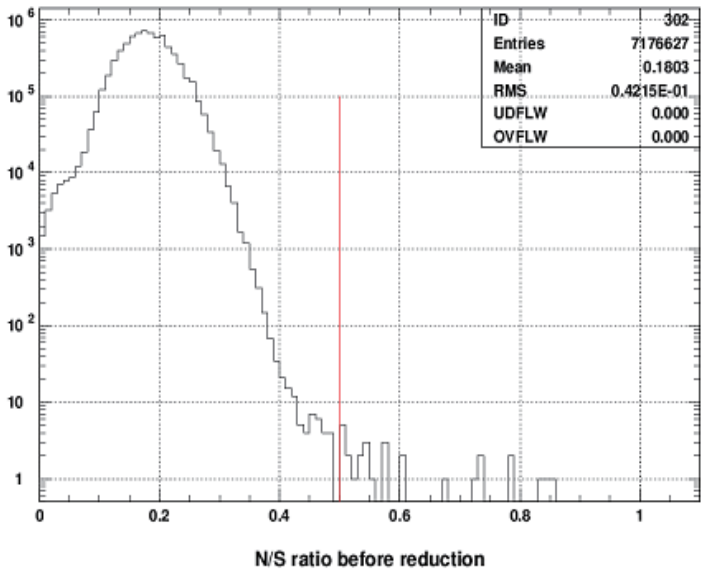

Figure 7.4: N/S ratio in a typical good run. Events in the right side of the red line are rejected.

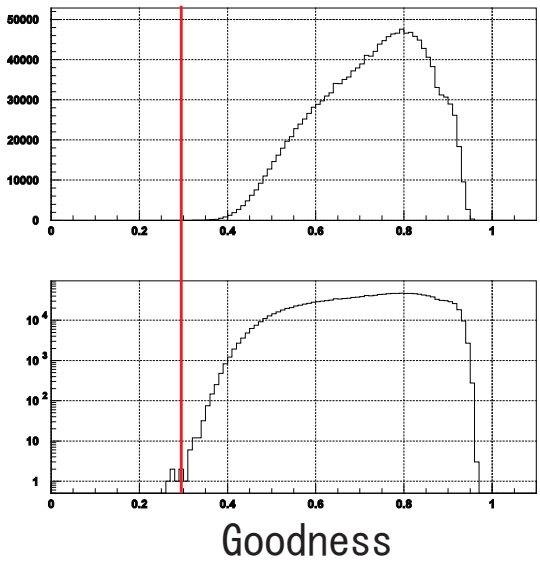

Figure 7.5: Goodness distribution in linear (top) and log (bottom) scale of a typical good run. Events in the left side of the red line are rejected.

7.4 Reduction for solar ν analysis

In this section, I will explain a series of further reductions which select a good single electron events. The total number of events after each reduction step and the efficiencies of each reduction will be summarized at the end of this section, and the systematic uncertainties due to each item of reductions are discussed in Chapter 9

7.4.1 Spallation Cut

This cut is to reject events caused by cosmic ray muons. When a muon interacts with an oxygen, radioactive elements are produced;

$$\mu + {}^{16}O \longrightarrow \mu + X \tag{7.2}$$

where X represents radioactive nuclei. Possible radioactive nuclei are summarized in Table 7.2. The γ and β decay of such a radioactive nuclei trigger the detector and make background events so called "Spallation events", which are main background source in energy region 6.5 to 20 MeV. Here, I explain an overview of spallation event cut. The details of muon selection, muon track reconstruction, and how to built a likelihood function to identify a spallation event was described in [20].

For each low energy event, a likelihood value is calculated for every preceding muon within 100 sec. The likelihood is a product of three functions;

$$L_{spa} = f(\Delta t) \times f(\Delta l) \times f(Q_{res}) \tag{7.3}$$

where Δl is a distance from the low energy event vertex to the reconstructed muon track. Δt is a time difference between the low energy and a preceding muon event. Q_{res} is a residual

Isotope	$\tau_{\frac{1}{2}}$(sec)	decay mode	Kinetic Energy (MeV)
$^{8}_{2}He$	0.119	β^-	9.67 + 0.98(γ)
		β^- n	16%
$^{8}_{3}Li$	0.838	β^-	$\sim$ 13
$^{8}_{3}B$	0.77	β^+	13.9
$^{9}_{3}Li$	0.178	β^-	13.6 (50.5 %)
		β^- n	($\sim$ 50 %)
$^{9}_{6}C$	0.127	β^+ n	3$\sim$15
$^{11}_{3}Li$	0.0085	β^-	16$\sim$20 ($\sim$ 50 %)
		β^- n	$\sim$ 16 ($\sim$ 50 %)
$^{11}_{4}Be$	13.8	β^-	11.51 (54.7 %)
			9.41 + 2.1 (γ) (31.4 %)
$^{11}_{4}Be$	0.0236	β^-	11.71
$^{12}_{5}B$	0.0202	β^-	13.37
$^{12}_{7}N$	0.0110	β^+	16.32
$^{13}_{5}B$	0.0174	β^-	13.44
$^{13}_{8}O$	0.0086	β^+	13.2 16.7
$^{14}_{5}B$	0.0138	β^-	14.55+6.09 (γ)
$^{15}_{6}C$	2.449	β^-	9.77 (36.8 %)
			4.47+5.30 (γ)
$^{16}_{6}C$	0.747	β^- n	$\sim$ 4
$^{16}_{7}N$	7.13	β^-	10.42 (28.0%)
			4.29+6.13 (γ) (66.2%)

Table 7.2: Possible Spallation products in water [20]

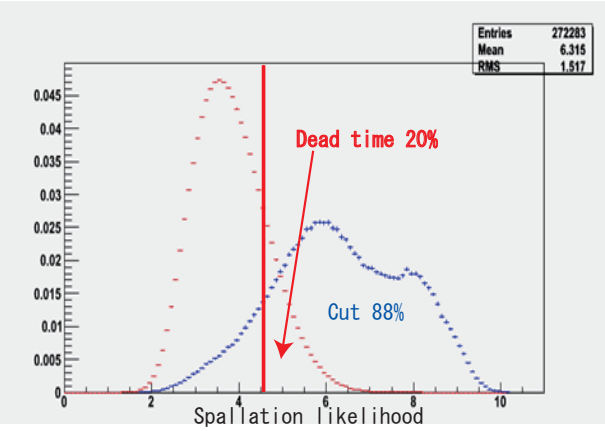

Figure 7.6: Spallation likelihood distribution. Blue histogram shows spallation like events, and red histogram shows random sample (The areas are normalized).

charge of the preceding muon which is defined as

$$Q_{res} = Q_{total} - Q_{unit}(t) \times L_{\mu} \tag{7.4}$$

the Q_{total} is the total charge (p.e.) of a muon event, $Q_{unit}(t)$ is the average number of photo electrons per unit length of a muon track observed in a time period t .

The spallation likelihood for a low energy event then obtained as the maximum value of the likelihood values, and the muon which gives the maximum value is called a parent muon. Figure 7.6 shows the distribution of the spallation likelihood in spallation like event and randomly sampled events. For spallation like event, events with $\Delta t < 0.1$sec and energy$>$ 8MeV are selected. For a random sample, events with energy $<$5MeV are selected because most of such low energy events are produced near the detector wall due to radioactive impurities and are not to spallation event. A random vertex is assigned to the vertex position of the random sample event. The cut point for the spallation likelihood is 4.52, so that the inefficiency of the random sample (dead time) becomes 0.20. The position dependence of the dead time is shown Figure 7.7. This position dependence is taken into account when the expected number of solar neutrino events is calculated using MC.

7.4.2 Ambient background reduction

Vertex and Angular Reconstruction Quality check

There still remain many background events due to mis-reconstruction inside the fiducial volume after noise reduction. To check the quality of vertex and angular reconstruction and remove the mis-reconstructed events, the 2 dimensional vertex and angular goodness cut is applied. Since the mis-reconstruction usually occurs for low energy background ($<\sim$ 6MeV), such events has small number of hits. Thus, there is no hit selection to calculate goodness of vertex reconstruction, so that we get information as much as possible from all hit PMTs. The

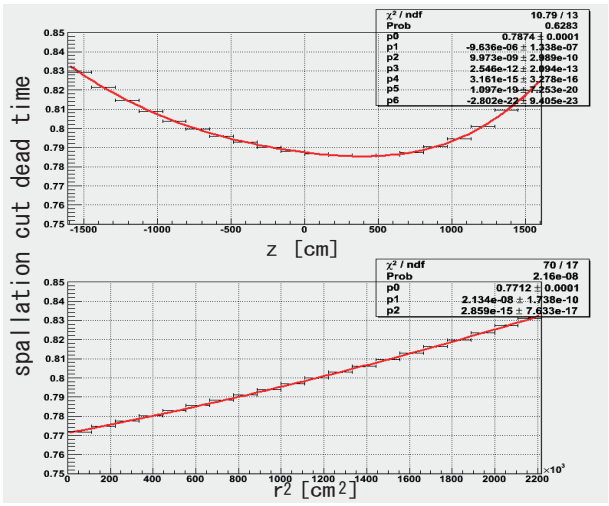

Figure 7.7: Spallation cut dead time depending on the detector position.

goodness vertex reconstruction is calculated using all hit PMT timing as follows,

$$G_V = \frac{\sum e^{-\frac{1}{2}\ (\frac{\tau_i(\vec{v})-t_0}{\omega})+(\frac{\tau_i(\vec{v})-t_0}{\sigma})^{\ 2}}}{\sum e^{-\frac{1}{2}(\frac{\tau_i(\vec{v})-t0}{\omega})^2}} \tag{7.5}$$

where $\tau_i(\vec{v}) = t_i - |\vec{v} - \vec{h}_i|/c$ is a TOF subtracted hit time, and t_0 is the fitted peak time of τ distribution. The sums are over all hits.

The goodness of angular reconstruction can be tested by checking how the hit PMTs distribute in space. In the case of a real electron event, the hit PMTs should reside uniformly along with Cherenkov ring toward the reconstructed direction. To check the uniformity, the Kolomogorov-Smirnov test is applied. Figure 7.8 shows examples of event displays for a single electron event and a background event. Figure 7.8 also shows the distribution of azimuth angle of hit PMTs with respect to the reconstructed direction. The definition of goodness is the full width of azimuth angle deviation which is given by

$$G_A = \frac{max\left\{\angle_{uniform}(i) - \angle_{Data}(i)\right\} - min\left\{\angle_{uniform}(i) - \angle_{Data}(i)\right\}}{2\pi} \tag{7.6}$$

where $\angle_{uniform}(i)$ is the azimuth angle of i-th hit PMT among the N_{50} assuming that the hit PMTs are uniformly distributed along with a Cherenkov cone (the dashed line in Figure7.8), and $\angle_{Data}(i)$ is that of real event (the closed circles in Figure7.8). As shown in the figures, a good event has a small value and a bad event has a large value.

The correlation between the vertex goodness G_V and the angular goodness G_A is shown in figure 7.9. Figure 7.9-(a) is a plot of real data which is just after the 1st reduction and still contains a lot of badly reconstructed events, and figure 7.9-(b) is that of solar neutrino MC. As shown in the figure, we can separate a good single electron like event from background events by checking a quality factor which is a combination of the vertex goodness and the angular goodness *ovaQ* (One dimensional variable of Vertex and Angular reconstruction Quality);

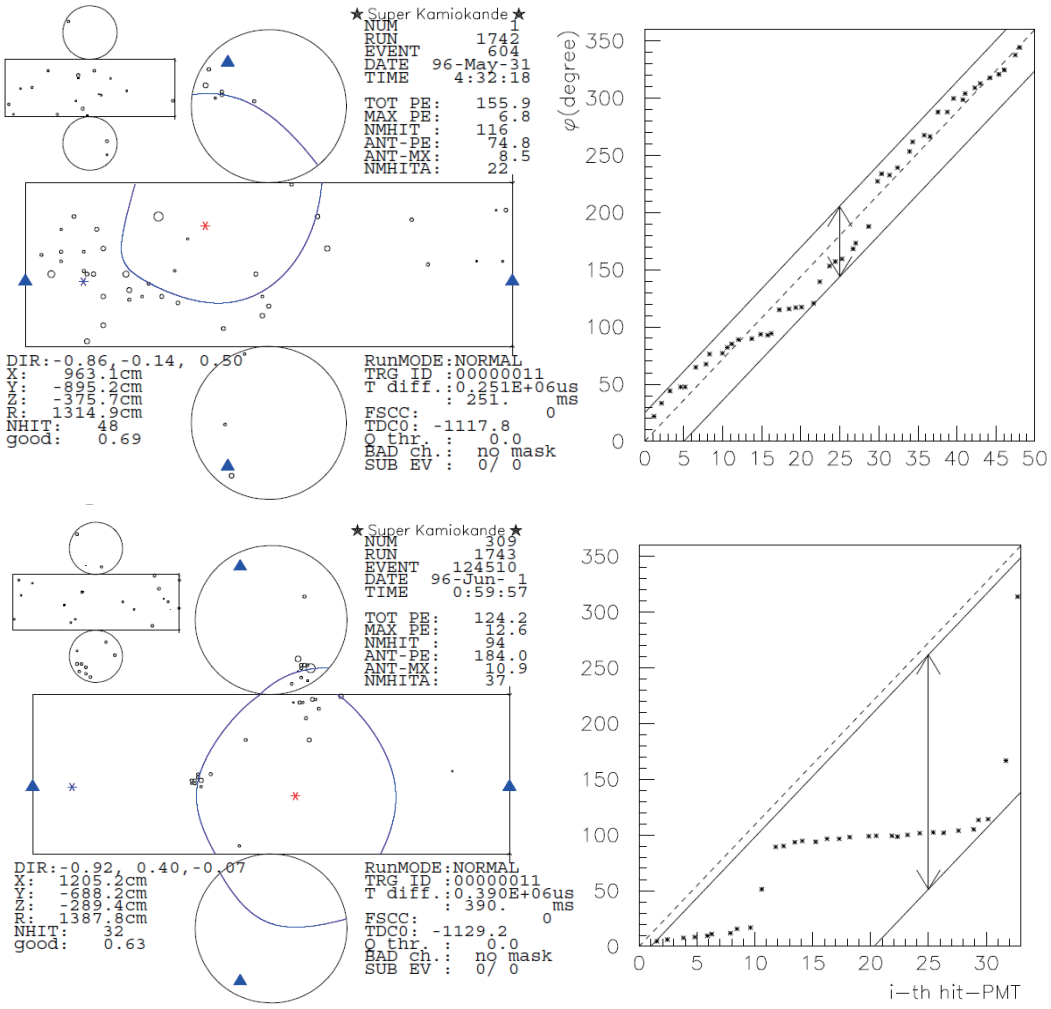

Figure 7.8: Examples of direction KS test for good event (top) and bad event (bottom).

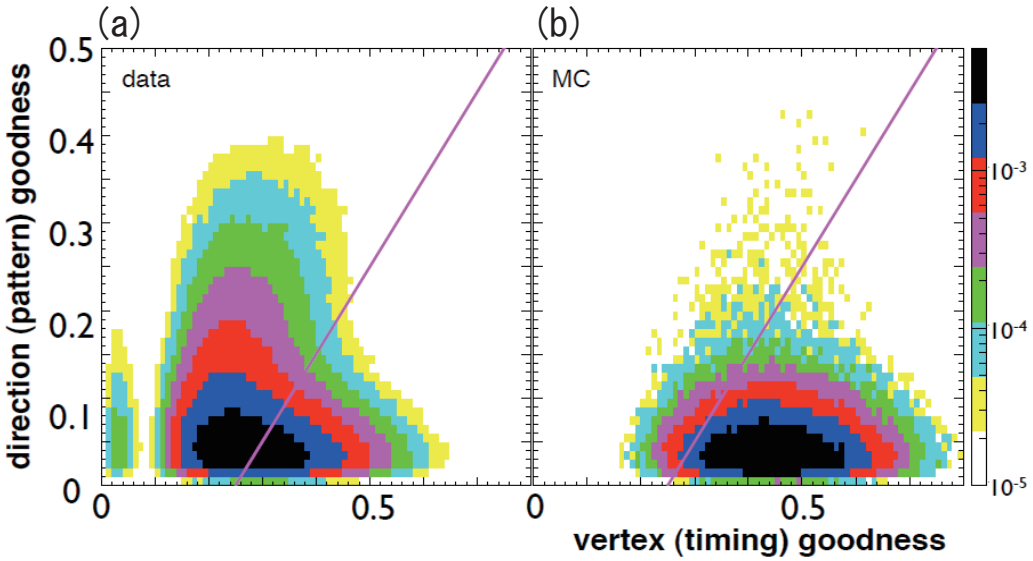

Figure 7.9: Correlation of G_V^2(horizontal) and G_A^2(vertical). Line indicate $G_A^2 = G_V^2 - 0.25$

$$ovaQ \equiv G_V^2 - G_A^2 \tag{7.7}$$

Distributions of the quality factor for several energy are shown in figure 7.10. The cut criteria is following;

$$\begin{cases} ovaQ > 0.29,\ 4.5 \leq Energy < 5.0MeV \\ ovaQ > 0.25,\ 5.0 \leq Energy < 7.5MeV \\ ovaQ > 0.20,\ Energy \geq 7.5MeV \end{cases} \tag{7.8}$$

Flasher cut

If there is a PMT which emits light because of arch discharge on dynodes, such a PMT causes background events so called "flasher events". The flasher event is characterized with a large charge hit and many hits in the surrounding PMTs.

Figure 7.11 shows the maximum charge of a PMT in an event for the horizontal axis, and the number of hits in the surrounding 24 PMTs. The cut criteria are also shown in the Figure 7.11.

Hit Pattern cut

This cut is to select a clean single electron event. If additional γ-rays in an event, the hit pattern does not show a clear Cherenkov ring, then the reconstructed direction might not be correct. To select a single electron event, a likelihood function is made from $\cos\theta_{dir,i}$ distribution of the uniform electron MC event; Figure 7.14 shows examples of the Cherenkov ring probability

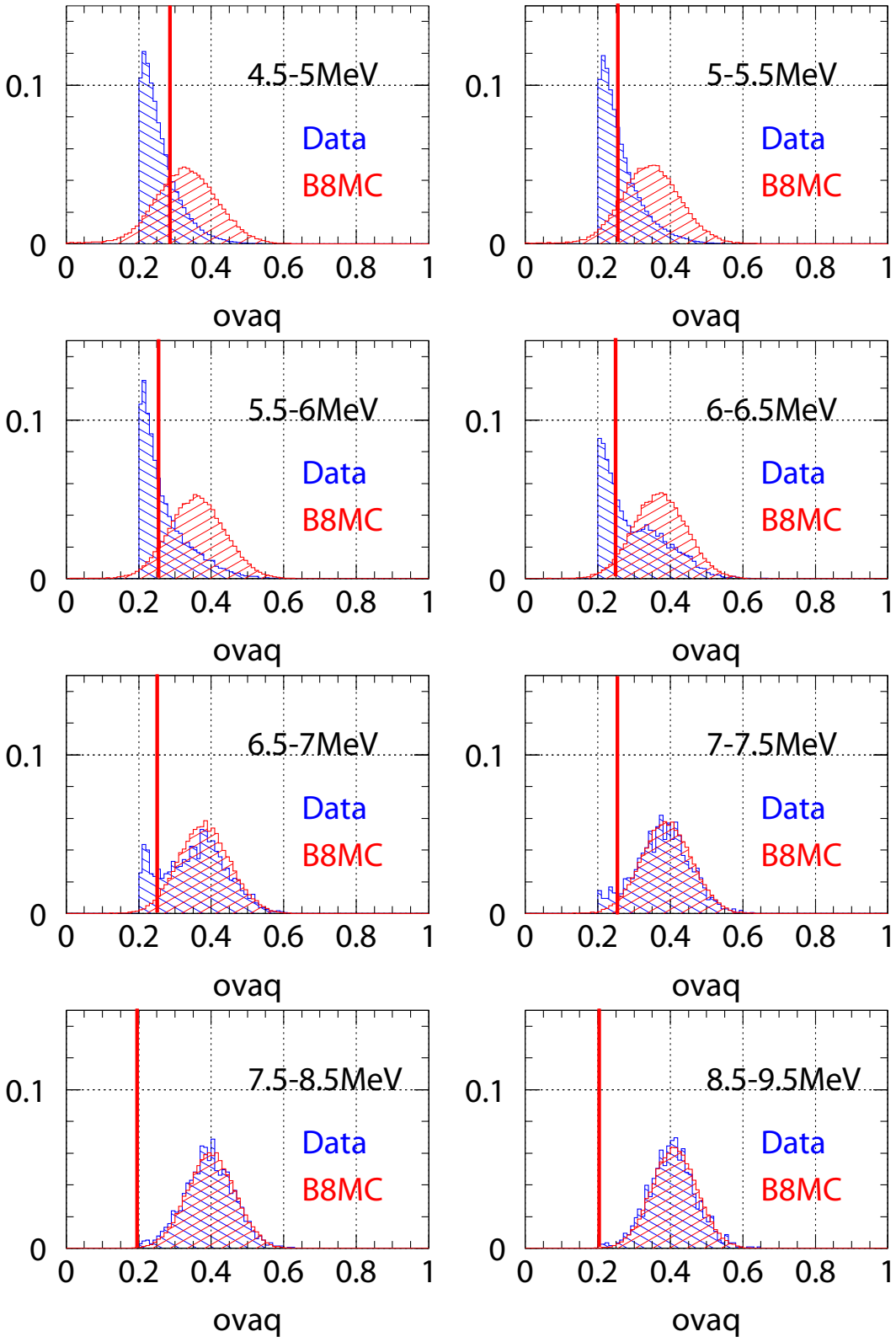

Figure 7.10: *ovaQ* distribution of different energy region.

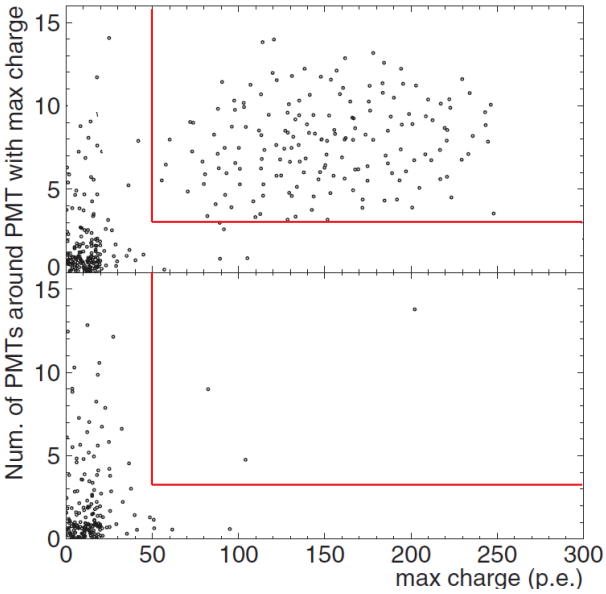

Figure 7.11: 2 dimensional cut of flasher events. The top figure contains flasher sample, while the bottom figure shows a typical good run.

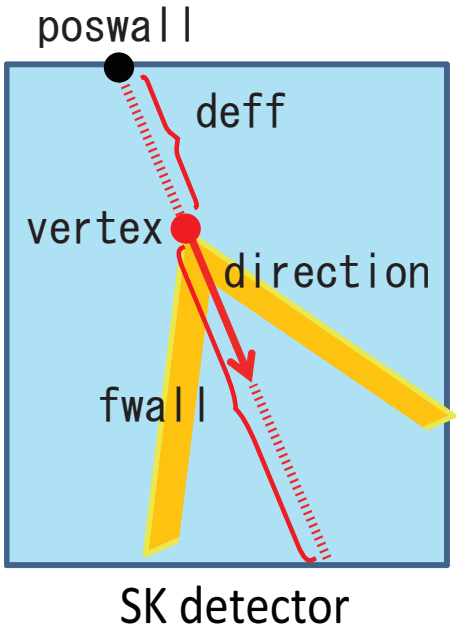

Figure 7.12: Definition of variables which appear in hit pattern cut and gamma-ray cut.

functions for several energy regions. The definition of Cherenkov ring probability is

$$P(Energy, vertex, diretion) = \frac{1}{N_{50}} \sum_{i}^{N_{50}} \log(f(Energy, \cos\theta_{dir,i}, fwall)) \tag{7.9}$$

where $fwall$ is the distance from the event vertex to the detector wall (See Figure 7.12) along with the reconstructed direction, and probability functions $f(Energy, \cos\theta_{dir.i}, fwall)$ are obtained from single electron MC with different energies. To determine the cut point of P, the significance is calculated as

$$Significance(P) = \frac{\int_{P_0}^{P} MC(P')dP'}{\sqrt{\int_{P_0}^{P} BG(P')dP'}} \tag{7.10}$$

where $MC(P)$ and $BG(P)$ are distributions of the Cherenkov ring probability obtained from single electron MC and control sample of real data and P_0 is the likelihood value at the left edge of Figure 7.13. The obtained cut criteria which give maximum significance for different energy regions are

$$\begin{cases} P > -1.88, & 6.5MeV \leq Energy < 8.0MeV \\ P > -1.86, & 8.0MeV \leq Energy < 12.0MeV \\ P > -1.95, & 12.0MeV \leq Energy \end{cases} \tag{7.11}$$

Since, for an event whose energy is less than 6.5 MeV, the distributions of likelihood for data and solar neutrino MC become the same (see Figure 7.14), I decided not to use this cut for the energy region.

Fiducial volume cut using the second vertex fitter

The result of second vertex reconstruction is checked here. If the reconstruction returns a vertex position outside of the fiducial volume (2m inside of the ID wall), the event is rejected.

7.4.3 Gamma-ray cut

This cut is to reject events induced by gamma-ray which are from the PMTs or the detector wall. To eliminate the background, events with direction inward from the wall are rejected. The criteria for event energy $\geq 6.5MeV$ are

$$\begin{cases} d_{eff} > 650cm, & 6.5MeV \leq Energy < 8.0MeV \\ d_{eff} > 400cm, & 8.0MeV \leq Energy \end{cases} \tag{7.12}$$

where $d_{eff}$is the distance from the wall in the direction of the reconstructed event (see Figure 7.12), and this cut points are obtained by calculation of significance as in Equation 7.10 but the significance here is a function of d_{eff}.

Figure 7.15 shows the distribution of d_{eff} for different energy regions. Because the radioactive background (energy <6.5 MeV) is not uniformly distributed in the detector (see **??**), a tighter fiducial volume cut is needed. Considering the tighter fiducial volume which will be tuned in the later step, events in the central area ($z > -5$m,r< 13m) are selected to tune the gamma-ray cut point of d_{eff} for energy $< 6.5MeV$ region. Then, for this energy region, different

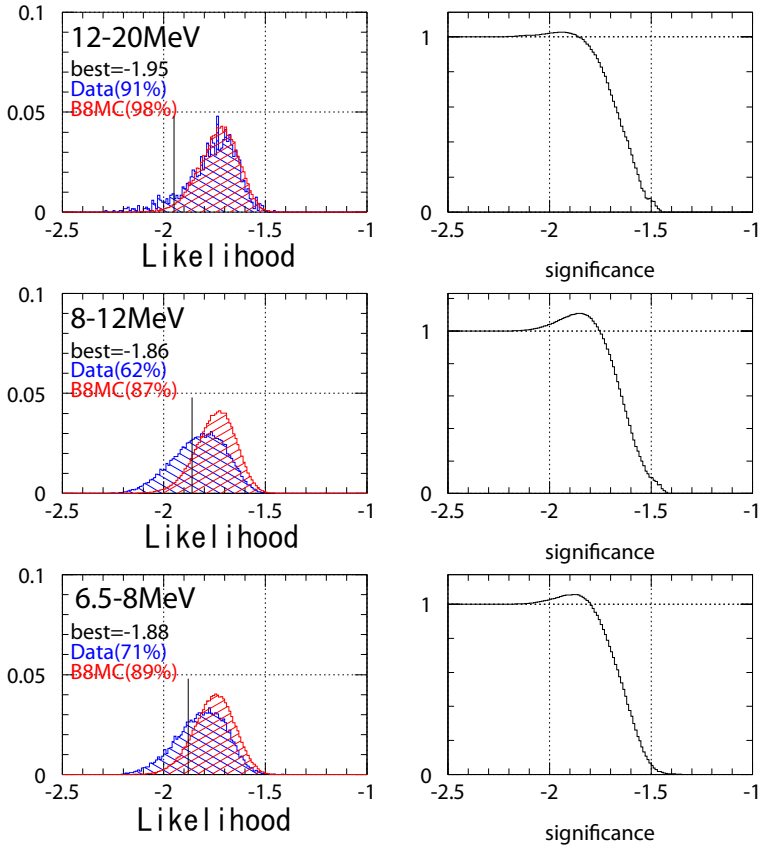

Figure 7.13: Hit pattern likelihood distribution of data and solar neutrino MC in E>6.5MeV.

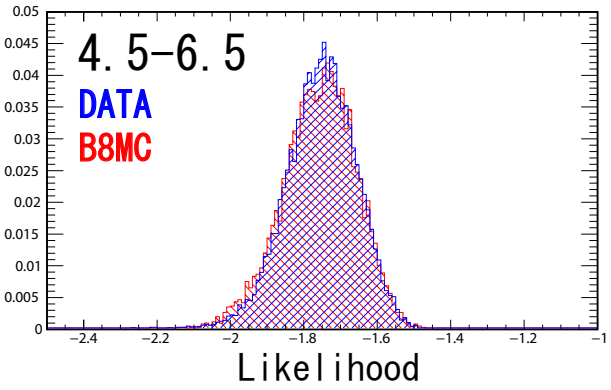

Figure 7.14: Hit pattern likelihood distribution 4.5≤E<6.5MeV.

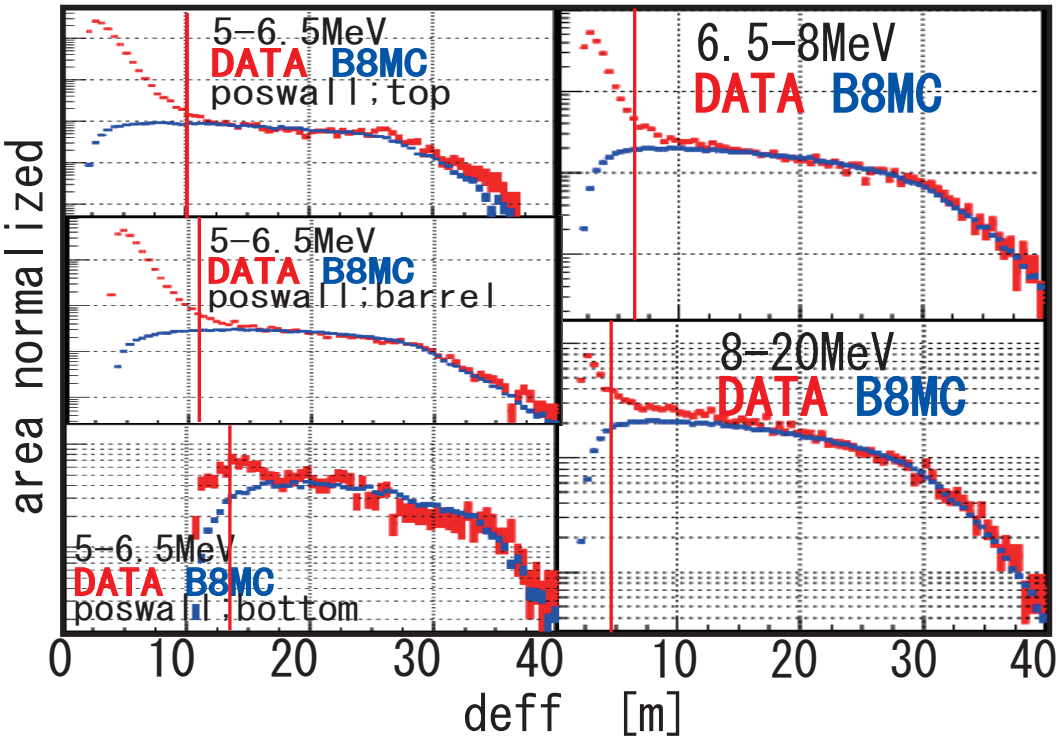

Figure 7.15: d_{eff} distribution for different energy regions. The cut criteria are indicated in the line.

cut criteria are applied depending on where the original position at the detector wall (poswall) is (see Figure 7.15);

$$\begin{cases} d_{eff} > 1000cm, & \text{poswall is top} \\ d_{eff} > 1100cm, & \text{poswall is barrel} \\ d_{eff} > 1300cm, & \text{poswall is bottom} \end{cases} \tag{7.13}$$

7.4.4 Cosmogenic ^{16}N cut

This cut is to reject events caused by decay of ^{16}N The ^{16}N is produced when cosmic ray μ^- is captured by ^{16}O in water;

$$\mu^- + ^{16}O \longrightarrow ^{16}N + \nu \tag{7.14}$$

The most of ^{16}N produces a 6.1 MeV γ with a β whose end point energy is 4.3 MeV; its half life is 7.13 second.

In order to reject this background, the correlation between all captured muons and all remaining low energy event are checked. The first step is to select only captured muon event which are characterized as following; Muon with no exit point(stopping muon) and is not followed by a decay electron event in 100μsec. After the selection, a low energy event within 250cm from the

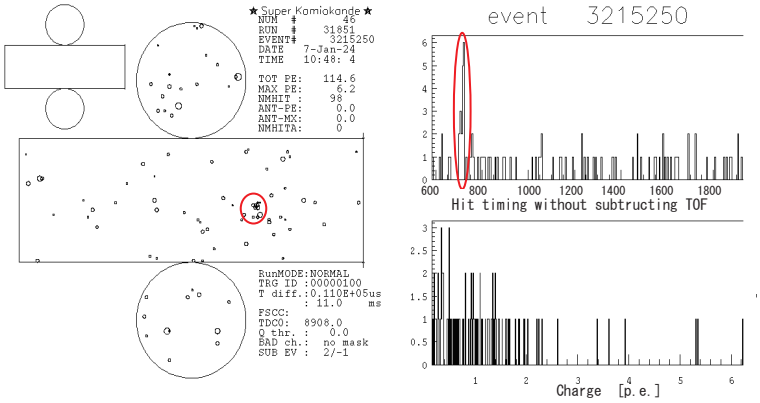

Figure 7.16: A typycal event display of low-energy background.

stopping point of the captured muon and a time-window of 100msec to 30sec following the muon is rejected. The total number of the rejected events 4750 events. The dead time due to this cut is estimated accidental coincidence between the selected muons and random event sample which is 0.53%.

7.4.5 Further quality cut for the lowest energy region

Clustering hits background

This cut is newly developed in this analysis to reduce the low energy background in edge region. Figure 7.16 shows one example of remaining background. This kind of event is supposed to be triggered by a coincidence of dark hits and the small clustering hits due to radioactive sources in the FRP or the structure of the detector wall.

We can separate this background from the solar neutrino signals by searching a small cluster in both space and time. A real neutrino signal at the edge region also has similar characteristics, but it causes a bigger cluster compared to the background events. Thus, the key is to evaluate the size of clustering hits.

In order to do this, two variables are used. One is to check the size of clustering hits in space; the minimum distance from any of N_{20} PMTs to another N_{20} PMT within which more than 0.2 number of N_{20} are included (called "$R02$"). The other variable is to check the clustering hits in time; the maximum number of hits in 20nsec sliding time window search "without" subtracting TOF from the reconstructed vertex (called "$N20_{rawT}$"). The reason why TOF is not subtracted is that for the background case, except for the small clustering, hit PMT positions should be randomly distributed while for the real signal in the edge of fiducial volume, hit PMT positions should be concentrated close to the wall. Thus, timing distribution without subtracting TOF makes the difference between the background and the signal clearer.

Figure 7.17 shows correlation between $R02$ and $N20rawT$ for background sample data and solar neutrino MC events. The background sample is selected from the data after the gamma cut applied around the edge of fiducial volume (r>13m). To compare the background with MC events, the same cuts are applied. As expected, the background sample shows smaller $R02$ and smaller $N20_{rawT}$ (which is indicated by the orange area in Figure 7.17). The cut point

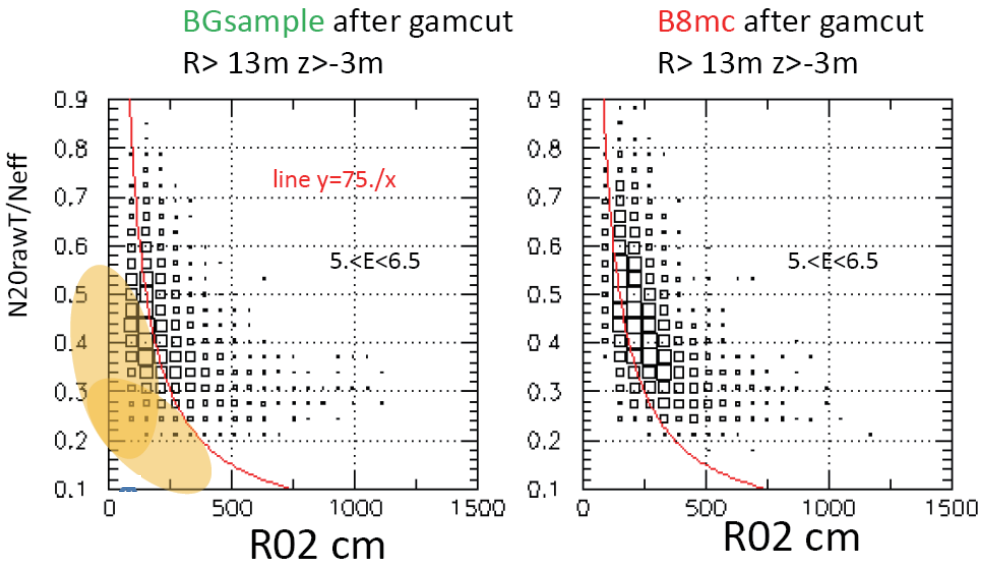

Figure 7.17: Correlation between $R02$ and $N20rawT$ for background sample (left) and solar neutrino MC events (right).

is obtained from one dimensional distribution of $R02 \times N20_{rawT}/N_{eff}$. The significance as a function of $R02 \times N20_{rawT}/N_{eff}$ becomes maximum at $R02 \times N20_{rawT}/N_{eff} = 75$ (see Figure 7.18). Following is a summary of cut criteria of this new cut;

$$\begin{cases} R02 \times N20_{rawT}/N_{eff} > 75 \; and \; r^2 > 180m^2 \text{ for } 5.5 \leq \text{E} < 6.5 \text{ MeV} \\ R02 \times N20_{rawT}/N_{eff} > 75 \; and \; r^2 > 155m^2 \text{ for } 5.0 \leq \text{E} < 5.5 \text{ MeV} \\ R02 \times N20_{rawT}/N_{eff} > 75 \; and \; r^2 > 120m^2 \text{ for } 4.5 \leq \text{E} < 5.0 \text{ MeV} \end{cases} \tag{7.15}$$

After these cut applied, the vertex distributions in low-energy events are shown in Figure 7.19.

Tighter fiducial volume cut

This cut is to reject the remaining background in the edge region. As shown in Figure 7.19, background events in the bottom region still remain after the cluster cut. This nonuniformity of the vertex distribution of background makes the angular distribution of the background distorted, which causes a large systematic uncertainty for day-night asymmetry of solar neutrino flux.

To set a tight fiducial volume, the significance as a function of detector radius is calculated. Based on the significance calculation, the final value of fiducial volume is obtained for each energy region which is shown in Figure 7.19:

$$\begin{aligned} 4.5 - 5MeV: \quad & (r^2 < 180m^2 and z > -3m) or (r^2 < 120m^2 and -7 < z < 3m) = 12.3kton \\ 5 - 5.5MeV: \quad & (r^2 < 180m^2 and z > -7.5m) = 13.3kton \\ 5.5 - 20Mev: \quad & \text{no tight fiducial volume cut} = 22.5kton \end{aligned}$$

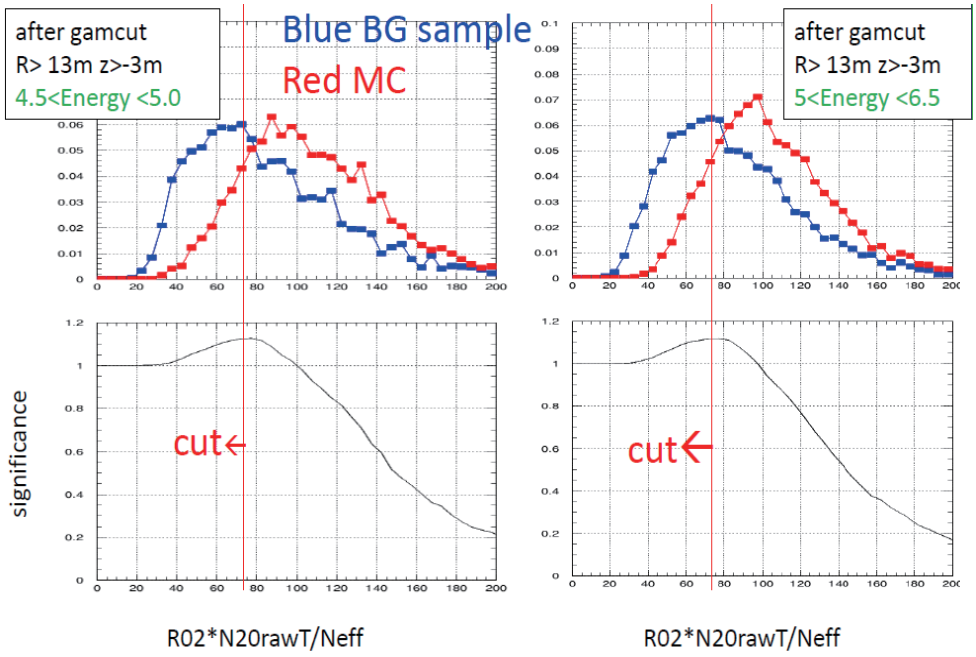

Figure 7.18: Distribution of $R02 \times N20_{rawT}/N_{eff}$ and the significance.

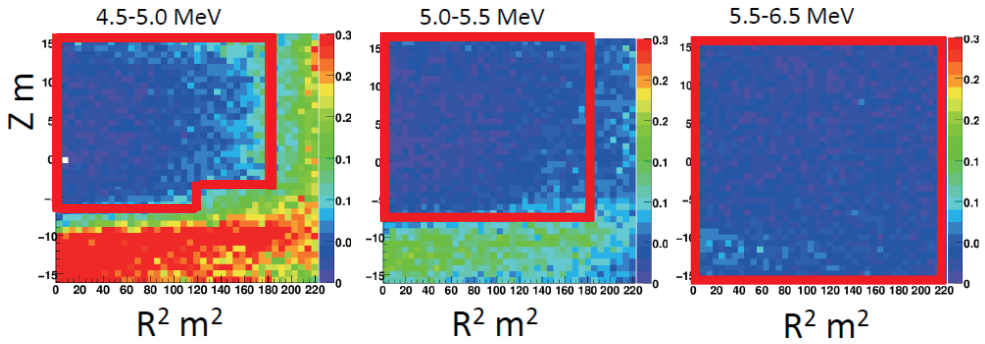

Figure 7.19: Vertex distribution of low-energy events. The tight fiducial volume is shown by the red box: 12.3kton for 4.5-5MeV, 13.3kton for 5-5.5MeV and 22.5kton 5.5-20MeV.

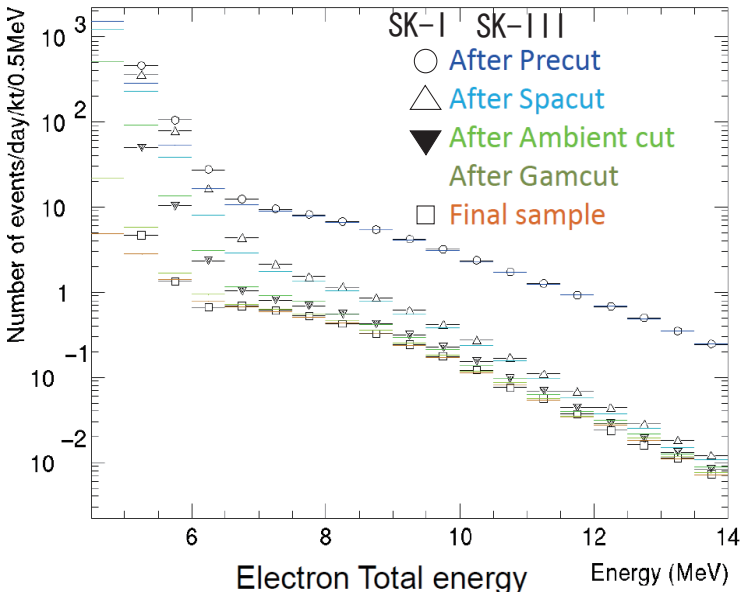

Figure 7.20: Number of event after each reduction step as a function of energy. Precut in SK-I (open circle) means noise reduction. For and SK-III(blue) there still remained lots of low-energy events due to FRP. Thus, $ovaQ > 0.2$ is applied for all events, and this is called precut in SK-III.

7.5 Summary of Reduction step

Figure 7.20 shows the energy spectrum after each step of the reductions and Figure 7.21 shows the remaining efficiency of ^8B solar neutrino MC with respect to the reconstructed energy. While the event rate in the real data as a function of energy is the same as SK-I, the cut efficiencies are improved by 10% in the final data sample. For 4.5-5MeV region, while the efficiency gets worse by about 30% compared to SK-I, the background is reduced by about 80%, which enables to observe the solar neutrino signals in that energy region with better signal to noise ratio. The number of events after each reduction step is summarized in Table 7.3 (real data) and 7.4.

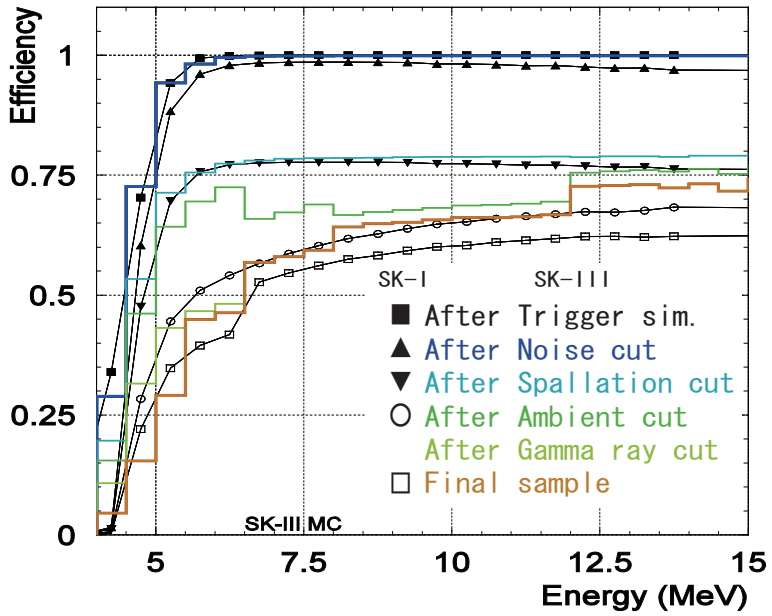

Figure 7.21: Reduction efficiency for the solar neutrino MC simulation. Color lines show SK-III and Makers show SK-I (From top; after SLE trigger, noise reduction, spallation cut, ambient BG reduction, and final data sample)

Reduction step	4.5-20.0 MeV	5.0-20.0 MeV	6.5-20.0 MeV
Precut	10162637	2381464	669641
Spallation cut	8324066	1861770	114350
ovaQ	1795878	866835	100470
Second fidv. cut	1609465	734843	89808
Hit pattern cut			58187
Gamma ray cut	89096	54820	43146
^{16}N cut	89096	54351	39879
Cluster cut	67774	42916	
Tight fidv. cut	13346	24311	
Final	13346	24311	39879

Table 7.3: Reduction results of data

Reduction step	4.5-5.0 MeV	5.0-6.5 MeV	6.5-20.0 MeV
Total	502745	1277710	1932146
Bad run cut	428206	1098880	1672114
Trigger condition	225121	920427	1670429
Goodness cut	225119	920424	1670429
Fiducial volume cut	211920	748352	1310258
Precut	196572	724259	1295878
Flasher events cut	196572	724259	1295878
Spallation cut	155869	574679	1029365
ovaQ	136319	537522	1020542
Secont fidv cut	135223	527545	998017
Hit pattern cut			889857
Gamma ray cut	92326.8	355474	815156
Cluster cut	87390.7	341162	
Tight fidv cuts	45109.5	308757	
Final	45109.5	308757	815156

Table 7.4: Reduction results of MC

Chapter 8

Signal extraction

8.1 Solar angle fitting

The strongest information which is used to extract solar neutrino signal from the final sample is the direction of the recoil electrons because the direction of the recoil electron is strongly correlated with the direction of the incident neutrino. Thus, by checking the cosine of the direction from the Sun and the event direction ($\cos\theta_{sun}$), the solar neutrino signals can be extracted. The signal extraction is done by an extended maximum likelihood fit [43] with data and the solar neutrino MC events distributions. The likelihood function is

$$L = e^{-(\sum_i B_i + S)} \prod_{i=1}^{N_{bin}} \prod_{j=1}^{n_i} (B_i \cdot b_{ij} + S \cdot Y_i \cdot s_{ij}) \tag{8.1}$$

where $N_{bin} = 22$ is the number of bins between 4.5 MeV and 20.0 MeV: 19 energy bins of 0.5 MeV between 4.5 and 14.0 MeV, two energy bins of 1 MeV between 14.0 and 16.0 MeV, and one bin between 16.0 and 20.0 MeV [1] . and n_i is the number of observed events in the i-th energy bin. S and B_i are free parameters to be fitted and represent the total number of solar neutrino events and the number of background in the i-th energy bin. Y_i is the expected fraction of signal events in the i-th energy bin which will be explained in the next section. The probability density functions b_{ij} and s_{ij} describe the expected shapes of the background and recoil electron signal respectively, and are defined for each energy bin as a function of the solar angle.

$$b_{ij} = u(\cos\theta_{ij}) \tag{8.2}$$

$$s_{ij} = p(\cos\theta_{ij}, E_{ij}) \tag{8.3}$$

where θ_{ij} and E_{ij} are a solar angle and energy of j-th event in i-th energy bin. The definition of the solar angle ($\theta_j \equiv \theta_{Sun}$) is shown in Figure 8.1. The background shape is not completely flat due to the cylindrical shape of the detector. To estimate the shape of background, at first, the zenith angle and azimuthal distributions of real data ($\cos\theta_{sun} < 0.7$ is imposed to avoid solar signal) are fitted with an eighth-order polynomial. Then, the expected solar angle distribution can be obtained from the fitted zenith and azimuthal distributions by generating a toy MC. The

[1] If the threshold is 5.0 MeV, the number of bins are 21 bins: 18 energy bins of 0.5 MeV between 5 and 14.0 MeV, two energy bins of 1 MeV between 14.0 and 16.0 MeV, and one bin between 16.0 and 20.0 MeV. That is, $i = 2 \sim 22$ is for 5MeV threshold, and $i = 5 \sim 22$ is for 6.5MeV threshold.

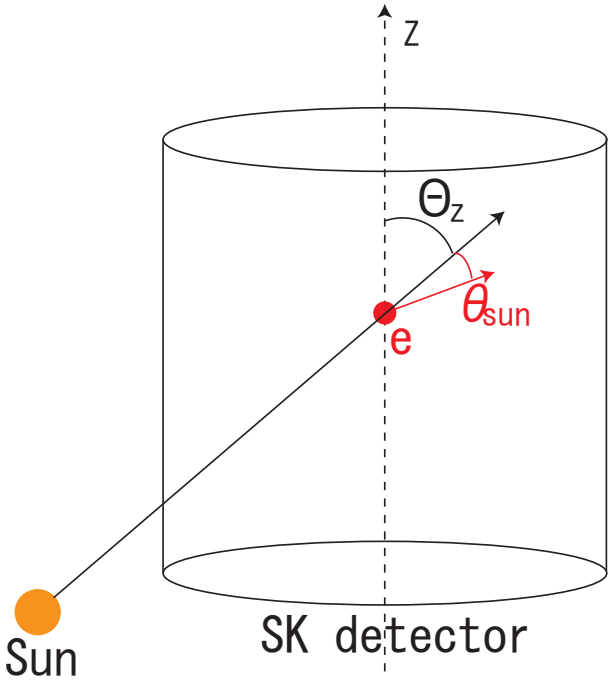

Figure 8.1: Definition of Θ_z and θ_{sun}.

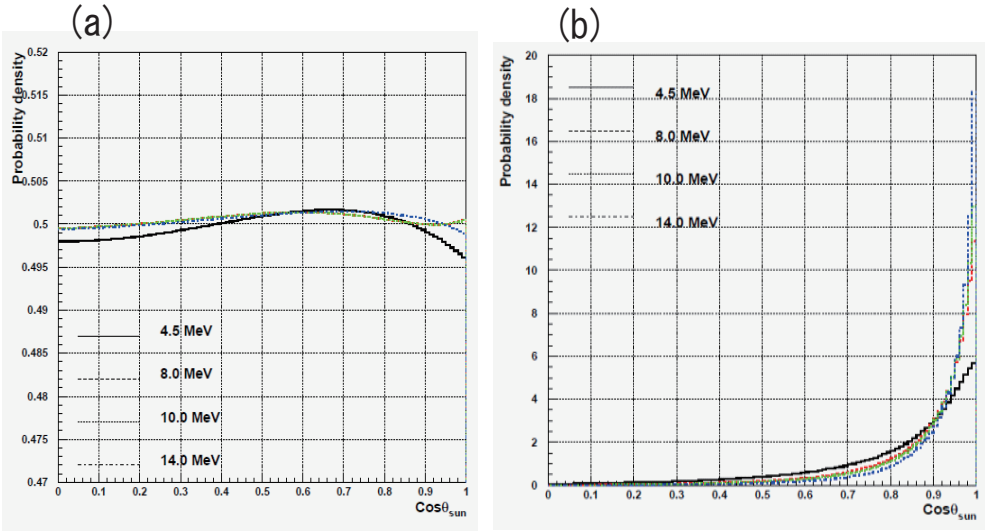

Figure 8.2: Distributions of $\cos\theta_{sun}$ for the expected background (a) and the solar neutrino MC events (b).

signal shape is obtained from the known neutrino-electron elastic scattering which is smeared by electron multiple scattering in water and the detector's angular resolution. Figure 8.2 shows some examples of the expected background shapes and solar neutrino signal shapes. Finally, the values B_i and S are chosen so the likelihood has a maximum value.

8.2 How to get Y_i

As denoted in the previous section, Y_i is the expected fraction of signal events in the i-th energy bin. Y_i can be calculated as follows:

1. Based on the ^8B spectrum in section 2.2, calculate the recoil electron energy distribution of the elastic scattering:
$$\nu_e + e^- \longrightarrow \nu_e + e^- \tag{8.4}$$

2. Obtain the total electron energy distribution to be observed considering the detector response.

3. Calculate the expected total number of signal events and the expected number of signal events in each energy bin.

To obtain the recoil electron energy distribution, the cross section of the reaction in equation 8.4 is given [44]

$$\frac{d\sigma}{dT_e} = \frac{G_F^2 m_e}{2\pi}\left[A_0 + B_0\left(1 - \frac{T_e}{E_\nu}\right)^2 + C_0\frac{m_e T_e}{E_\nu^2}\right] \tag{8.5}$$

where G_F, m_e, E_ν, T_e, are the Fermi coupling constant, the electron mass, the incident neutrino energy and the kinetic energy of the recoil electron, respectively (see Figure 8.3-(b)). The A_0, B_0, C_0 are defined by

$$A_0 = (g_V + g_A)^2, B_0 = (g_V - g_A)^2, C_0 = (g_A^2 - g_V^2) \tag{8.6}$$

$$\begin{cases} g_V = 2\sin^2\theta_W + \frac{1}{2},\ g_A = +\frac{1}{2} & \text{for } \nu_e \\ g_V = 2\sin^2\theta_W - \frac{1}{2},\ g_A = -\frac{1}{2} & \text{for } \nu_\mu, \nu\tau \end{cases} \tag{8.7}$$

where θ_W is the Weinberg angle ($\sin^2\theta_W = 0.2317$) [2]. We have applied the radiative correction [45] to the equation 8.5. If the corrections are considered, they contribute to reduce the cross

[2]The total cross section is given:

$$\begin{aligned} \sigma_{total} &= \int_0^{T_{max}} \frac{d\sigma}{dT_e} dT_e \\ &= \frac{G_F^2 m_e}{2\pi}\left[A_0 T_{max} + B_0\frac{E_\nu}{3}\left\{1 - \left(1 - \frac{T_{max}}{E_\nu}\right)^3\right\} + C_0\frac{m_e T_{max}^2}{2E_\nu^2}\right] \end{aligned} \tag{8.8}$$

where

$$T_{max} = \frac{E_\nu}{1 + \frac{m_e}{2E_\nu}} \tag{8.9}$$

(see figure 8.3-(a)) For electron neutrino, the total cross section is

1) $\nu_e\, e^- \rightarrow \nu_e\, e^-$

$$\sigma_{\nu_e\, e^- \rightarrow \nu_e\, e^-} = 9.478 \times 10^{-44}\ \frac{E_\nu(MeV)}{10(MeV)}\ \ (cm^2) \tag{8.10}$$

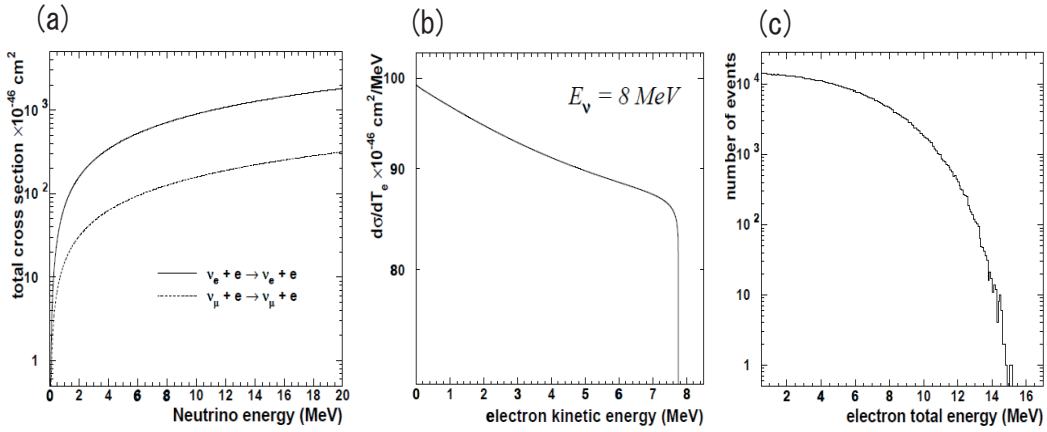

Figure 8.3: (a)$\nu - e$ total cross section,(b)differential cross section, (c) total recoil energy for ^{8}B solar neutrino.

section by $\sim 2\%$ for the ^8B energy region [45]. The recoil electron energy distribution is then calculated as:

$$F(T_e)dT_e = \left\{ \int_0^{E_{\nu,max}} \frac{d\sigma_{\nu e}(E_\nu, T_e)}{dT_e} \phi(E_\nu) dE_\nu \right\} dT_e \tag{8.14}$$

where $\phi(E_\nu)$ is the solar neutrino flux as a function of neutrino energy. Figure 8.3-(c) shows the energy distribution of the recoil electron for ^{8}B solar neutrinos.

In the second step, in order to take into account the detector response in the observed energy distribution prediction, we actually carry out the full detector simulation. In that simulation, electrons which obey the recoil energy distribution are generated, and the real run time is also simulated so that the solar neutrino MC events can be directly compared with the data for the time variation or the day-night asymmetry study.

Finally, the same reconstruction tools and reduction steps are applied to the solar neutrino MC events, and the MC final sample is made. The expected fraction in each energy bin, Y_i is obtained from the energy distribution of the solar neutrino MC final sample. Figure 8.4 shows the predicted energy distribution of the MC final sample.

For muon and tau neutrinos, the total cross section is

2) $\nu_{\mu,\tau}\, e^- \;\rightarrow\; \nu_{\mu,\tau}\, e^-$

$$\sigma_{\nu_{\mu,\tau}\, e^- \rightarrow \nu_{\mu,\tau}\, e^-} \;=\; 1.559 \times 10^{-44}\, \frac{E_\nu(MeV)}{10(MeV)} \quad (cm^2) \tag{8.11}$$

which is about 1/6 smaller than that of electron neutrino. The scattering angle is determined by kinematics, such as:

$$\cos\theta = \frac{1 + \frac{m_e}{E_\nu}}{\sqrt{1 + \frac{2m_e}{T_e}}} \tag{8.12}$$

in case of $m_e \ll T_e$

$$\cos\theta > 1 - \frac{m_e}{T_e} \tag{8.13}$$

which shows a strong correlation between the incident neutrino direction scattering angle of the recoil electron.

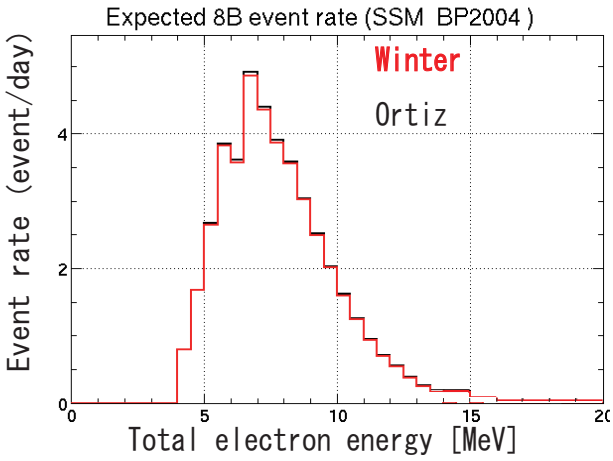

Figure 8.4: Energy spectrum of the solar neutrino MC final sample. The ^8B flux from BP04 SSM and Winter spectrum is used for red histogram and Ortiz spectrum is used for black histogram. The reduction efficiency in Figure 7.21 is considered. They agree within 5%.

Chapter 9

Systematic Uncertainties

9.1 Energy scale

In order to study how the energy scale systematic uncertainty (0.53%) affect to the flux value, the difference of the Y_i is obtained first. By changing the energy of each solar ν MC event by + or - 0.53% after the energy reconstruction, Y_i^{scale+} and Y_i^{scale-} are calculated. Using the Y_i^{scale+} and Y_i^{scale-}, the solar angle fittings are carried out. Then it turns out that the 0.53% scale shift makes $\pm$1.4% difference on the total flux in the 5.0-20.0 MeV electron total energy region.

For the day-night asymmetry study, I only take into account the angular dependence of energy scale uncertainty (0.25%) because the other systematic uncertainties of energy scale would be canceled out in the calculation of the asymmetry factor $((\Phi_D - \Phi_N)/0.5(\Phi_D + \Phi_N))$. In the same way, Y_i^{DN+} and Y_i^{DN-} are calculated with + or - 0.25% scale shift. As the result of the solar angle fittings, the systematic uncertainty of the day-night asymmetry is estimated as $\pm$1.3% in the 5.0-20MeV region.

Since the water transparency varies in time, the energy scale uncertainty depending on the water transparency (0.21%) should be contributed to the uncertainty to the seasonal study. It is estimated as $\pm$1.3%.

9.2 Energy resolution

In order to estimate the effect of the systematic uncertainty of the energy resolution ($\pm$2.5%) on the total flux, the prediction of observed energy spectrum is obtained not from the full detector simulation but from the calculation:

$$\mathcal{F}(E_{obs}) = \left\{ \int_0^{E_{max}} F(E_e) R(E_e, E_{obs}) dE_e \right\} dE_{obs} \tag{9.1}$$

where $E_{obs}, \mathcal{F}(E_{obs})$ are observed energy and the calculated observed energy spectrum, E_e is total energy of recoil electron, and $F(E_e)$ is the recoil energy spectrum calculated in equation 8.14. $R(E_e, E_{obs})$ is the detector response function:

$$R(E_e, E_{obs}) = \frac{1}{\sqrt{2\pi\sigma(E_e)^2}} \exp\left(-\frac{(E_e - E_{obs})^2}{\sigma(E_e)^2} \right) \tag{9.2}$$

where $\sigma(E_e)$ is the energy resolution function given by Equation 6.7. Then, the effect of the energy resolution systematic uncertainty on the observed energy is calculated by replacing $\sigma(E)$ with $\sigma^+(E) = \sigma(E)(1 + 0.025)$ or $\sigma^-(E) = \sigma(E)(1 - 0.025)$ to get $\mathcal{F}^+(E_{obs})$ or $\mathcal{F}^-(E_{obs})$, respectively. Finally, the ratio of $\mathcal{F}^{+(\text{or -})}$ to the original $\mathcal{F}$:

$$w_{eres}^{+(\text{or -})}(E_{obs}) = \frac{\mathcal{F}^{+(\text{or -})}(E_{obs})}{\mathcal{F}(E_{obs})} \tag{9.3}$$

is used as a weight for a each solar neutrino MC event, then the Y_i^{eres+} and Y_i^{eres-} are obtained. Using the Y_i^{eres+} and Y_i^{eres-}, the solar angle fittings are carried out. As the result, $\pm 0.12\%$ uncertainty on the total flux in 5-20MeV energy region is estimated from the 2.5% energy resolution uncertainty.

9.3 ^{8}B spectrum

Winter et.al. calculate ^{8}B spectrum from a very precise measurement of spectrum of ^{8}Be α decay [19]. The uncertainty of the ^{8}B calculation is taken from the paper which include both experimental and theoretical uncertainties. To estimate the effect of this uncertainty, the original spectrum $\phi(E_\nu)$ is changed by $\pm$ uncertainty, then $F^{^8B+(\text{or-})}$ is made by equation 8.14. By using the $F^{^8B+(\text{or-})}$ to Equation 9.1, $Y_i^{^8B+}$ and $Y_i^{^8B-}$ are made in the same way as Y_i^{eres+} and Y_i^{eres-}. After the solar angle fitting, the systematic uncertainty due to the ^8B shape is estimated as $\pm 0.2\%$ for the Winter ^{8}B spectrum. For the Ortiz ^{8}B spectrum, the same method in [20] is used, then the estimated as $^{+1.1}_{-1.0}\%$.

9.4 Angular resolution

In the same way as energy scale, Y_i^{ang+} and Y_i^{ang-} are made by artificially shifting the reconstructed direction of the solar neutrino MC events. The shifted direction is calculated as the reconstructed direction $\pm$ the systematic uncertainty of angular resolution (section 6.9) with respect to the generated direction of the recoil electron. After the solar angle fitting with Y_i^{ang+} and Y_i^{ang-}, the systematic uncertainty due to the uncertainty of angular resolution is estimated as $\pm 0.7\%$ on the total flux in 5.0-20MeV region.

9.5 Vertex shift

The vertex shift makes the systematic uncertainty of the fiducial volume. To estimate the total flux uncertainty due to the vertex shift, The reconstructed vertex positions of the solar neutrino MC events are artificially shifted toward outward of the detector. Then, it is estimated how many fraction of events are rejected by the fiducial volume cut due to the shift. As the result, 0.54% of the MC events are rejected and this contributes to the total flux systematic uncertainty.

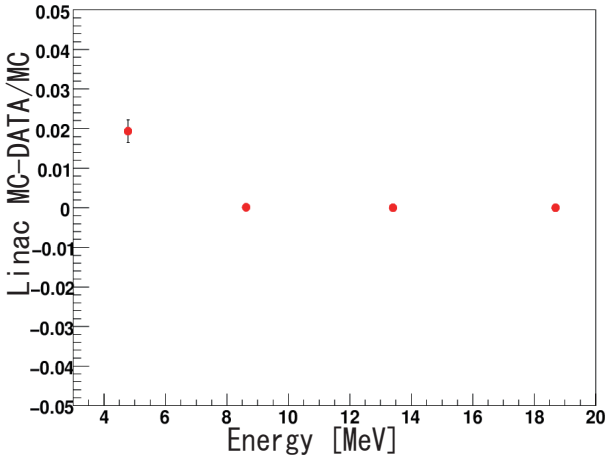

Figure 9.1: The difference of the ovaQ cut efficiency (MC-DATA)/MC of LINAC.

9.6 Reduction

9.6.1 ovaQ cut

Figure 9.1 shows the difference of the efficiency of ovaQ cut using the LINAC data and MC. To estimate the systematic uncertainty of the total flux due to the ovaQ cut, this energy dependence of the efficiency is taken into account. As the result, ±0.4% uncertainty to the total flux in 5.0-20MeV energy region is found.

9.6.2 Hit pattern cut

Figure 9.2 shows the difference of the inefficiency of the hit pattern cut using the LINAC data and MC. As seen in the figure, the efficiency difference between data and MC agree within 0.25%. This maximum discrepancy 0.25% is taken as the uncertainty to the total flux, conservatively.

9.6.3 Second vertex cut

The reconstructed vertex shift using the second fitter is also taken into account to estimate the systematic uncertainty on the flux. The estimation is done in the same way as the BONSAI vertex fitter, resulting 0.45% of uncertainty should contribute to the total flux.

9.7 Spallation cut

The same uncertainties as SK-I [20] is taken in this thesis. This is because the origin of the systematic uncertainty of spallation cut is mainly due to the characteristics of the muon such as rate, energy, arrival direction, and thus, the uncertainly should not depend on each phases of the experiment. The estimated valuses are 0.2% on the total flux in 5.0-20MeV region and 0.1 % for the time dependence part.

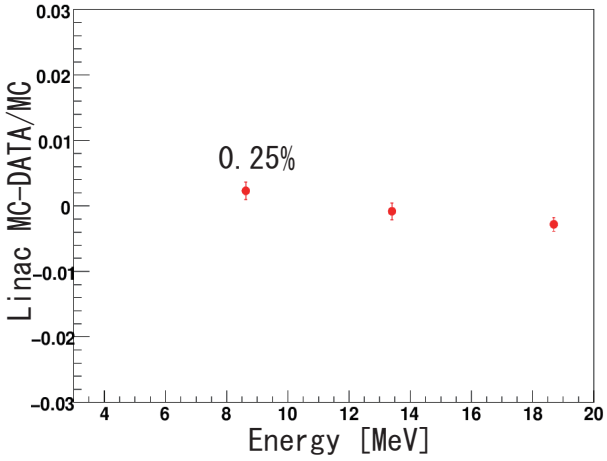

Figure 9.2: The difference of hit pattern cut efficiency (MC-DATA)/MC of LINAC.

9.8 Gamma ray cut

The vertex shift and the difference in the angular resolution measured by LINAC make some bias to the gamma cut efficiency. To estimate the effect, first, the reconstructed vertex and direction of solar neutrino MC events are shifted with the difference of the vertex and angular resolution systematic uncertainties between data and MC as shown in Figure 9.3. Second, the gamma cut efficiencies of the shifted MC sample and the original MC sample are compared. Then, the systematic uncertainty due to the gamma cut is estimated as ±0.25% for the total flux, and ±0.2% for the day-night asymmetry. For the uncertainly of spectrum, ±0.1% uncertainty is estimated.

9.9 Background shape

The systematic uncertainty due to the background shape prediction is estimated. As in the section 8.1, the solar angle distribution is fitted with the non-flat background shape. To get the non-flat background shape, not only the distribution of z-direction but also the distribution of phi direction is fitted. To estimate the systematic uncertainty, the background shape assuming flat ϕ distribution is made and then the solar angle fitting is carried out with the background shape. The difference of the fitting results between these two types of background shapes are taken as the systematic uncertainty, which is 0.07% for the total flux and 0.4% for the day-night asymmetry.

9.10 Signal extraction method

To check how the signal extraction method biases the flux value, the solar angle fit is applied to dummy data which have known number of signal and background events. As the result, ±0.7% difference is found between the input and the output number of signal events for the total flux, and ±2% difference is found especially in the $5.0 < E < 5.5$MeV region.

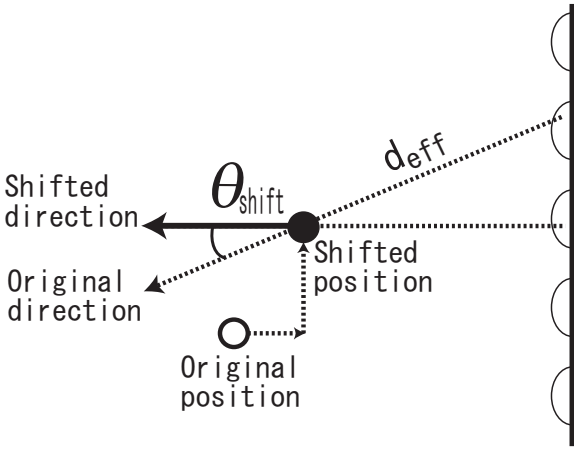

Figure 9.3: Gamma cut systematic uncertainty check. the amount of vertex shift and direction shift are measured by calibration. The shifted direction is determined based on the original direction and reconstructed direction.

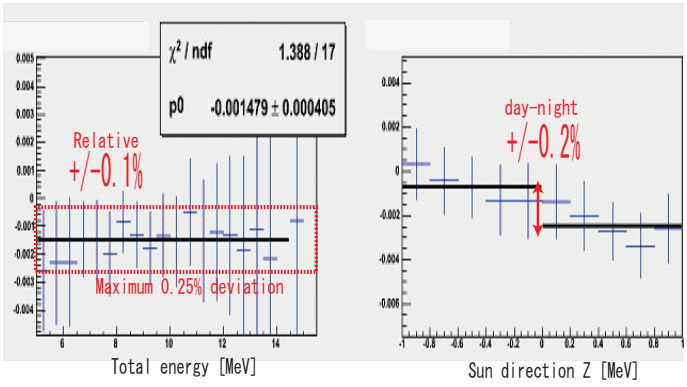

Figure 9.4: Gamma cut systematic uncertainty check. difference of inefficiency before and after the vertex and direction shift as a function of energy (left) and z component of sun direction (right)

9.11 Cross section

The systematic uncertainty due to cross section is estimated from [45], in which cross section parameters ρ, κ has 1σ theoretical uncertainty. Shifting the parameters by $\pm 1\sigma$ uncertainty gives the difference in cross section which corresponds to $\pm 0.5\%$ uncertainty on the total flux.

9.12 Further quality cut for the lowest energy region

Clustering hits cut

Using DT data and MC simulation at the position (x=-12m,y=0m,z=0m), the difference of cut efficiency between DT data and MC events is estimated as 2%. Assuming the all fiducial volume and energy region of solar neutrino signal, this difference corresponds to 0.5% uncertainty on the total flux in the 5.0-20MeV region. 2% is assigned to the spectral shape uncertainty in the 5.0 to 6.5 MeV bins.

Tighter fiducial volume cut

Assuming the vertex shift, the tighter fiducial volume cut makes 0.9% uncertainty on the flux in 5.0 to 5.5 MeV region. This is negligible for the total fulx uncertainty, but is assigned to the spectral shape uncertainty in the 5-5.5 energy bin.

9.13 Summary of systematic uncertainty

9.13.1 Flux,time variation,Day-Night asymmetry

The systematic uncertainty of total flux, time variation and day-night asymmetry is summarized in the Table 9.1 In this thesis, the systematic uncertainty on the total flux is estimated as 2.3% when we use Ortiz ^{8}B spectrum. This is about two thirds of the corresponding SK-I value. For comparison, SK-I systematic uncertainty is shown in Table 9.2. The main contributions for the improvement are vertex shift, angular resolution, and reduction step which are reestimated in this thesis.

9.13.2 Spectrum

The systematic uncertainty of the spectral shape consists of two components.

Energy correlated

The energy correlated systematic uncertainties are given from Equation 9.1 with artificially shifted energy scale, energy resolution and ^8B spectrum. The results of the calculations are shown in Figure 9.5 These correlations are taken into account in the oscillation analysis.

Energy uncorrelated

The energy uncorrelated energy spectral uncertainties are listed in Table 9.3 In this table, the common offset of the uncertainties are omitted in order to estimate the effect on the energy spectral shape.

Source	Flux	Time variation	Day/Night
Energy scale	±1.4%	±1.3%	±1.3%
Energy resolution	±0.2%		
^{8}B spec.	±0.2/1.0%		
Trig. eff.	±0.5%	±0.1%	
Ang. resolution	±0.67%		
Vertex shift	±0.54%		
Reduction			
ovaQ	±0.4%		
Hit pattern cut	±0.25%		
Second vertex	±0.45%		
Spallation	±0.2%	±0.1%	±0.1%
Gamma-ray cut	±0.25%		±0.2%
Cluster hit cut	±0.5%		
Background shape	±0.1%		±0.4%
Signal ext. method	±0.7%		
Cross section	±0.5%		
Total	±2.1/2.3%	±1.3%	±1.4%

Table 9.1: Summary of the total systematic uncertainty. The total value 2.1% is for Winter ^{8}B spectrum and 2.3% is for Ortiz

Source	Flux	Time variation	Day/Night
Energy scale, resolution	±1.6%	$^{+1.2}_{-1.1}$%	$^{+1.2}_{-1.1}$%
^{8}B spec.	±1.0%		
Ang. resolution	±1.2%		
Vertex shift	±1.3%		
Reduction	$^{+2.1}_{-1.6}$%		
Spallation	±0.2%	±0.1%	±0.1%
Gamma-ray cut	±0.5%	±0.25%	
Background shape	±0.1%		±0.4%
Cross section	±0.5%		
Livetime calculation	±0.1%	±0.1%	±0.1%
Total	$^{+3.5}_{-3.2}$%	±1.3%	$^{+1.3}_{-1.2}$%

Table 9.2: Summary of the total systematic uncertainty in SK-I.

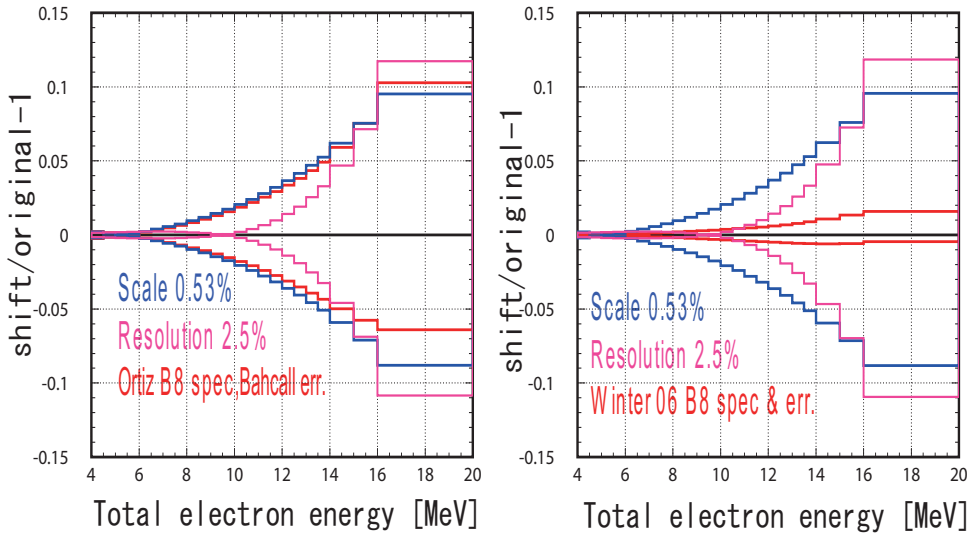

Figure 9.5: Energy correlated systematic uncertainties for Ortiz (left) and Winter (right) ^{8}B spectrum.

Energy(MeV)	5-5.5	5.5-6	6-6.5	6.5-7	7-7.5	7.5-20
Trig eff	±2.4%	±0.9%	±0.1%	-	-	-
ovaQ	±2.%	±1.75%	±1.5%	±1.25%	±1.0%	-
Hit pat.	-	-	-	±0.25%	±0.25%	±0.25%
Cluster cut	±2.%	±2.%	±2.%	-	-	-
Gamma Cut	±0.1%	±0.1%	±0.1%	±0.1%	±0.1%	±0.1%
Vertex shift	±0.5%	±0.1%	±0.1%	±0.1%	±0.1%	±0.1%
BG shape	±0.2%	±0.8%	±0.2%	±0.2%	±0.2%	±0.2%
Sig.Ext.	±2.1%	±0.7%	±0.7%	±0.7%	±0.7%	±0.7%
Cross section	±0.2%	±0.2%	±0.2%	±0.2%	±0.2%	±0.2%
Total	±4.3%	±3.0%	±2.6%	±1.5%	±1.3%	±0.8%

Table 9.3: Energy uncorrelated systematic uncertainty on the spectrum shape.

Chapter 10

Result

The results of solar neutrino signal fitting are shown in this chapter.

Total Flux and time variation

Figure 10.1 shows the solar angle distribution of the final sample. The energy range of this sample is 5.0 to 20.0MeV. The fitted signal and background shape are also plotted in the figure. The observed total number of solar neutrino events is $8098^{+132}_{-131}(stat.) \pm 186(sys.)$, the resulting flux is

$$2.28 \pm 0.04(stat.) \pm 0.05(sys.) \ \times 10^6 \mathrm{cm}^{-2}\mathrm{sec}^{-1} \tag{10.1}$$

where Ortiz ^{8}B neutrino spectrum is used, and thus the total systematic uncertainty is $\pm 2.3\%$. This value is consistent with the the flux values obtained in SK-I and II:

$$\begin{aligned} 2.35 \pm 0.02(stat.) \pm 0.08(sys.) \ \times 10^6 \mathrm{cm}^{-2}\mathrm{sec}^{-1} \qquad \text{SK-I} \\ 2.38 \pm 0.05(stat.)^{+0.16}_{-0.16}(sys.) \ \times 10^6 \mathrm{cm}^{-2}\mathrm{sec}^{-1} \qquad \text{SK-II} \end{aligned}$$

In this thesis, since the angular resolution becomes better than SK-I due to the new fitter, the peak at $\cos\theta_{sum} = 1$ is gotten higher resulting in a better S/N ratio.

If the Winter spectrum is used instead of Ortiz's one, the flux value in SK-III is found to be

$$2.31 \pm 0.04(stat.) \pm 0.05(sys.) \ \times 10^6 \mathrm{cm}^{-2}\mathrm{sec}^{-1} \tag{10.2}$$

This difference between Equation 10.1 and 10.2 is expected from the difference between the two ^{8}B spectrum shapes in Figure 2.8

The day time and night time fluxes are defined by

$$\cos\Theta_z \ \leq \ 0 \qquad Day \tag{10.3}$$

$$\cos\Theta_z \ > \ 0 \qquad Night \tag{10.4}$$

where Θ_z is the solar zenith angle (see Figure 8.1). Figure 10.2 shows the angular distribution in day-time and night-time. The observed fluxes are

$$\begin{aligned} \Phi_{day} &= 2.22 \pm 0.05(stat.) \ \pm 0.05(sys.) \times 10^6 \mathrm{cm}^{-2}\mathrm{sec}^{-1} \\ \Phi_{nignt} &= 2.35 \pm 0.05(stat.) \ \pm 0.05(sys.) \times 10^6 \mathrm{cm}^{-2}\mathrm{sec}^{-1} \end{aligned} \tag{10.5}$$

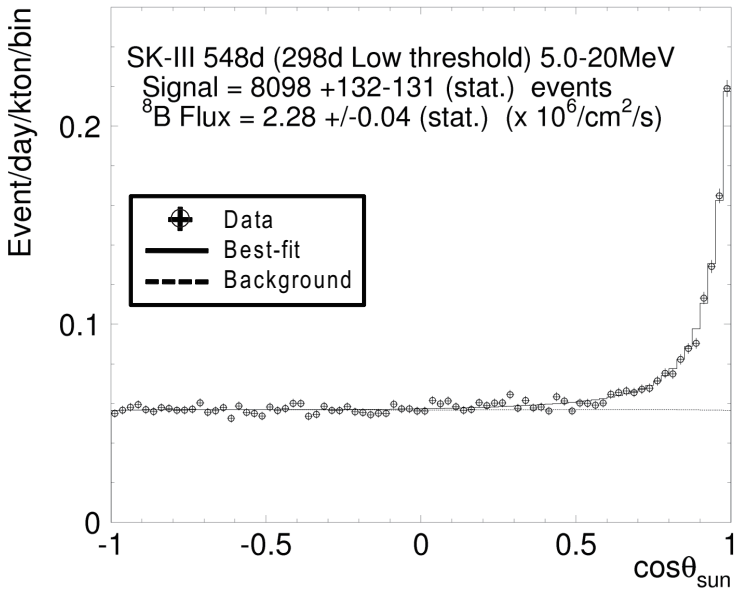

Figure 10.1: Angular distribution of final sample 5-20MeV.

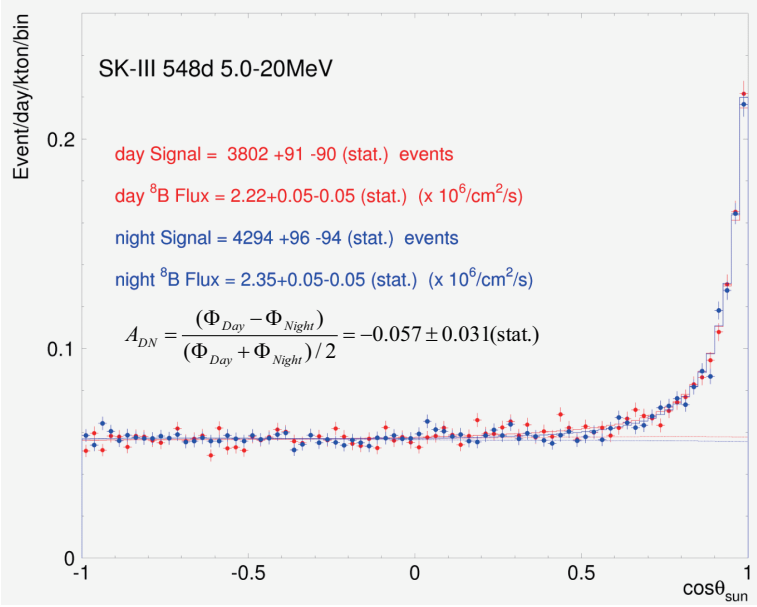

Figure 10.2: Angular distribution on day (red) and night (blue) time.

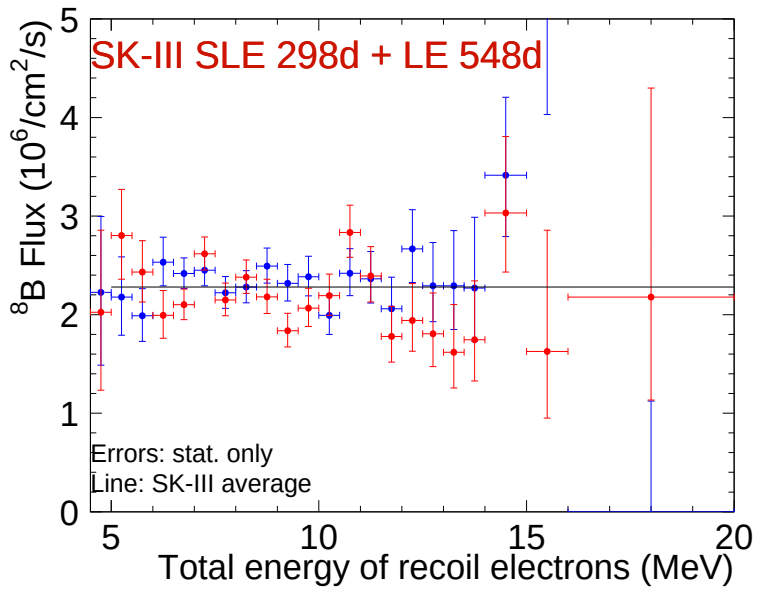

Figure 10.3: Energy spectrum of day(red) and night(blue). Black line shows SK-III average flux.

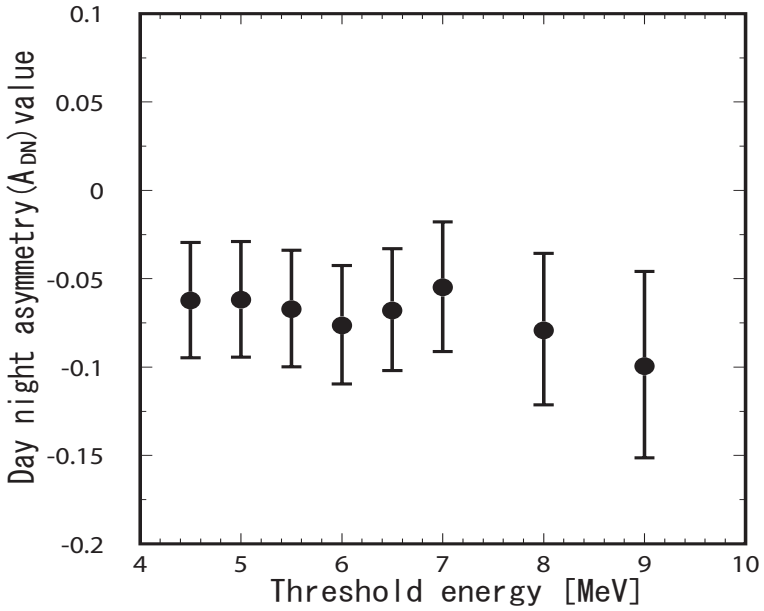

Figure 10.4: Day night asymmetry values as a function of energy threshold. The upper limit of energy is 20MeV.

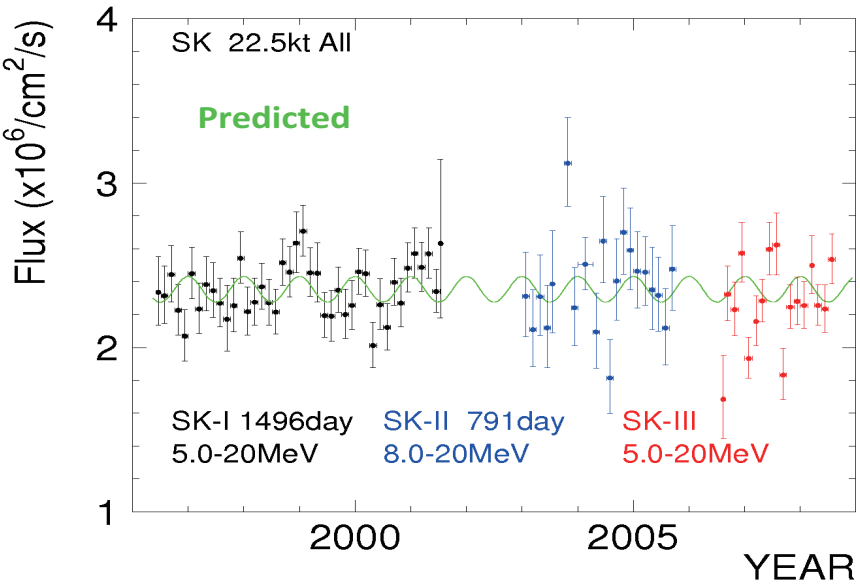

Figure 10.5: Time variation of observed flux. Green line shows the predicted value

The day-night asymmetry A_{DN} is defined by

$$\begin{aligned} A_{DN} &= \frac{\Phi_{day} - \Phi_{night}}{\frac{1}{2}(\Phi_{day} + \Phi_{night})} \\ &= -0.057 \pm 0.031(stat.) \pm 0.013(sys) \end{aligned} \tag{10.6}$$

The A_{DN} in SK-I and II are:

$$\begin{aligned} A_{DN} &= -0.021 \pm 0.020(stat.)\ ^{+0.013}_{-0.012}(sys.) \qquad SK-I \\ A_{DN} &= -0.63 \pm 0.020(stat.)\ \pm 0.037(sys.) \qquad SK-II \end{aligned} \tag{10.7}$$

The A_{DN} in SK-III is about 1.7σ away from 0, and the expected value from the oscillation parameters in favored Large Mixing Angle (LMA) solution is -1.5% [20]. To study this difference between A_{DN} and 0, A_{DN} values in the different energy regions are calculated, and it is confirmed that those A_{DN} values in the different energy regions are consistent with the 5-20MeV value (see Figure **??** and 10.4). Further more, using the event sample before spallation cut above 6.5MeV (most events in a such sample are due to a single β ray which is emitted by spallation products), it is also confirmed that energy scale of upward going events and that of downward going events are consistent within the assigned systematic uncertainty ($\pm$0.25%). Thus, any systematic bias has not been found to explain the large A_{DN} value so far.

Figure 10.5 shows the time variation of observed solar neutrino flux. Each horizontal bin corresponds to 45 days. The correction of the elliptical orbit of the Earth is not taken into account in this analysis. The fluctuation in SK-III seems large, but it would be statistically consistent with the average value obtained by SK-I. Figure 10.6 shows the seasonal variation of the solar neutrino flux. The χ^2 value is 13.6(d.o.f. = 7) which corresponds to 5.95% probability. (Cf. The χ^2 value of SK-I is 4.7(d.o.f = 7) which corresponds to 69.9% probability.) Combining

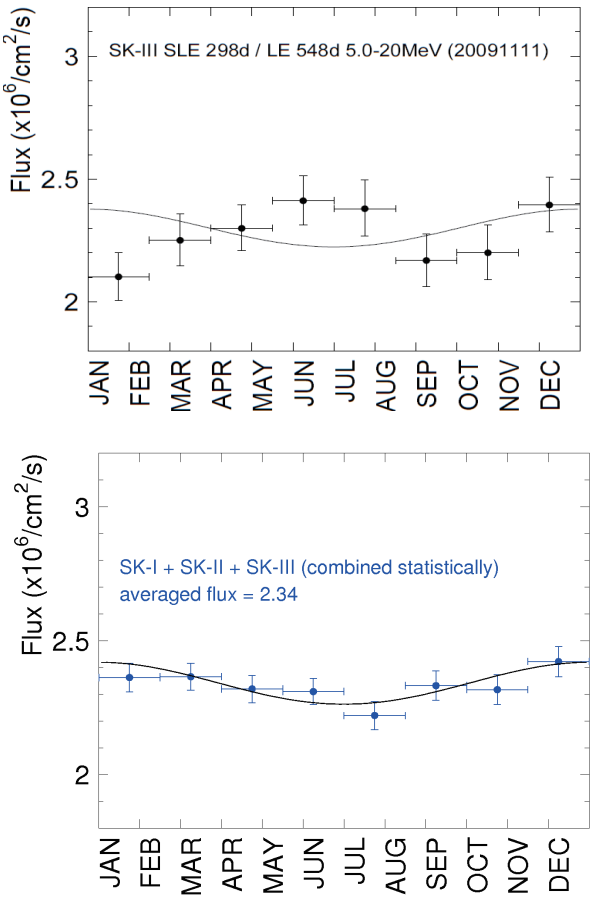

Figure 10.6: Seasonal variation of observed flux. Solid line shows the predicted value from the elliptical orbit of the Earth.

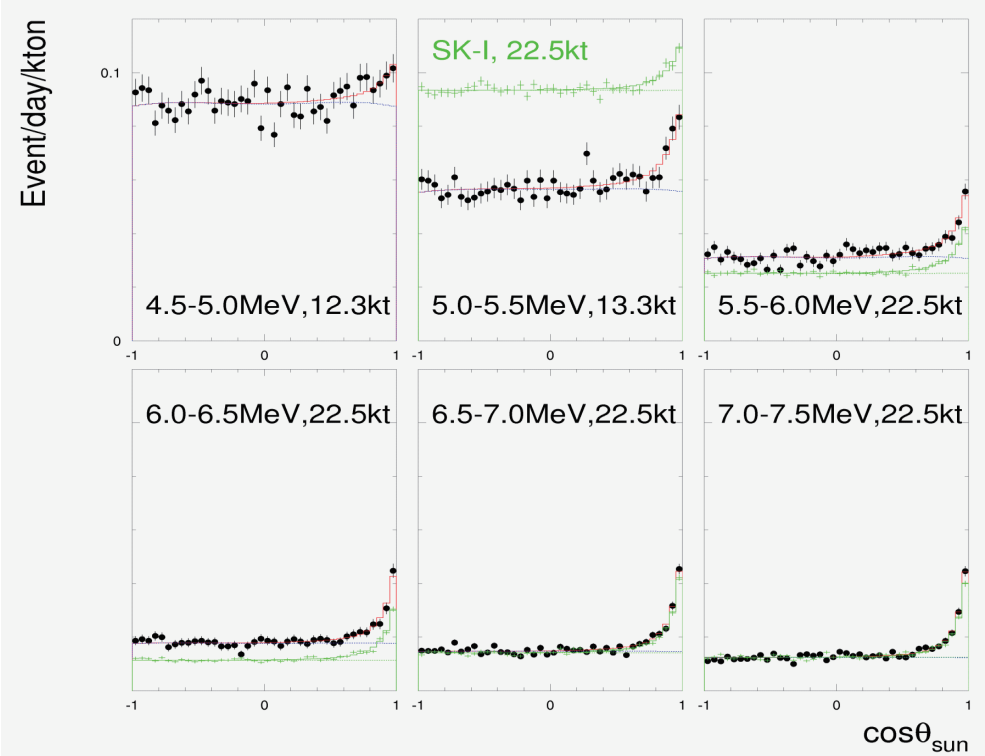

Figure 10.7: Solar angle distributions of different energy regions from 4.5-7.5 MeV.

SK-I,II,and III statistically, the χ^2 value is 3.6(d.o.f.=7) which corresponds to 89% probability. Thus, seasonal variation in SK-III is statistically consistent with SK-I.

Figure 10.7 shows the solar angle distribution in the different energy regions. The solar angle distribution in the 4.5-5MeV region is shown in the upper left plot. The background level is almost the same as that of SK-I 5-5.5 MeV region (green histogram in middle top plot). The solar angle fitting result looks good, and the fitted number of signal events and the flux in the 4.5-5MeV region are

$$4.5 - 5MeV: \qquad 232. \pm 59.event \tag{10.8}$$

and

$$4.5 - 5MeV: \qquad 2.14^{+0.56}_{-0.54}(stat.) \times 10^6 \mathrm{cm}^{-2}\mathrm{sec}^{-1} \tag{10.9}$$

This flux value is consistent with the 5-20MeV flux. Since the trigger efficiency in the SLE1 period is not clear, the systematic uncertainty for this energy region was not estimated.

Energy spectrum

Figure 10.8 shows the expected and measured electron total energy spectrum. The expected rate is calculated by the detector simulation which uses BP04 SSM. The solid line is expected spectrum by SSM. The summary of observed and expected event rate is summarized in Table 10.1. Figure 10.9 shows the ratio of observed energy spectrum to the SSM prediction. As shown

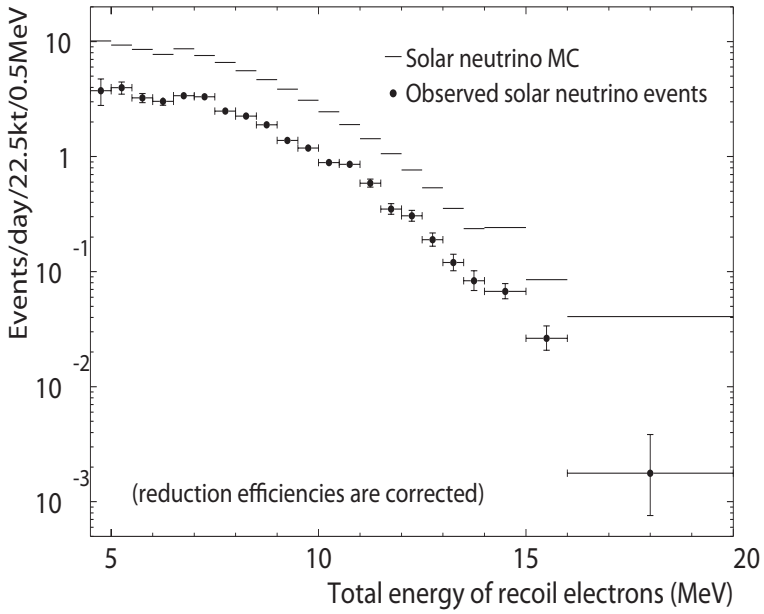

Figure 10.8: Energy spectrum of the solar neutrino signal. Horizontal axis is the total energy of recoil electrons. Vertical is the event rate.

in the figure, no significant up-turn was not observed. And the average value is consistent with SK-I.

Ennergy (MeV)	ALL	DAY	NIGHT	^{8}B	hep
$5.0 - 5.5$	$64.4^{+8.0}_{-7.7}$	$73.2^{+12.2}_{-11.6}$	$56.9^{+10.6}_{-10.1}$	150.9	0.260
$5.5 - 6.0$	$52.6^{+5.0}_{-4.8}$	$58.1^{+7.6}_{-7.2}$	$47.6^{+6.6}_{-6.2}$	138.2	0.250
$6.0 - 6.5$	$49.1^{+3.8}_{-3.7}$	$43.2^{+5.4}_{-5.1}$	$54.9^{+5.5}_{-5.2}$	125.3	0.241
$6.5 - 7.0$	$55.0^{+2.7}_{-2.6}$	$51.0^{+3.9}_{-3.7}$	$58.7^{+3.8}_{-3.7}$	140.4	0.289
$7.0 - 7.5$	$53.7^{+2.5}_{-2.4}$	$55.5^{+3.6}_{-3.5}$	$52.0^{+3.5}_{-3.3}$	122.6	0.271
$7.5 - 8.0$	$40.3^{+2.2}_{-2.1}$	$39.6^{+3.1}_{-3.0}$	$41.0^{+3.1}_{-2.9}$	106.5	0.257
$8.0 - 8.5$	$36.5^{+1.9}_{-1.8}$	$37.3^{+2.7}_{-2.6}$	$35.7^{+2.6}_{-2.5}$	90.5	0.240
$8.5 - 9.0$	$30.6^{+1.7}_{-1.6}$	$28.6^{+2.4}_{-2.2}$	$32.7^{+2.4}_{-2.3}$	75.6	0.223
$9.0 - 9.5$	$22.4^{+1.4}_{-1.3}$	$19.8^{+1.9}_{-1.8}$	$25.0^{+2.1}_{-1.9}$	62.3	0.205
$9.5 - 10.0$	$19.3^{+1.2}_{-1.2}$	$17.9^{+1.8}_{-1.6}$	$20.7^{+1.8}_{-1.7}$	50.0	0.186
$10.0 - 10.5$	$14.4^{+1.0}_{-1.0}$	$15.1^{+1.5}_{-1.4}$	$13.7^{+1.5}_{-1.3}$	39.6	0.169
$10.5 - 11.0$	$13.9^{+1.0}_{-0.9}$	$15.1^{+1.5}_{-1.3}$	$12.9^{+1.3}_{-1.2}$	30.6	0.151
$11.0 - 11.5$	$9.54^{+0.80}_{-0.74}$	$9.59^{+1.20}_{-1.06}$	$9.47^{+1.11}_{-0.99}$	23.07	0.134
$11.5 - 12.0$	$5.69^{+0.64}_{-0.58}$	$5.28^{+0.91}_{-0.77}$	$6.11^{+0.96}_{-0.82}$	17.07	0.118
$12.0 - 12.5$	$4.96^{+0.57}_{-0.51}$	$4.16^{+0.80}_{-0.67}$	$5.71^{+0.85}_{-0.73}$	12.30	0.102
$12.5 - 13.0$	$3.08^{+0.44}_{-0.38}$	$2.71^{+0.62}_{-0.50}$	$3.44^{+0.66}_{-0.54}$	8.60	0.088
$13.0 - 13.5$	$1.95^{+0.36}_{-0.30}$	$1.61^{+0.48}_{-0.36}$	$2.28^{+0.56}_{-0.44}$	5.68	0.074
$13.5 - 14.0$	$1.35^{+0.30}_{-0.24}$	$1.16^{+0.40}_{-0.28}$	$1.51^{+0.48}_{-0.36}$	3.78	0.062
$14.0 - 15.0$	$2.19^{+0.36}_{-0.31}$	$2.06^{+0.53}_{-0.41}$	$2.32^{+0.54}_{-0.42}$	3.84	0.092
$15.0 - 16.0$	$0.854^{+0.240}_{-0.180}$	$0.389^{+0.295}_{-0.162}$	$1.249^{+0.398}_{-0.284}$	1.326	0.059
$16.0 - 20.0$	$0.115^{+0.134}_{-0.066}$	$0.248^{+0.242}_{-0.119}$	$0.000^{+0.128}_{-0.415}$	0.592	0.068

Table 10.1: Observed and expected rates in each energy bin at 1AU. The unit of the rate is event/kton/year. The errors in the observed rate are statistical only. The reduction efficiencies are corrected, and the expected event rates are for the BP2004.

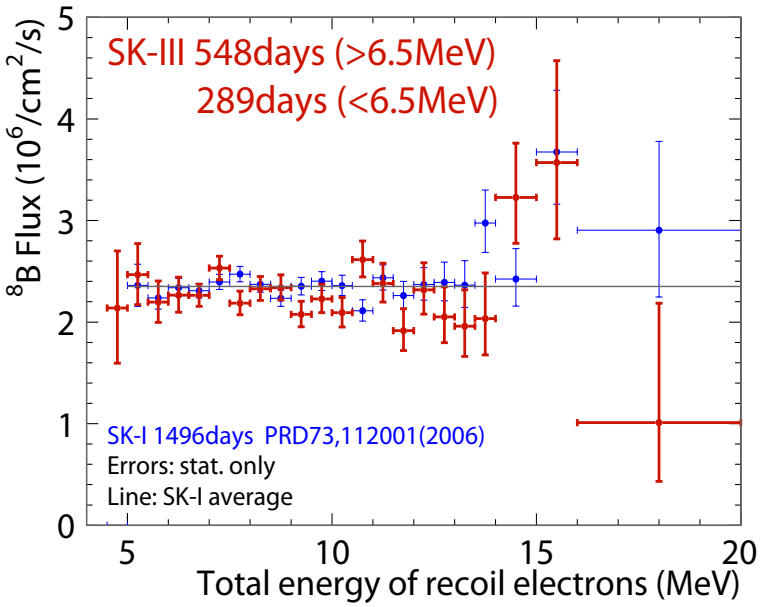

Figure 10.9: Energy spectrum of SK-I and III. Horizontal axis is the total energy of recoil electrons. Vertical is data/SSM$\times 5.79 \times 10^6 cm^{-2}s^{-1}$(^{8}B flux of BP2004).

Chapter 11

Oscillation Analysis

11.1 Spectrum fit

11.1.1 Spectrum shape prediction

The method to calculate the expected energy spectrum of the recoil electron by solar neutrino is following. Using the survival probability p_e in Equation 2.23, the neutrino interaction rate in the observed energy range E_{low} to E_{high} with the neutrino oscillation is written as

$$r_{osc} = \int_{E_{low}}^{E_{high}} dE \int_{E_\nu} dE_\nu \phi(E_\nu) \int_{E_e} dE_e R(E_e, E) \left(p_e S_e(E_\nu, E_e) + (1 - p_e) S_{\mu,\tau}(E_\nu, E_e)\right) \quad (11.1)$$

where $S_{e,\mu,\tau}(E_\nu, E_e)$ describe the probability of the elastic scattering of a $\nu_{e,x}$ of energy E_ν with an electron of recoil energy E_e. $R(E_e, E)$ is the detector response function given by the equation 9.2. $\phi(E_\nu)$ is the solar neutrino flux (^{8}B or *hep*) as a function of neutrino energy. For the null oscillation case, the rate r_{null} is given by setting $p_e = 1$.

As described in Section 2.3, the p_e consists of the Sun propagation part, p_1, and the Earth propagation part, p_{1e}. Since we do not know the path of the observed neutrino in the Sun, p_1 is obtained by averaging over the production points. On the other hand, for the earth part, if the event time and the position of the Sun and the detector at the time are given, a unique path of the observed neutrino can be calculated for an oscillation parameter set, $(\Delta m^2, \theta)$, and eventually, p_e is obtained as a function of neutrino energy (E_ν) and zenith angle of the Sun, $cz \equiv \cos\Theta_z$, $p_e(E_\nu, cz)$. The interaction rate with the neutrino oscillation in Equation 11.1 correspondingly has a form of $r_{osc}(E, cz)$.

In this analysis, cz of the night time ($0 < cz \leq 1$) is divided into 1000 bins and 1 bin is for day time ($-1 \leq cz \leq 0$). With this binning, the interaction rate of ^8B and *hep* neutrinos are

$$B^{osc}(E) = \sum_{j=1}^{1001} \frac{\tau(cz_j)}{\tau_{tot}} \cdot r_{osc}^{^8B}(E, cz_j) \quad (11.2)$$

$$H^{osc}(E) = \sum_{j=1}^{1001} \frac{\tau(cz_j)}{\tau_{tot}} \cdot r_{osc}^{hep}(E, cz_j) \quad (11.3)$$

where $\tau(cz_j)$ is the livetime in the j-th zenith angle bin which is obtained from the real data (see Figure 11.1), and τ_{tot} is the total livetime. The predicted rate of the i-th bin ($E_{low,i} <$

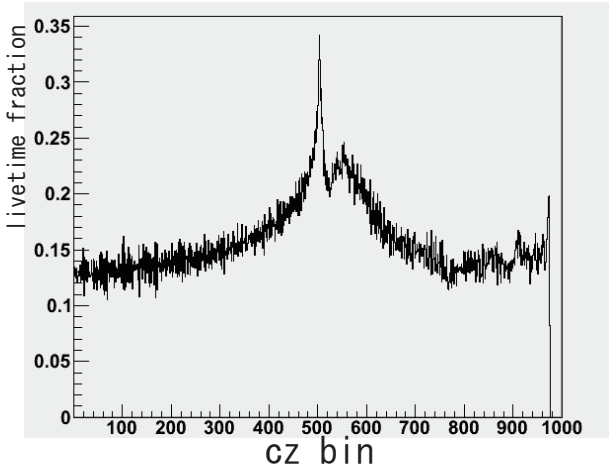

Figure 11.1: livetime fraction in each cz bin 1 to 1000. cz bin = 1 and 1000 correspond to cosΘ_z = -1 and 1, respectively.

$E < E_{high,i}$) is given as

$$B_i^{osc} = \int_{E_{low,i}}^{E_{high,i}} dE \cdot B^{osc}(E) \tag{11.4}$$

$$H_i^{osc} = \int_{E_{low,i}}^{E_{high,i}} dE \cdot H^{osc}(E) \tag{11.5}$$

11.1.2 Constructing χ^2

In this calculation, the 5.0MeV energy threshold is used. The definition of χ^2 is

$$\chi^2 = \sum_{i=2}^{Nbin} \frac{(d_i - (\beta b_i + \eta h_i) \times f(E_i, \delta_B, \delta_S, \delta_R))^2}{\sigma_i^2} + \delta_B^2 + \delta_S^2 + \delta_R^2 \tag{11.6}$$

where i is the energy bin as explained in Section 8.1. d_i, b_i, and h_i are ratios of the data and oscillated solar neutrino rate to the unoscillated SSM rate:

$$d_i = \frac{D_i}{B_i + H_i} \tag{11.7}$$

$$b_i = \frac{B_i^{osc}}{B_i + H_i} \tag{11.8}$$

$$h_i = \frac{H_i^{osc}}{B_i + H_i} \tag{11.9}$$

D_i is observed solar neutrino observed rate, and B_i and H_i are the expected rate without the neutrino oscillation, and β and η are free parameters to allow the arbitral fit of the total neutrino fluxes. f in Equation 11.6 is the energy shape factor:

$$f(E_i, \delta_B, \delta_S, \delta_R) = f_B(E_i, \delta_B) \times f_S(E_i, \delta_S) \times f_R(E_i, \delta_R) \tag{11.10}$$

where

$$f_x(E_i, \delta_x) = \frac{1}{1 + \delta_x \times \epsilon_x^{\pm}(E_i)}, \qquad (x = B, S, R) \tag{11.11}$$

and B, S, R denote the ^8B spectrum, energy scale, energy resolution, respectively. δ_x is the unitless parameter to scale the energy correlated uncertainty, $\epsilon_x^{\pm}(E_i)$ in Figure 9.5. The δ_x is varied until the χ^2 gives the minimum value with β_m and η_m. β_m and η_m are calculated analytically by setting the partial first derivative of χ^2 with respect to β and η to zero.

σ_i in equation 11.6 is combined statistical-systematic uncertainty, in which the energy uncorrelated systematic uncertainties are combined in quadrature with the energy spectrum's statistical uncertainties. To account for the total flux energy uncorrelated systematic uncertainty, Taylor expanding of χ^2 is carried out around the χ^2 minimum (χ^2_m) with:

$$\chi^2(\beta, \eta) = \chi^2_m(\beta_m, \eta_m) + \begin{pmatrix} \beta - \beta_m \\ \eta - \eta_m \end{pmatrix}^T C_0 \begin{pmatrix} \beta - \beta_m \\ \eta - \eta_m \end{pmatrix} \tag{11.12}$$

where C_0 is

$$C_0 = \sum_{i=2}^{N_{bin}} \begin{pmatrix} \frac{b_i^2}{\sigma_i^2} & \frac{b_i h_i}{\sigma_i^2} \\ \frac{b_i h_i}{\sigma_i^2} & \frac{h_i^2}{\sigma_i^2} \end{pmatrix} \tag{11.13}$$

Then C_0 is scaled by α_{sys} to add the total energy uncorrelated systematic uncertainty σ_{sys}. α_{sys} is defined as

$$\alpha_{sys} = \frac{\sigma_0^2}{\sigma_0^2 + \sigma_{sys}^2}, \qquad \text{where} \qquad \sigma_0^2 = \sum_{i=2}^{N_{bin}} \frac{1}{\sigma_i^2} \tag{11.14}$$

σ_{sys} is obtained as the total flux $\times$ (energy uncorrelated sys. on the total flux) / SSM flux, which is $2.28 \times \sqrt{0.023^2(total) - 0.014^2(escale) - 0.002^2(eres.) - 0.01^2(^8B)}/5.79 = 0.6\%$ for SK-III. Then, the χ^2 becomes

$$\chi^2_{\alpha,SK3}(\beta, \eta) = \chi^2_m(\beta_m, \eta_m) + \begin{pmatrix} \beta - \beta_m \\ \eta - \eta_m \end{pmatrix}^T \alpha_{sys} \cdot C_0 \begin{pmatrix} \beta - \beta_m \\ \eta - \eta_m \end{pmatrix} \tag{11.15}$$

The χ^2 for the energy spectrum shape is eventually expressed as: excluded

$$\chi^2_{specSK3}(\beta, \eta) = \mathrm{Min}(\chi^2_{\alpha,SK3}(\beta, \eta, \delta_B, \delta_S, \delta_R) + \delta_B^2 + \delta_S^2 + \delta_R^2) \tag{11.16}$$

where the number of fitting parameters is five; $\beta, \eta, \delta_B, \delta_S, \delta_R$. Inside of line is excluded. Figure 11.2-(a) shows the exclude region by the SK-III spectrum obtained from the Equation 11.16.

11.2 Time-Variation Analysis

In the time-variation analysis, 6.5MeV energy threshold is used. In order to take into account the time variation of the rate due to the matter effects of the Earth, the s_{ij} of Equation 8.1 is modified with a scaling function $r_i(t_j)/r_i^{ave}$. Here, t_j is the event time of the j-th event and $r_i(t_j)$ is the predicted time dependence (that is, cz dependence) of the expected oscillated solar

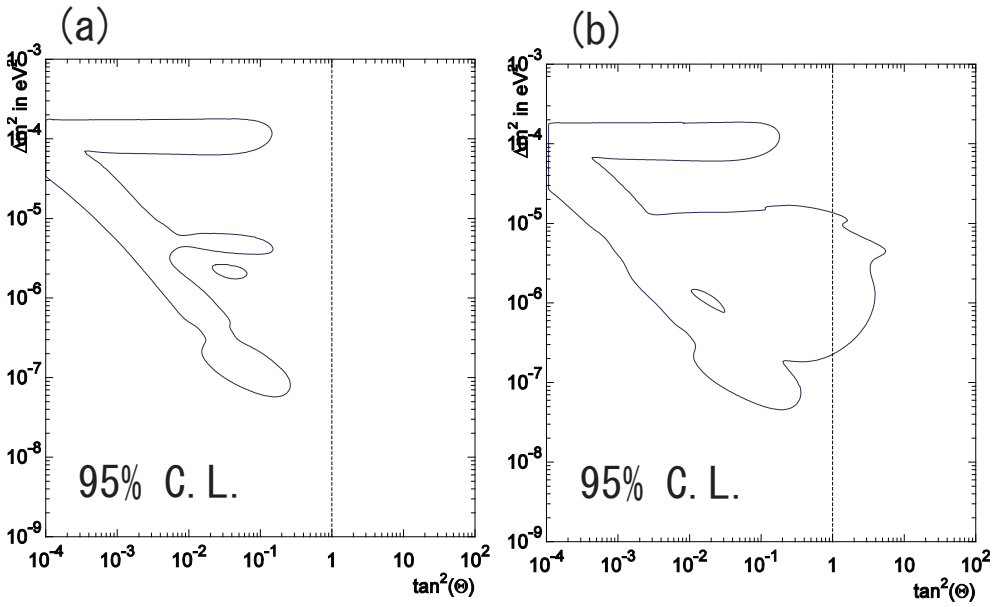

Figure 11.2: Excluded region only from the SK-III result (inside area of the line is excluded). (a) Spectral shape only, (b) Spectral shape and time variation

neutrino rate in energy bin i, and r_i^{ave} is the average of the oscillated rates over all the zenith angle bins. The likelihood is for the signal extraction (Equation 8.1) is modified as:

$$L_{t.v.SK3} = e^{-(\sum_i B_i + S)} \prod_{i=5}^{N_{bin}} \prod_{j=1}^{n_i} (B_i \cdot b_{ij} + S \cdot Y_i \cdot s_{ij} \frac{r_i(t_j)}{r_i^{ave}}) \tag{11.17}$$

The effect of the matter oscillation can be tested by comparing the likelihood $L_{t.v}$ with the original L ($r_i(t)/r_i^{ave} = 1$). In this calculation, the Y_i is now determined from the prediction of the oscillated spectrum. This spectrum is given by using the ^{8}B and hep neutrino fluxes and energy spectral shape factors from the $\chi^2_{specSK3}$ fit. The combination of $\chi^2_{specSK3}$ and the likelihood of the time-variation is done by converting the likelihood value in terms of χ^2. That is:

$$\chi^2_{SK3} = \chi^2_{specSK3} + \Delta\chi^2_{t.v.SK3} \tag{11.18}$$

where

$$\Delta\chi^2_{t.v.SK3} = -2(\log L_{t.v.SK3} - \log L). \tag{11.19}$$

Figure 11.2-(b) shows the excluded region by the spectral shape and time variation only from SK-III data.

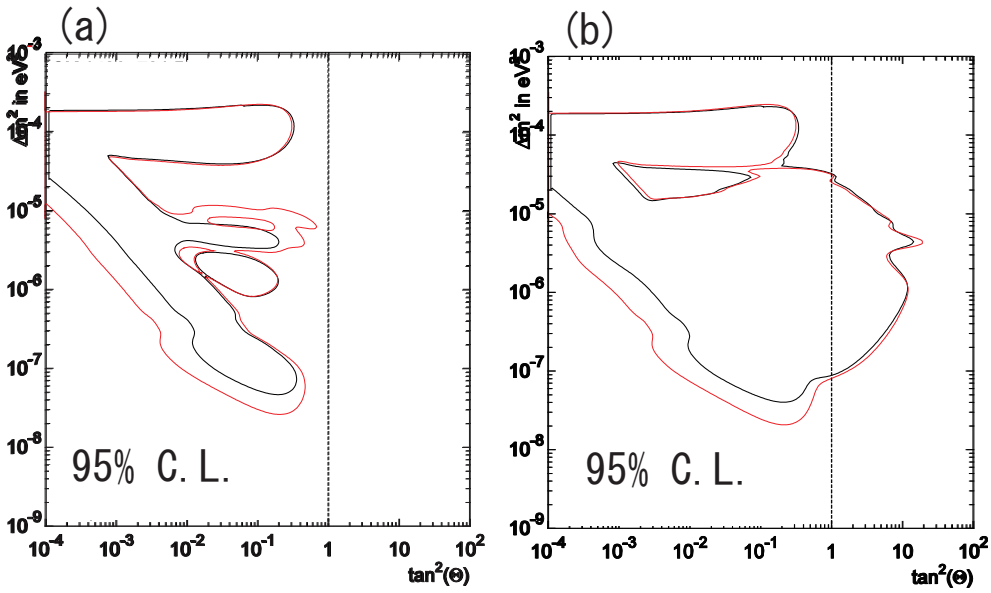

Figure 11.3: Excluded region from the SK combined analysis (inside area of the line is excluded). Black shows only SK-I and II, Red shows SK-I,II and III. (a) Spectral shape only . (b) Spectral shape and time variation.

11.3 Oscillation constraint from SK

The combined χ^2 to be minimized is following:

$$\begin{aligned}\chi^2_{specSK} &= Min(\chi^2_{\alpha,SK1}(\beta,\eta,\delta_B,\delta_{S1},\delta_{R1}) \\ &+\chi^2_{\alpha,SK2}(\beta,\eta,\delta_B,\delta_{S2},\delta_{R2}) \\ &+\chi^2_{\alpha,SK3}(\beta,\eta,\delta_B,\delta_{S3},\delta_{R3}) \\ &+\delta^2_B+\delta^2_{S1}+\delta^2_{R1}+\delta^2_{S2}+\delta^2_{R2}+\delta^2_{S3}+\delta^2_{R3}) \end{aligned} \quad (11.20)$$

where the energy threshold is 5.0MeV (i=2 to 22) for SK-I and 7.0MeV (i=6 to 22)for SK-II [46]. In Equation 11.20, seven parameters are fitted. The full SK χ^2 is obtained by adding the time variation terms in each phase.

$$\chi^2_{SKfull} = \chi^2_{specSK} + \Delta\chi^2_{t.v.SK1} + \Delta\chi^2_{t.v.SK2} + \Delta\chi^2_{t.v.SK3} \quad (11.21)$$

Figure 11.3 show the exclusion region obtained from the spectral fit (a), and the spectral fit plus the time variation (b).

Chapter 12

Discussion

12.1 Global oscillation analysis

The combined analysis of other solar neutrino experiments and KamLAND experiment is discussed in this section. The numbers which are used in this global analysis are based on the results summarized in Section **??**.

12.1.1 SNO

The results of the CC total flux measured by D_2 O phase(CC) and salt phase(CC) are included in this thesis. For the NC flux, the latest low-energy threshold analysis (LETA) [47] is also included. The latest value of NC flux is

$$\Phi_{NC} = 5.14^{+0.160}_{-0.158}(\text{stat.})^{+0.132}_{-0.117}(\text{sys.}) \times 10^6 \text{cm}^{-2}\text{s}^{-1} \tag{12.1}$$

This represents 3.1% statistical uncertainty and 2.4% systematic uncertainty.

The definition of χ^2 is following:

$$\begin{aligned}\chi^2_{SNO} = &\frac{(D_{CC}^{SNO1} - (\beta B_{CC}^{SNO1} + \eta H_{CC}^{SNO1}))^2}{(\sigma_{CC}^{SNO1})^2} + \frac{(D_{CC}^{SNO2} - (\beta B_{CC}^{SNO2} + \eta H_{CC}^{SNO2}))^2}{(\sigma_{CC}^{SNO2})^2} \\ &+ \frac{(D_{NC} - (\beta B_{SSM} + \eta H_{SSM}))^2}{(\sigma_{NC})^2} + \frac{(ADN_{CC} - ADN_{pred}(\beta,\eta))^2}{(\sigma_{ADN_{CC}})^2}\end{aligned} \tag{12.2}$$

where $ADN_{pred}(\beta,\eta)$ is the predicted day-night asymmetry parameter of pure D_2O phase:

$$ADN_{pred}(\beta,\eta) = 2 \times \frac{(\beta B_{CC}^{SNO1,day} + \eta H_{CC}^{SNO1,day}) - (\beta B_{CC}^{SNO1,night} + \eta H_{CC}^{SNO1,night})}{(\beta B_{CC}^{SNO1,day} + \eta H_{CC}^{SNO1,day}) + (\beta B_{CC}^{SNO1,night} + \eta H_{CC}^{SNO1,night})} \tag{12.3}$$

The combined χ^2 to be minimized is then given:

$$\chi^2_{SK+SNO}(\beta,\eta) = \chi^2_{specSK}(\beta,\eta) + \chi^2_{SNO}(\beta,\eta) \tag{12.4}$$

The common flux scale factors are used in this calculation. So, the number of fitted parameters are 7, same as in Equation 11.20.

12.1.2 Radiochemical and Borexino

The Homestake, GALLEX/GNO, SAGE and Borexino (only ^{7}Be neutrino flux [48] is used in this thesis) rates are added to the χ^2. The calculation of the χ^2 from these experiments are based on [49].

$$\chi^2_{GaClBore} = \sum_{n,m=1}^{N(=3)} (R_n^{expt} - R_n^{theor})[\sigma^2_{nm}]^{-1}(R_m^{expt} - R_m^{theor}) \tag{12.5}$$

where GALLEX/GNO, and SAGE are merged into one Ga experiment and N is the number of experiments. According to [25], the merged result from Ga experiment is

$$66.1 \pm 3.1 \qquad \text{SNU (All Ga experiment)} \tag{12.6}$$

The σ^2_{nm} is a matrix of squared uncertainty [50] which are the sum of the correlated uncertainty (such as uncertainties of SSM) and uncorrelated uncertainty among these experiments, , R_n^{expt} is the observed solar neutrino rate for the n-th experiment, and R_n^{theor} is the predicted solar neutrino rate by the SSM. In this thesis, correlation of β, η among Radiochemical experiments are omitted because the dependence could be negligible in Large Mixing Angle (LMA) solution area.

12.1.3 KamLAND

KamLAND experiment (2002$\sim$)is a liquid scintillator experiment in Japan. measuring the inverse beta decay reaction:

$$\bar{\nu_e} + p \longrightarrow e^+ + n \tag{12.7}$$

KamLAND detects antineutrinos from surrounding nuclear reactors. According to the latest result from 2002 to 2007, the total exposure is 2.44×10^{32} proton-yr(2881 ton-yr). The best fit parameters are obtained as $\Delta m^2_{12} = 7.58^{+0.14}_{-0.13}(stat)^{+0.15}_{-0.15}(sys) \times 10^{-5} eV$ and $\tan^2\theta_{12} = 0.56^{+0.10}_{-0.06}(stat)^{+0.10}_{-0.06}(sys)$ [51].

Adding the χ^2 which is given in [51], the combined result is shown in the filled contour in Figure 12.2.

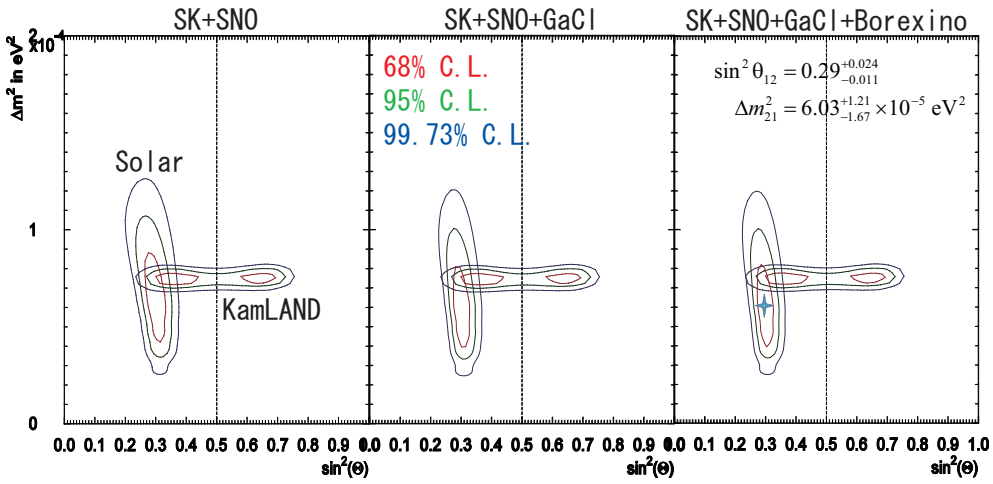

Figure 12.1: Allowed region of LMA (inside area of the line is allowed)

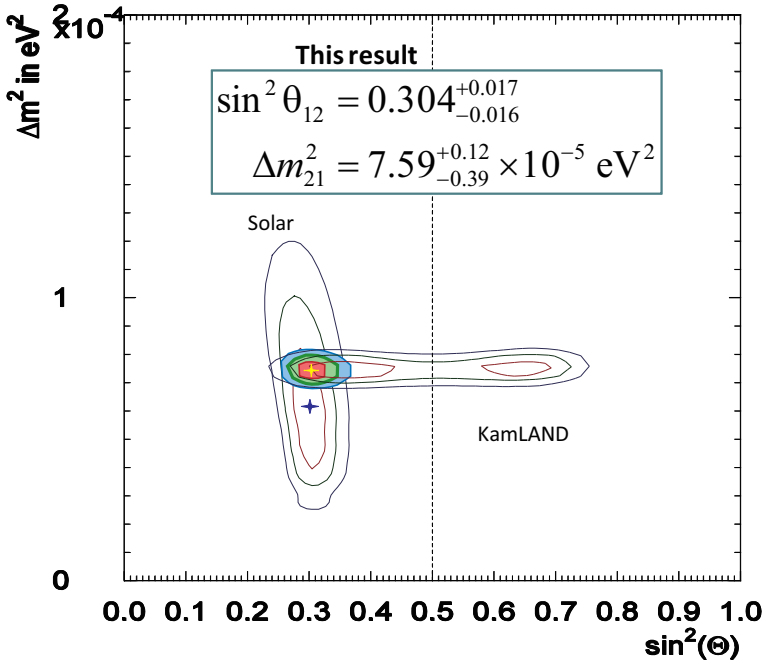

Figure 12.2: Allowed region of LMA, Solar + KamLAND (inside area of the line is allowed)

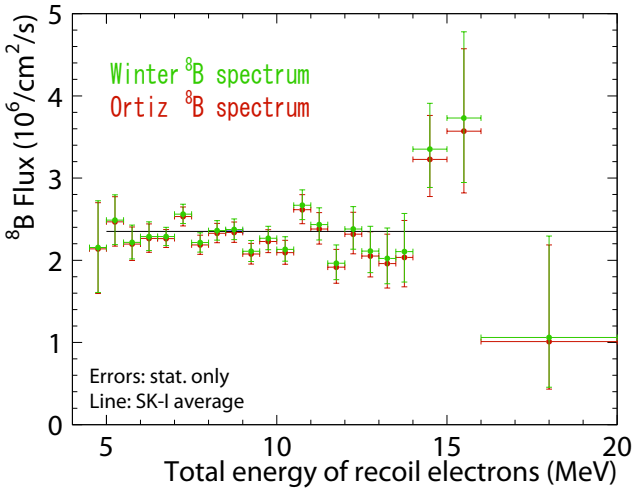

Figure 12.3: SK-III data /SSM (BP2004) with Winter and Ortiz ^{8}B spectrum. Green shows SSM with Winter ^{8}B spectrum, and red shows SSM with Ortiz ^{8}B spectrum.

12.2 Comparison of Winter and Ortiz ^{8}B spectrum

In this section, the effect of the difference between Winter ^{8}B spectrum and Ortiz ^{8}B spectrum to the oscillation contour is discussed.

Figure 12.3 shows the SK-III energy spectra divided by SSM with Winter ^{8}B spectrum and Ortiz ^{8}B spectrum. Since the Ortiz spectrum has more tail in the higher energy region compared to the Winter spectrum (see Figure 2.8), the energy spectrum over the SSM prediction becomes larger in high energy region if the Winter spectrum is used for the SSM prediction. Therefore, if the Wineter spectrum is used, this makes the χ^2 value of the spectrum fitting worse in the LMA solution area because the LMA predicts upturn of the energy spectrum in the lower energy region, and thus, the LMA area is excluded slightly lager. In Figure 12.4, we can see this effect. For the spectrum fitting, I use different energy correlated systematic uncertainties for Winter and Ortiz spectrum which are shown in Figure 9.5.

12.3 Comparison with other results

Figure 12.5 shows the comparison of the results on the mixing angle measurements. The reason why only the mixing angle results are compared is that the uncertainty of Δm^2 is mainly controlled by KamLAND, and thus, for the solar neutrino experiments, the contribution to the Δm^2 measurement is smaller than the contribution to the mixing angle measurement. As shown in Figure 12.5, even though only the CC and NC rate information from SNO are used in this thesis, the size of uncertainty is about the same. This indicates that if more information of the SNO results, for example CC spectral shape, is added to the SK result, the global analysis results will be improved.

Using these oscillation parameters obtained from the solar and reactor experiments, the flux value of ^{8}B neutrino can be extracted. As in Equation 11.20, the β is a free parameter to minimize the χ^2_{SK+SNO} and there is no constraint from the SSM prediction in the χ^2_{SK+SNO}.

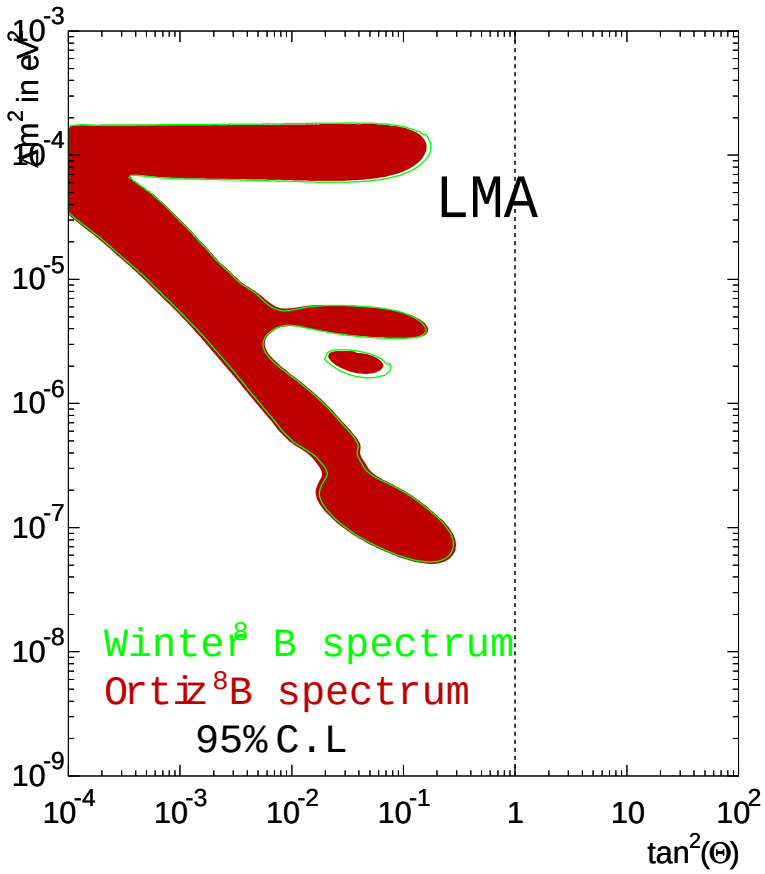

Figure 12.4: Excluded region by SK-III data /SSM (BP2004) with Winter and Ortiz ^{8}B spectrum shapes. Green shows SSM with Winter ^{8}B spectrum, and red shows SSM with Ortiz ^{8}B spectrum.

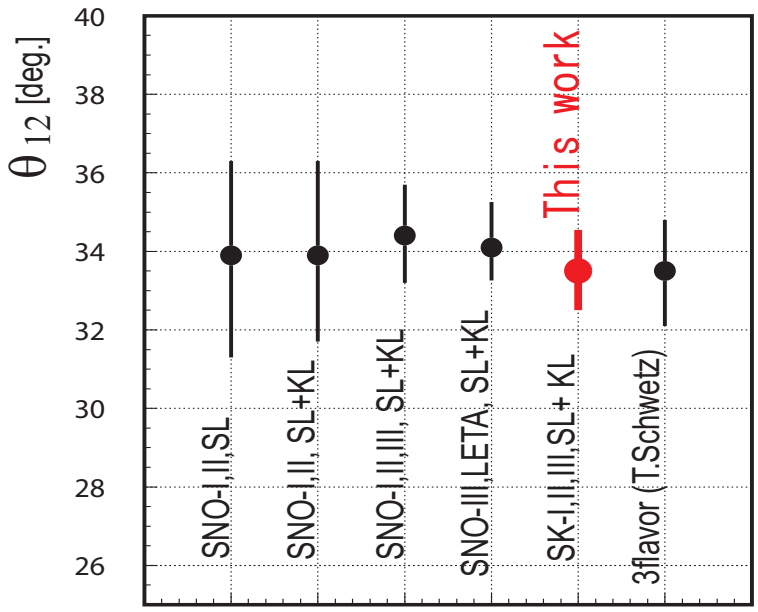

Figure 12.5: Comparison of the mixing angle measurement between SNO results and the results obtained by this thesis. the error size corresponds to 1 σ uncertainty of (stat.+sys.). SNO-I,II,SL use SNO phase I and II and other solar neutrino data (SL) [29] and SNO-I,II,SL+KL added KamLAND(2004) [29]. SNO-I,II,III,SL+KL add the phase III [30] and updated KamLAND(2008) [51]. SNO-III,LETA+KL is latest SNO result [47]. Result of this work is shown as SK-I,II,III SL+KL. The 3 flavor analysis is from the analysis of latest solar + reactor+ atmospheric results [52]

Thus, the flux value scaled by the β_m does not depend on the SSM so much. Figure 12.6 shows the scaled ^{8}B flux values by using the β_m at the best fit point obtained by the global solar analysis and the global solar + KamLAND analysis and they are compared with the ^{8}B flux obtained by SNO NC rate. The size of error corresponds to the maximum and minimum flux values among the 1σ oscillation parameter region. The obtained ^{8}B flux values are;

$$\text{Global solar analysis:} \qquad 5.27^{+0.16}_{-0.13} \times 10^6 cm^{-2} s^{-1}$$
$$\text{Global solar+KamLAND analysis:} \qquad 5.08^{+0.10}_{-0.07} \times 10^6 cm^{-2} s^{-1}$$

As shown in Figure 12.6, the flux obtained by the solar neutrino experiments agree with the all the SSM predictions (BP04, BS05(OP) and BS05(AGS,OP)), and the seismic model prediction [7] within their uncertainties. However, the size of the experimental uncertainty ($\sim 2\%$)is much smaller than that of SSMs. Thus, our results of ^{8}B flux measurement can be a strong tool to test the future improvement of SSM.

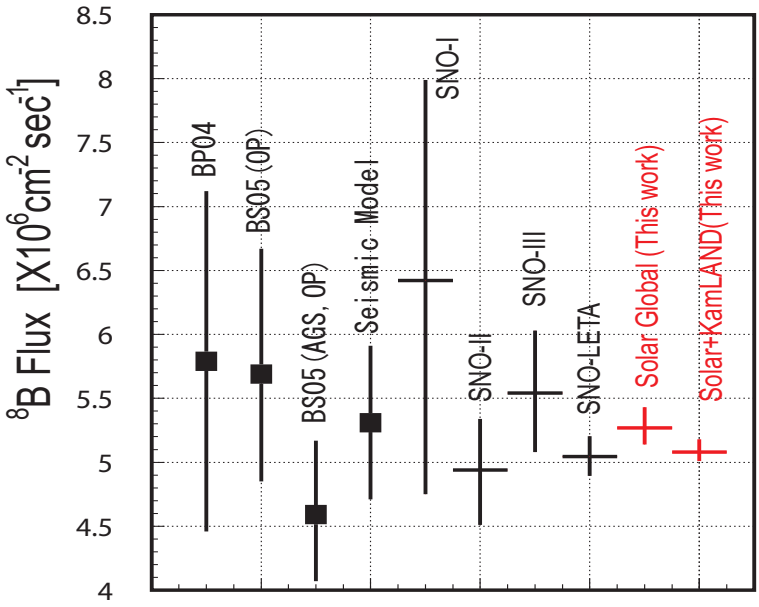

Figure 12.6: Comparison of the ^{8}B flux between SNO results and the results obtained by this thesis. the error size corresponds to 1 σ uncertainty of (stat.+sys.). Square mark shows theoretical predictions and cross marks shows experimental results.

12.4 Treat reduction uncertainties as energy correlated uncertainties

In Chapter 9, the uncertainties of ambient cuts (ovaQ cut and hit pattern cut) are treated as energy uncorrelated uncertainty. However, if MC simulation gives systematically better goodness than the real data, for example, the uncertainties for each energy bins move to the same direction. That is, the uncertainties of ambient cuts have some energy correlation. To estimate how this energy correlation affects the fitting of the spectrum, those uncertainties (ovaQ cut and hit pattern cut) are treated as energy correlated uncertainties here.

Figure 12.7 shows the uncertainties of ovaQ cut and hit pattern cut which are obtained from the comparisons between LINAC data and MC simulation (see Figure 9.1 and 9.2 of Section 9.6). These uncertainties are assigned as $\pm 1\sigma$ uncertainties of the ambient cut efficiency (see the purple histogram of Figure 7.21), and treated as $\epsilon_x^{\pm}$ of Equation 11.11. Hence, the definition in $\chi^2_{specSK3}$ of Equation 11.16 becomes

$$\chi^2_{specSK3}(\beta,\eta) = \mathrm{Min}(\chi^2_{\alpha,SK3}(\beta,\eta,\delta_B,\delta_S,\delta_R,\delta_{ovaQ},\delta_{HitPat}) + \delta_B^2 + \delta_S^2 + \delta_R^2 + \delta_{ovaQ}^2 + \delta_{HitPat}^2) \tag{12.8}$$

where the free parameters to be fitted are $\beta, \eta, \delta_B, \delta_S, \delta_R, \delta_{ovaQ}, \delta_{HitPat}$. To avoid double counting of uncertainties, the energy uncorrelated systematic uncertainties are modified as in Table 12.1.

By taking them as energy correlated uncertainties, all data points shift to the same direction when they are fitted. This treatment gives a slightly tighter allowed region than when the data points are uncorrelated (see Figure 12.8). The best-fit point is unchanged after this modification.

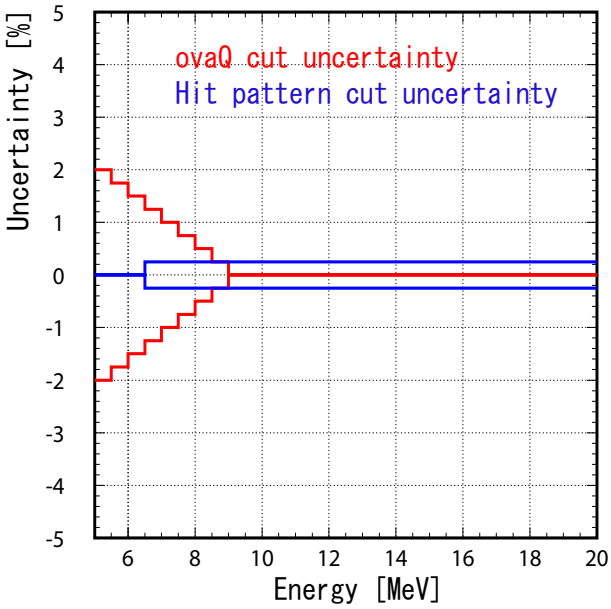

Figure 12.7: Energy correlated systematic uncertainties of ovaQ and hit pattern cut.

Energy(MeV)	5-5.5	5.5-6	6-6.5	6.5-7	7-7.5	7.5-20
Total	±3.8%	±2.4%	±2.1%	±0.8%	±0.8%	±0.8%

Table 12.1: Energy uncorrelated systematic uncertainty on the spectrum shape. The contributions from ovaQ and Hit pattern cut are removed from Table 9.3

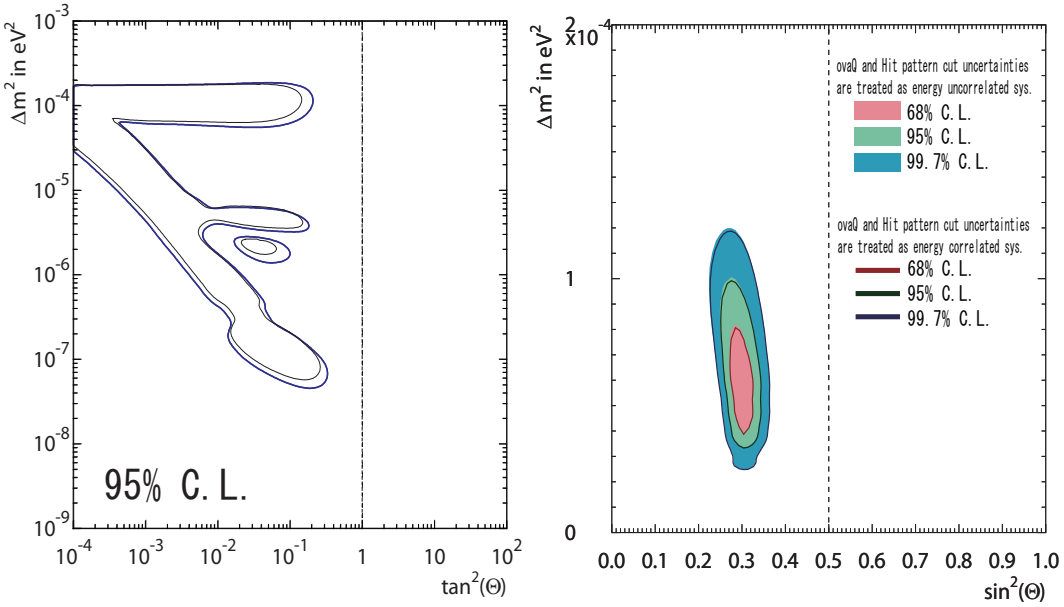

Figure 12.8: Excluded region (inside area of blue line) from SK-III spectrum fit (left) and allowed region from all solar neutrino experiments (right). The systematic uncertainties of ambient cut are treated as energy correlated uncertainties. Black line in left plot shows the result in which the uncertainties have no correlation. The best fit point of global analysis is not changed whether the uncertainties are energy correlated or not.

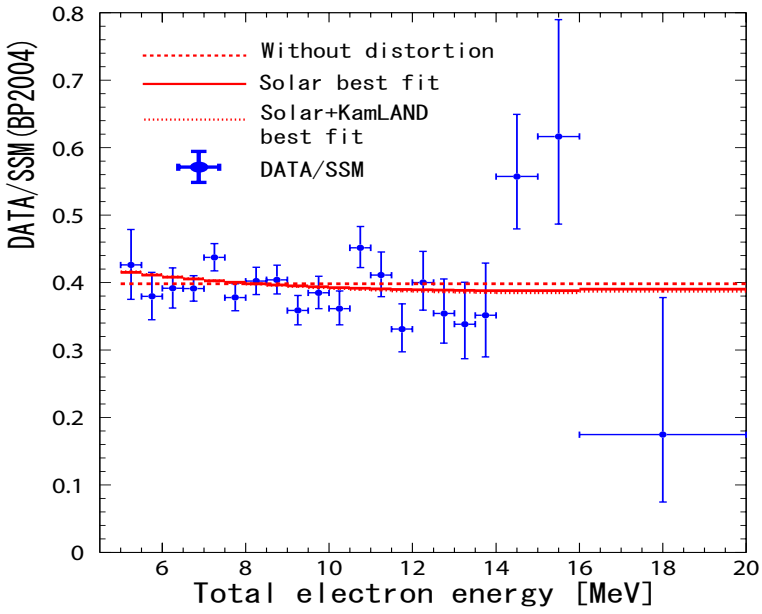

Figure 12.9: SK-III spectrum with expected distorted shapes and flat shape. The error shows only statistical uncertainty.

Even if this treatment gives better results, it is not clear how much the uncertainty band shown in Figure 12.7 is energy correlated. Thus, in the final results on parameter region of solar neutrino oscillation, the uncertainties of the ambient cuts are treated as energy uncorrelated conservatively.

12.5 Sensitivity to upturn

Figure 12.9 shows SK-III energy spectrum with solar best fit, solar plus KamLAND best fit, and flat expectations. The χ^2 value with each case is following: 26.8/20d.o.f. (solar best fit: $\Delta m^2 = 6.03 \times 10^{-5} eV^2$, $\sin^2\theta = 0.29$), 26.7/20d.o.f. (solar plus KamLAND best fit: $\Delta m^2 = 7.59 \times 10^{-5} eV^2$, $\sin^2\theta = 0.34$), and 27.7/20d.o.f. (flat shape). When the ambient cut uncertainties are treated as energy correlated systematic uncertainty, the χ^2 value with each case is following: 26.9/20d.o.f. (solar best fit), 27.0/20d.o.f. (solar plus KamLAND best fit), and 27.5/20d.o.f. (flat shape).

Figure 12.10 shows spectral shape of each phase with solar best fit expectation. Although it is not statistically significant, the spectral shape of SK-III might show a little hint of the upturn.

Finally, a sensitivity of the observation of upturn is estimated. Followings are assumed for this estimation;

1. Background level is same as SK-III.
2. Energy correlated systematic uncertainty is half of SK-I
3. 4 MeV threshold is accomplished.

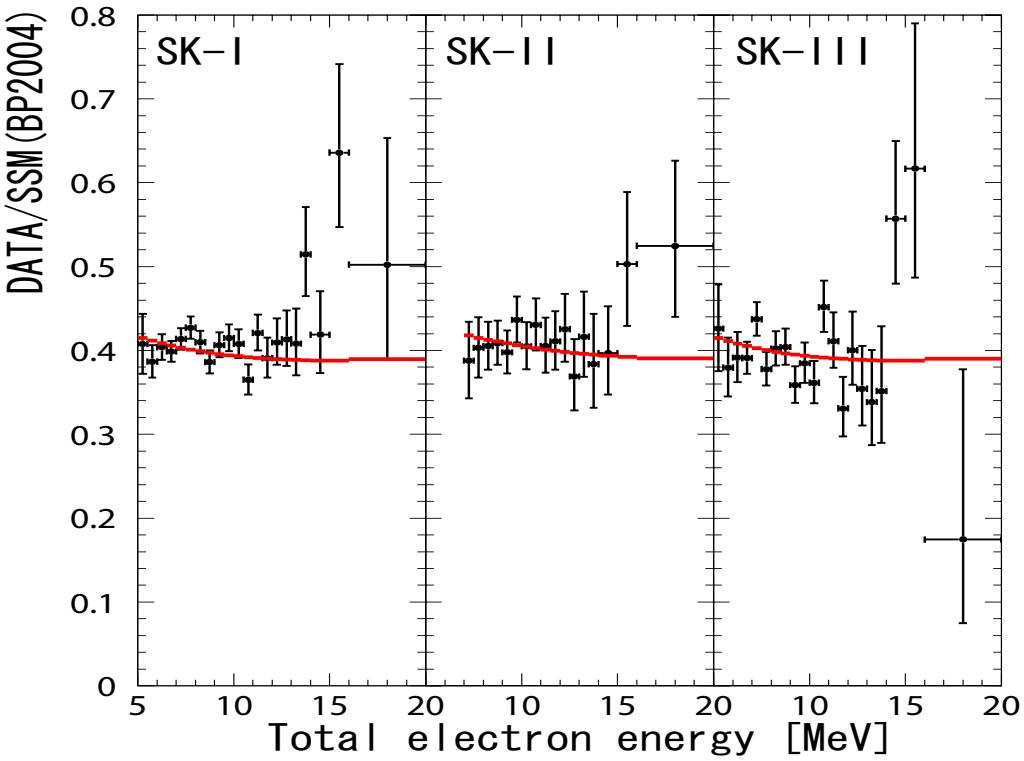

Figure 12.10: SK-I,II, and III spectrum with expected distorted shapes and flat shape. The error shows only statistical uncertainty.

If we use Winter06 ^{8}B spectrum, energy correlated uncertainty of SK-III already achieves 30% improvement since SK-I. Further 20% improvement would be possible if the position and direction dependence of energy scale becomes half of current dependence. This is done by more precise calibrations and a better modeling of water condition. Item 3 would be possible because the new electronics and DAQ system, which are already installed in 2008, can store all hit information without hardware trigger. Under this assumption, about 2σ level observation within 3 years, and about 3σ level within 10 years could be expected. In addition to new data, re-analysis of SK-I data is desirable because the calibration method and analysis tools which are developed in this thesis can be applied to SK-I data and expected to reduce uncertainties. Since we already have 6 years of total livetime during SK-I and III, A 3σ level discovery of the upturn might be possible within few years if the SK-I data are re-analyzed.

Chapter 13

Conclusion

In conclusion, the measurement of solar neutrino with SK-III was carried out aimed at the observation of the spectrum distortion due to MSW effect. The strategies of this thesis to achieve this goal are to reduce the background level by 70% from SK-I in the lower-energy region, and to reduce the energy correlated systematic uncertainty by 50% compared to SK-I.

With improved detector calibrations, a full detector simulation, and analysis methods, the number of background events is reduced by about 50% from SK-I. Meanwhile, the energy correlated systematic uncertainties are reduced by 30%, and the energy uncorrelated systematic uncertainties are reduced by 60% from SK-I. Thus, the goal is almost achieved and acceptable for the future observation of the spectrum distortion.

The systematic uncertainty of the total flux is estimated as $\pm 2.3\%$, and is about two third of SK-I. The ^{8}B flux in SK-III is

$$2.28 \pm 0.04(stat.) \pm 0.05(sys.) \ \times 10^6 \mathrm{cm}^{-2}\mathrm{sec}^{-1}$$

which is the most precise result of previous results from SK-I and II. A day-night asymmetry is obtained to be

$$A_{DN} = -0.057 \pm 0.031(stat.) \pm 0.013(sys.)$$

After combining the previous phase of SK and other solar neutrino experiments, the best-fit parameters of the solar neutrino oscillation are determined with the world's best accuracy;

$$\begin{aligned} \sin^2\theta_{12} &= 0.29^{+0.024}_{-0.011} \\ \Delta m^2_{12} &= 6.03^{+1.21}_{-1.67} \times 10^{-5} eV^2 \end{aligned}$$

By adding the result from KamLAND, the obtained best-fit parameters are

$$\begin{aligned} \sin^2\theta_{12} &= 0.304^{+0.017}_{-0.016} \\ (\theta_{12} &= 33.46^{+1.05}_{-1.00}) \\ \Delta m^2_{21} &= 7.59^{+0.12}_{-0.39} \times 10^{-5} eV^2 \end{aligned}$$

which are consistent with the latest analysis by SNO group.

The χ^2 value of spectrum fit with the solar plus KamLAND best-fit prediction is 26.7/20d.o.f. which is slightly better than 27.7/20d.o.f. with a flat shape. Although, this result is not statistically significant, it is estimated that the improved calibration and analysis methods will give a sensitivity of 3σ level discovery of the spectrum distortion within a few years, together with re-analysis of the SK-I data.

Appendix A

Glossary

ADC Analog to Digital Converter

ATM Analog Timing Module; front end electronics based on TKO standard.

BP04 One of the SSM series published in 2004, which is used in this thesis.

BONSAI Branch Optimization Navigating Succesive Annealing Iterations, the standard vertex fitter for this analysis.

BS05(AGS,OP) One of SSM series published in 2005, which uses the latest physics information, called the "low Z" model including updated opacity calculation by Opacity Project.

BS05(OP) One of SSM series published in 2005, which used the previous heavy metal abundance, called the "high Z" model. Other updates including the opacity calculation by OP are implemented.

COREPMT Average Q.E. determined by LINAC 8.8MeV. This in one of input parameters for MC

DT Duteron Tritium generator (neutron source)

HE High Energy Trigger (-320mV)

HITSUM summation of hit square pulses

ID Inner Detector

LMA Large Mixing Angle solution of solar neutrino oscillation

LE trigger Low Energy trigger (-302mV)

LINAC LINear ACcelerator

LMA Large Mixing Angle solution of the solar neutrino oscillation. $10^{-5} < \Delta m^2 < 10^{-4}\mathrm{eV}^2$ and $\theta_{12} \sim 30 - 40^{\circ}$

N_{eff} Effective number of hits in a event.

N_{hit} The number of hits in one event.

Ni calibration Calibration using Cf-Ni gamma-ray source

N_x The number of hits within x nsec time window. The number is found after applying the sliding x nsec time-window search to the $t - tof - t_0$ distribution.

OD Outer Detector

ovaQ One dimensional variable for Vertex and Angular Quality: $G_V^2 - G_A^2$

PMT Photo Multiplier Tube

QAC Charge to Analog Converter

Q.E. Quantum efficiency of PMT

Seismic model One of solar models. This model is based on a standard stellar evolution and the input information is adjusted for the Sun by the seismic measurements.

S-factor Cross section factor of nuclear fusion reactions in the Sun.

SLE1 trigger Super Low Energy trigger period 1(-212mV)

SLE2 trigger Super Low Energy trigger period 2(-186mV)

SMP Super Meory Partner; VME memory modules after ATM

Spallation cut Cut to reject sapallation products

SSM the Standard Solar Model. A series of solar model first developed by J.N.Bahcall.

TAC Timing to Analog Converter

TBA Top Bottom Asymmetry of the detector

Tisk hit timing of each PMT (without subtruction of TOF)

TKO Tristan KEK Online standard

TOF Time of flight

TQmap Hit timing correction function as a fuction of charge

TRG TRiGger module which distribute the global trigger and the event number

Bibliography

[1] Z. Maki et al. Phys.Lett. **28B** 498 (1969)

[2] L. Wolfenstein Phys.Rev.D **17** 2369 (1978)

[3] S. P. Mikheyev and A. Yu. Smilnov Nuovo Cim. **9C** 17 (1986)

[4] J. N. Bahcall *Neutrino Astrophysics* Cambridge University Press (1989)

[5] J. N. Bahcall et al. Phys.Lett,B **374** 1 (1996)

[6] H. Bethe Phys.Rev., **55** 434 (1939)

[7] Turck-Chieze et al. Phys.Rev.Lett. **93** 211102 (2004)

[8] J. N. Bahcall et al. Phys.Rev.Lett., **92** 121301 (2004)

[9] J. N. Bahcall et al. Astrophys.J, **621** 83 (2005)

[10] A. M. Serenelli Nucl.Phys.B (Proc.Suppl.), **168** 115 (2005)

[11] M. Asplund et al. Nucl.Phys.A **777** 1 (2005)

[12] N. Grevesse et al. Space.Sci.Rev., **85** 161 (1998)

[13] N. R. Badnell et al. MNRAS, **360** 458 (2005)

[14] C. A. Iglesias Astrophys.J., **464** 943 (1996)

[15] A. M. Serenelli Astrophys.J., **705** 123 (2009)

[16] D. L. Anderson, *Theory of the Earth* Blackwell scientific publication (1989)

[17] C. E. Ortiz et al. Phys.Rev.Lett., **85** 2909 (2000)

[18] J. N. Bahcall et al. Phys.Rev.C **54** 411 (1996)

[19] W. T. Winter et al. Phys.Rev.C, **73** 025503 (2006)

[20] J. Hosaka et al. (Super-Kamiokande Collaboration) Phys.Rev.D, **73** 112001 (2006)

[21] Phys.Rev.Lett D **62** 113004 (2000)

[22] B. T. Cleveland et al. Astrophys.J., **496** 505 (1998)

[23] W. Hampel et al. Phys.Lett.B **447** 127 (1999)

[24] M. Altmann et al. Phys.Lett.B **616** 174 (2005)

[25] T. J. Bowles arXiv:0901.2200v1

[26] Y. Fukuda et al, Phys.Rev.Lett **77** 420 (1998)

[27] C. Arpesella et al. Phys.Lett. **B658** 101 (2008)

[28] Q. R. Ahmad et al. Phys.Rev.Lett. **89** 011301 (2002)

[29] B. Aharmim et al. Phys.Rev. **C72** 055502 (2005).

[30] B Ahrmim et al. Phys.Rev.Lett **101** 111301 (2008)

[31] S. Fukuda et al. Nucl.Instr.and Meth. A **51** (2003) 418

[32] http://sales.hamamatsu.com/assets/pdf/parts_R/R3600-06.pdf

[33] H. Ikeda et al. Nucl.Inst.and Meth. A **320** 310 (1992)

[34] T. Tanimori et al. IEEE Trans.Nucl.Sci **NS-36** 497 (1989)

[35] T. K. Ohsuka et al. *KEK Report* 85-10 (1985)

[36] M. Smy Proc. of the 30th ICRC, **5** 1279 (2007)

[37] "GEANT - Detector Description and Simulation Tool", CERN Program Library (1993)

[38] Y. Koshio Ph.D thesis, University of Tokyo, ICRR-Report-426-98-22 (1998)

[39] R. M. Pops et al. Applied Optics **35** 33 (1997)

[40] E. Blaufuss et al. Nucl.Instr.and Meth. A **458** 636 (2001)

[41] W. Y. Chang et al. Nature **139** 962 (1937)

[42] M. Nakahata et al. Nucl.Instr.and Meth. A **421** 113 (1999)

[43] L. Lyons, *Statistics for nuclear and particle physicists* Cambridge University Press, Cambridge

[44] E. Commins and P. H. Bucksbaum *Weak interactions of leptons and quarks* Cambridge University Press, Cambridge

[45] J. N. Bahcall et al. Phys.Rev.D **51** 6416 (1995)

[46] J. P. Cravens Phys.Rev.D **78** 032002 (2008)

[47] B. Aharmim et al. arXiv:0910.2984v1 (2009)

[48] E. A. Litvinovich Phys.Atom.Nucl. **72** 522 (2009)

[49] G. L. Fogli et al. Phys.Rev.D **66** 05310, arXiv:hep-ph/0206162v1 (2002)

[50] G. L. Fogli et al. PHys.Rev.D **62** 013002

[51] S. Abe et al. Phys.Rev.Lett. **100** 221803 (2008)

[52] T. Schwetz et al. New Journal of Physics **10** 113011 (2008)